PREDICTION OF THE CRYSTALLIZATION ONSET TEMPERATURES OF MOLECULAR LIQUIDS

by

Omar Al-Qatami

Submitted in partial fulfilment of the requirements

for the degree of Doctor of Philosophy

at

Dalhousie University

Halifax, Nova Scotia

June 2023

Dalhousie University is located in Mi'kma'ki,

the ancestral and unceded territory of the Mi'kmaq.

We are all Treaty people.

TABLE OF CONTENTS

LIST OF TABLES

LIST OF FIGURES

ABSTRACT

The processes of nucleation and crystallization while cooling are crucial to industry and require specialized models for characterization for process optimization, predictive capabilities and final products quality. Triacylglycerols (TAG) are essential in biology and nutrition, as well as in pharmaceutical and cosmetic industries. Liquid TAG molecules require deep undercooling to crystallize, and it is very difficult for them to form glasses. Their kinetics of crystallization are slow enough to be studied in reasonable timeframes, i.e. seconds to minutes. Upon crystallization TAG molecules self-arrange in lamellar-shaped nanocrystals, which can exist in several polymorphic forms, classified by their unit cells. These polymorphs are monotropic with a distinct thermodynamic stability hierarchy. However, predicting the type of polymorph and the temperature at which it will be formed is a know-how that is still missing from the current state of the art. A very fundamental tool to describe the process that happens before nuclei are observed (pre-nucleation) is the Fisher-Turnbull equation, which is based on the theory of homogeneous nucleation. It links the rate of forming embryos of growing sizes, up to the critical size (made up of a certain number of molecules) with the free energy needed to make a stable nucleus and the temperature at which crystallization begins (crystallization onset). In this study, to allow for time-temperature profiles, we used the differential version of the Fisher and Turnbull model to calculate the nucleation rates of the TAG tridodecanoyl-glycerol (LLL), when it is cooled at different rates. The parabolic partial differential equation was solved algebraically and programmed to be solved numerically with MATLAB, making this model accessible to many researchers. The crystallization temperatures were calculated as the point where temperatures deviated from the heat flow baseline obtained from differential scanning calorimetry (DSC) thermograms. The detection of these onset temperatures was carried out using a custom MATLAB code. The polymorphic forms were identified using time-resolved small and wide-angle X-ray diffraction (SAXD and WAXD) data obtained from experiments at a synchrotron. This is necessary to link thermal properties, such as undercooling (T_m-T_{onset}), enthalpy, entropy, and Gibbs free energy of crystallization to the identified polymorphs. For our model, we introduced three critical factors: a nanoplatelet embryo geometry, an interfacial energy dependent on temperature, and an activation energy barrier which varies based on temperature and the number of embryo molecules. Additionally, we expanded this model to describe the secondary heterogeneous nucleation of the α polymorph on the surface of the β'. Based on the model, it was found that critical embryo size of the β' polymorph was $i^* = 44$ molecules when cooled at 15.0 K/min, and the minimum interfacial energy, δ, is 11 to 14 $\times 10^{-24}$ kJ/nm^2 for $\Delta T = 13$ to 20 K. With this information, we can accurately predict the types of polymorphs that will form and at what specific temperature they crystallize.

LIST OF ABBREVIATIONS AND SYMBOLS USED

C_p	Specific heat capacity (J/g.◦C)
DSC	Differential scanning calorimeter
FEM	Finite element method
MMM	1,2,3-Tritetradecanoyl-glycerol, trimyristin
EEE	1,2,3-Tri(trans-9-octadecenoyl)-glycerol, trielaidin
LLL	1,2,3-Tridodecanoylglycerol, trilaurin
PPP	1,2,3-Trihexadecanoyl-glycerol, tripalmitin
SSS	1,2,3-Tristearoyl-glycerol, tristearin
CrCrCr	1,2,3-Tridecanoylglycerol, tricaprin
ClClCl	1,2,3-Trioctanoylglycerol, tricaprylin
CoCoCo	1,2,3-Tricaproylglycerol, tricaproin
TAG	Triacylglycerol
RCS	Refrigerated cooling system
MDSC	Modulated differential scanning calorimetry
GC	Gas chromatography
GUM	Expression of uncertainty in measurements
PDE	Partial differential equation
SAXD	Small angle X-ray diffraction
WAXD	Wide angle X-ray diffraction
T&F	Turnbull and fisher
$\Delta\mu$	Chemical potential
ΔS_m	Melting entropy (J/mol. K)
ΔH_m	Melting enthalpy (J/mol)
T_m	Melting temperature (˚C)
T_o	Onset temperature
ΔG_v	Volume formation free energy change

ΔG_s	Surface formation free energy change
ΔG_{hom}	The Gibbs free energy of homogeneous nucleation
δ	Interfacial tension (interfacial energy)
r_c	Critical nucleus size
k_b	Boltzmann constant (=1.38*10^{-23}J/K)
N_A	Avogadro constant (= 6.022*10^{23}/mol)
q	Heat flow (W/g)
d	Spacing between crystal lattice planes
α	Thermal diffusivity (mm^2/s)
κ	Thermal conductivity W/(mm·°C)
n_i	Number of embryos with given number of '*i*' molecules
i	Number of molecules in the growing surface
i^*	Critical size for nucleus
ξ	Nanoplate geometrical dimension
v_s	Molar volume
m	Number of molecules per a dimension (molecule/nm)
θ(t)	Relative crystallinity at a time *t*

ACKNOWLEDGEMENTS

Throughout the process of earning my PhD, I have been provided with a great deal of assistance and direction, for which I am extremely grateful. I would like to begin by extending my gratitude to my supervisor, Dr. Gianfranco Mazzanti, for his unflinching support, patience, and invaluable feedback throughout the entirety of my research. His direction and expertise have had a significant impact on all of my research questions, methodologies, and conclusions. I count myself extremely fortunate to have had the chance to work with such a wonderful mentor, and I am indebted to him for the support he has provided me with.

I would also like to take this opportunity to thank the members of my committee, Dr. Amyl Ghanem and Dr. Kevin Plucknett, whose input, suggestions for improvement, and direction have been extremely helpful. Their expertise and insights have been invaluable in assisting me to develop a more in-depth understanding of the topic of my research, and the suggestions they have provided have enhanced the quality of my investigation. I count it a privilege to have had the opportunity to collaborate with such a distinguished collection of academics, and I am appreciative of their contributions to the work that I have done.

I would also like to express my appreciation to my family, friends, and colleagues who have been there for me as I pursued my PhD. It would not have been possible for me to make it through the ups and downs of graduate school without their support, guidance, and friendship. I count myself extremely fortunate to have such a wonderful support system, and I am thankful for the unwavering support they have provided me with.

I would like to make mention of the difficulties I had to overcome regarding my health

while I was working on my PhD. Despite the difficulties they presented, I was able to gain valuable insights about tenacity, resiliency, and the significance of prioritizing self-care. I would like to express my sincere gratitude to my supervisor, my committee, and the graduate coordinator, Dr. Sue Budge, who assisted me during these difficult times, as well as to my parents, family and friends, who were there for me when I needed encouragement and provided me with emotional support.

I would like to express my appreciation to everyone who has helped me along the way to obtaining my PhD, and I am awed by the wealth of information, experiences, and friendships I have acquired along the way. I am thankful to each and every one of these individuals for their support and encouragement, without which obtaining this degree would not have been possible.

CHAPTER 1 INTRODUCTION

1.1 MOTIVATION OF THE CURRENT WORK

The field of crystallization studies, much like other scientific disciplines, is deeply influenced by the technology and methodologies available at the time. The current understanding of crystallization from a homogeneous liquid, for example, is largely shaped by the technological tools we have been able to apply to this complex process. These tools have allowed us to probe and analyze the intricacies of crystallization, giving us a relatively detailed, albeit potentially incomplete, picture of this phenomenon. Limitations in technology can sometimes impede our ability to thoroughly investigate and validate theoretical concepts related to crystallization. For example, the accurate observation of the formation of the initial solid phase, known as nucleation, has always been challenging due to its microscopic and transient nature. Traditional methods may not provide the resolution or speed necessary to capture these short-lived, critical events. As technology continues to evolve, however, so too does our capacity to examine and refine established theories. With these technological advancements, it becomes necessary and indeed vital to revisit and potentially revise our understanding of crystallization from a homogeneous liquid. Advanced technologies such as time-resolved synchrotron X-ray diffraction and sensitive calorimetric instrumentations have enabled the examination of crystallization structures at the atomic level (nanoscale) and determination of smallest changes in heat ($\approx 1\mu W$). In addition, new advancements in computational methods provide the computational capacity required for sophisticated data analysis and simulations. Collectively, these instruments and methods provide the capacity to assess the underlying

presumptions and processes of the concepts that establish the foundation of our present understanding of the mechanisms of nucleation and crystal growth.

The crystallization process has been utilized as a tool since our ancestors obtained salt by evaporating seawater. For tens of thousands of years, crystallization has been used for many applications in all fields. The history of crystallization and its importance has been documented beautifully by Bohm.[1] An important excerpt given below from Bohm's manuscript constitutes a major conceptual core discussed in this thesis.

"*But foremost, there is the masterly theoretical work of Gibbs (1878)* [2] *on heterogeneous equilibria, but the value of this work was generally recognized only with great delay. Gibbs determined the energy needed to generate a nucleus and derived the equilibrium form of a crystal that fulfils the condition of minimum total free surface energy. But in a footnote, he pointed out that the equilibrium form may determine the nature of small crystals only whereas the larger ones will be confined finally by such faces onto which the attachment of material proceeds most slowly."*

These concepts were developed by Gibbs, and they were used by Volmer and Weber[3], Farkas[22], Becker and Döring [4] to produce the theoretical framework that is generally recognized as the classical nucleation theory (CNT). This framework successfully describes the nucleation phenomenon in the vapor-to-liquid, vapor-to-crystal, and dilute solution-to-crystal transformations. The extension of CNT into condensed systems that was done by Turnbull and Fisher[5], and Hollomon[6], along with the Kolmogorov[7]-Johnson and Mehl[8]-Avrami [9](JMAK) model, formed the basis of our present understanding of the kinetics of phase changes in condensed systems. The compilation of these studies and their adaptations cover almost all the theoretical approaches that contribute to our present

understanding of the process by which nucleation occurs in condensed systems. Despite these advancements in our understanding of crystal nucleation, it, unfortunately, remains poorly understood.[10] A number of contributing factors lead to this, which include: 1) the microscopic and transient nature of the process, 2) the complex thermodynamics involved, 3) the inaccessibility of the pre-nucleation stage, and 4) the lack of real-time detection techniques.

under the right thermodynamic conditions (such as temperature and pressure), atoms or molecules of a substance will start to gather. They begin forming clusters, which are the early structures of a new phase (a solid state), shifting away from their original homogeneous liquid phase. A 'first-order phase transition' is a term used in thermodynamics to describe a change of state that involves latent heat. In the context of crystallization, this means the transformation from a liquid state to a solid state. During this transition, the substance absorbs or releases heat without changing its temperature. When a substance changes from one phase to another (from liquid to solid, for example), there's an 'energy cost' associated with forming the boundary between the old phase (liquid) and the new phase (solid). This boundary or interface is what separates the liquid and solid areas. The energy required to form this interface is referred to as interfacial energy. In a first-order phase transition, this energy barrier needs to be overcome for the phase change to occur. This can be thought of as the energy needed to start the transition process from liquid to solid.

This energy barrier prevents the phase transition from taking place instantaneously. As a result, the liquid transforms into a non-equilibrium (metastable) phase populated by a distribution of solid clusters of varied sizes. The size of the clusters varies because they

consist of different quantities of atoms or molecules. The rate at which clusters form is determined by the magnitude of the energy barrier and controls the transition's kinetics. This is the essence of classical nucleation theory (CNT), which has proven to be extremely effective in explaining first order phase transitions that occur in the nucleation process. Nucleation literature is largely directed toward investigating what is known as the "steady-state nucleation rate," which ignores all the time before the system reaches a point when nuclei are created at a regular rate. As a result, less effort has been devoted in studying the 'transient nucleation' regime, which includes the time before when the crystalline phase became the thermodynamically favored state (i.e., as soon as the system is lowered below its melting temperature). The crystalline phase initially occurs in this transient nucleation regime; therefore, the concern becomes not only how quickly nuclei appear, but also how nuclei appear. The significance of our research lies in its potential to serve as a valuable predictive tool for a range of industries, including pharmaceuticals, chemicals, food science and technology, energy storage, and cosmetics. It also has applications in multiple scientific fields such as materials science, environmental science, and space exploration. This tool offers the unique capability of accurately predicting both the temperature at which crystallization occurs and the subsequent polymorphic form. Historically, predicting such complex phenomena has posed a significant challenge for scientists, making this development a considerable breakthrough in the field.

In the next three sections, we provide a description on triacylglycerol (TAG) as a material model to test our hypotheses. Their nucleation kinetics are utilized to assess and improve the current understanding of crystallization form the melt. This model is based

on CNT and considers the effect of temperature change with time (i.e., cooling). We provide a description about the experimental techniques used in this study, differential scanning calorimetry (DSC) and time-resolved synchrotron X-ray diffraction (XRD). These techniques were employed to gather vital data on the crystallization tendencies and structural properties of TAG crystallization. We took a great deal of care in handling and calibrating the DSC instrument to guarantee the reliability of our thermal measurements, which will enable us to accurately determine when crystallization begins (onset temperature of crystallization, T_o).

Furthermore, we place particular emphasis on estimating the melt-crystal interfacial energy (surface tension). As an essential parameter influencing the nucleation process, the estimated interfacial energies contribute to a better understanding of the underlying mechanisms during crystallization. By combining this data with computational simulations, we probe the limits and assumptions of CNT and the transient nucleation regime, further refining our knowledge of these critical phenomena.

1.2 TRIACYLGLYCEROLS (TAGS)

TAGs are triacylglycerol esters produced from glycerol and three fatty acids. Figure 1-1 shows a depiction of the structure of an example TAG (trilaurin). They are the most prevalent lipids in nature and serve as the major source of energy storage in both plants and animals. TAGs are a necessary component of fats and oils, which play an important role in the structure, texture, and stability of a wide range of food goods, cosmetics, and medicinal formulations.

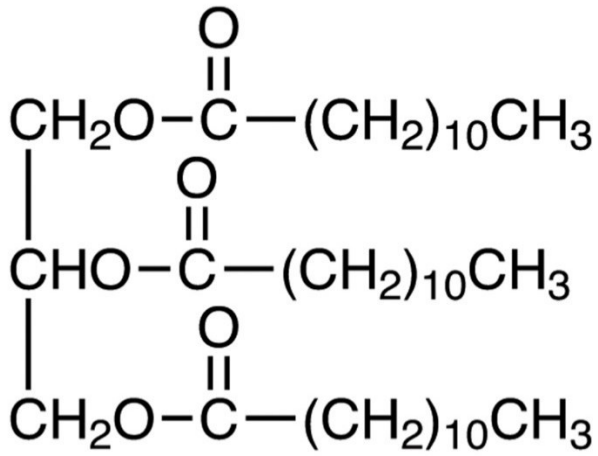

Figure 1-1: Chemical structure of trilaurin (LLL)

1.3 TAG CRYSTALLIZATION

The molecular structure and composition of the fatty acids, as well as their positional distribution on the glycerol backbone, impact the physical qualities of triacylglycerols such as melting temperature, crystallization behavior, and polymorphism. Polymorphism refers to TAG's ability to form multiple crystalline structures, and these structures have distinct properties in terms of stability, melting point, and lattice arrangement.

Non-isothermal conditions refer to processes where the temperature is not constant over time, such as during cooling or heating. In the context of TAG crystallization, non-isothermal conditions are relevant because they represent real-life scenarios where products experience temperature fluctuations during production, storage, and transportation. Thus, understanding the non-isothermal crystallization behavior of TAGs is of great importance for various industries, as it affects the properties, quality, and shelf-life of products that contain fats and oils.

Crystallization is a complex process that involves nucleation, crystal growth. Under non-isothermal conditions, the cooling rate, composition, and presence of other components can significantly influence the crystallization kinetics and final polymorphic forms of TAGs. Understanding and controlling these factors is crucial for optimizing the properties of lipid-based products, as well as for the development of new formulations with improved characteristics.

1.3.1 TAG polymorphism

Polymorphism is the ability of materials to exist in multiple crystalline forms, which arise from the different arrangements of molecules in their solid state. These variations in molecular packing result in distinctive structure-related properties, such as melting point, color, texture, crystal density, stability, solubility, and chemical reactivity. In the case of TAGs, there are three major polymorphic forms observed: α, β, and β'. The classification of these polymorphic forms is based on the lateral arrangement of molecules or sub-cellular packing. Specifically, α has a hexagonal sub-cell packing, β' has an orthorhombic perpendicular packing, and β has triclinic parallel packing. These sub-cell classifications (see Figure 1-2) provide information about the lateral arrangement or the arrangement of hydrocarbon chains with respect to one another in a crystal. In the longitudinal direction, TAG molecules in a crystal appear to have a 'chair' conformation, with a certain tilt or angle existing between the stacked TAG molecules, specific to each polymorphic form.

It is essential to understand that polymorphic forms also impact various properties of the materials they form. For instance, in cocoa butter used in chocolates, at least six polymorphs are present, but only one of them is preferred due to its glossy surface and

suitable melting point for chewing and mouthfeel.[11] This ensures that the chocolate remains solid during storage and melts smoothly in the mouth, providing a pleasurable eating experience.

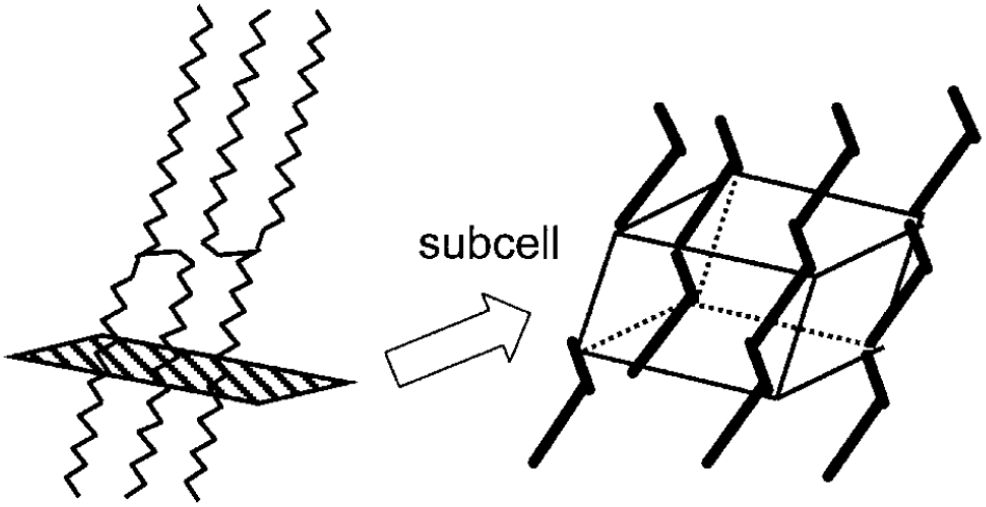

Figure 1-2: Sub-cell structures of TAGs[12]. (Permission is granted)

1.3.2 TAG nucleation and growth

Crystallization is the transformation where highly structured crystals emerge from a less organized system. This process consists of two stages: 1) nucleation of crystals and 2) their growth. The nucleation and growth of crystals are separate stages with distinct kinetics. The nucleation rate quantifies the number of nuclei generated per unit volume per unit time and has a standard unit of $m^{-3} \cdot s^{-1}$. In contrast, the growth rate of crystals is concerned with the change in a crystal's size over time, with a unit of $m \cdot s^{-1}$. For example, research on lithium disilicate ($Li_2O \cdot 2SiO_2$) revealed that its maximum nucleation and growth rates occurred at varying temperatures, emphasizing that these two stages are unique and should be examined separately.[13, 14]

When the temperature of a fat melt is lowered below its melting temperature, it undergoes a process of under (super)cooling.[15] This phenomenon serves as the driving force for the transition from a liquid to a solid state. It is necessary to cool fats by 5-10 °C below their melting point before the crystallization process can start within a viable time frame[16]. The interaction energy between TAG molecules must be greater than the kinetic energy of the molecules in the melt to overcome the Brownian dynamic effects. At the melting temperature, an adiabatic melt would not crystallize. Below the melting point, the melt enters a metastable region characterized by the formation of tiny molecular aggregates known as embryos. Embryos form and break down continuously, though near the melting temperature the net growth is too slow to reach the large critical nucleus size in a practical time scale. For these molecules, it is not enough to simply interact; they must adopt a specific conformation to stack and form a stable nucleus, as shown in Figure 1-3. The adoption of this more stable conformation is a process that takes time. As the undercooling is increased (i.e., at lower temperatures), stable nuclei of a critical size are formed within experimental time scales.

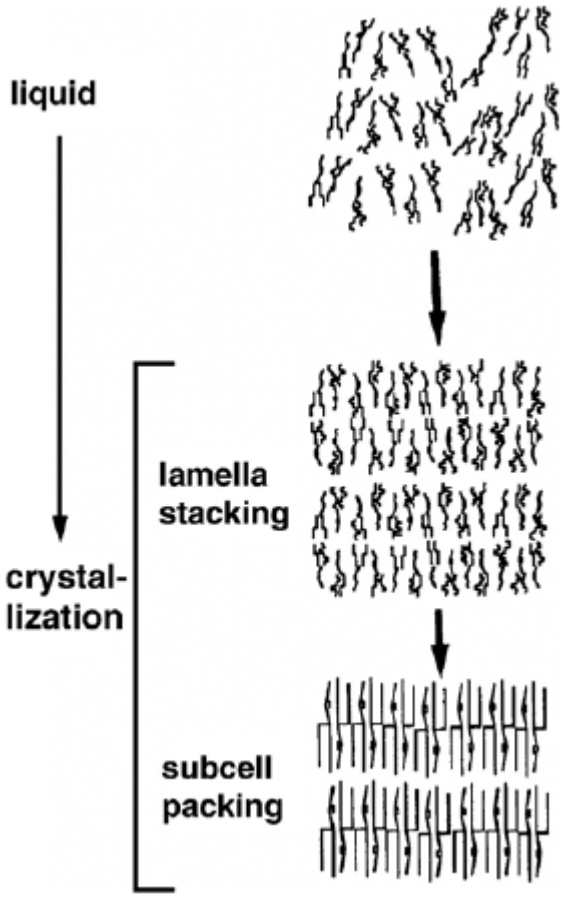

Figure 1-3: Schematic of the ordering process in the liquid state followed by sub-cell packing.[17] (Permission is granted)

The Gibbs free energy change associated with the formation of a crystal embryo (ΔG_n) includes contributions from both surface ($\Delta G_{\text{surface}}$) formation and volume changes (ΔG_{volume}) and can be defined by the following equation (known as Gibbs-Thomson equation [2]).

$$\Delta G_n = \Delta G_{\text{surface}} + \Delta G_{\text{volume}} \qquad 1\text{-}1$$

For a *spherical* shaped nucleus, Equation1-1 can further be re-written as

$$\Delta G_n = 4r^2\delta - \frac{4}{3}\pi r^3 \frac{\Delta\mu}{V_m^s} \quad 1\text{-}2$$

where δ is the solid-liquid interfacial energy (J.m^{-2}), r (m) is the radius, V_m^s is the molar volume of one mole of a crystal (m^3.mol^{-1}), and $\Delta\mu$ is the difference in free energy between the liquid and solid. For single-component systems, $\Delta\mu$ can be regarded as ΔG_c, which is the free energy of crystallization. Hence

$$\Delta G_n = 4r^2\delta - \frac{4}{3}\pi r^3 \frac{\Delta G_c}{V_m^s} \quad 1\text{-}3$$

While keeping the values of δ , V_m^s, and ΔG_c , Equation 1-3 is commonly used to find critical nucleus size, r_c ,that satisfies the condition $(\partial G_n)/\partial r=0$ in the (ΔG_n- r) profile, as seen in Figure 1-4. Before the critical size, the free energy released to form a nucleus is insufficient to overcome that to maintain the nucleus-liquid surface, hence no crystallization could happen. After the critical size, the free energy required to form a nucleus decreases rapidly with increasing radius, indicating that the formation of larger nuclei becomes more energetically favorable. In our study, we took into account that TAG crystals do not adopt a spherical shape during crystallization, as supported by recent findings[18]. To accommodate this observation, we adjusted Equation 1-3 to incorporate the anisotropic Gibbs energy that arises from the platelet-like geometry of the of 3D forming nuclei, which will be discussed in Chapter CHAPTER 3.

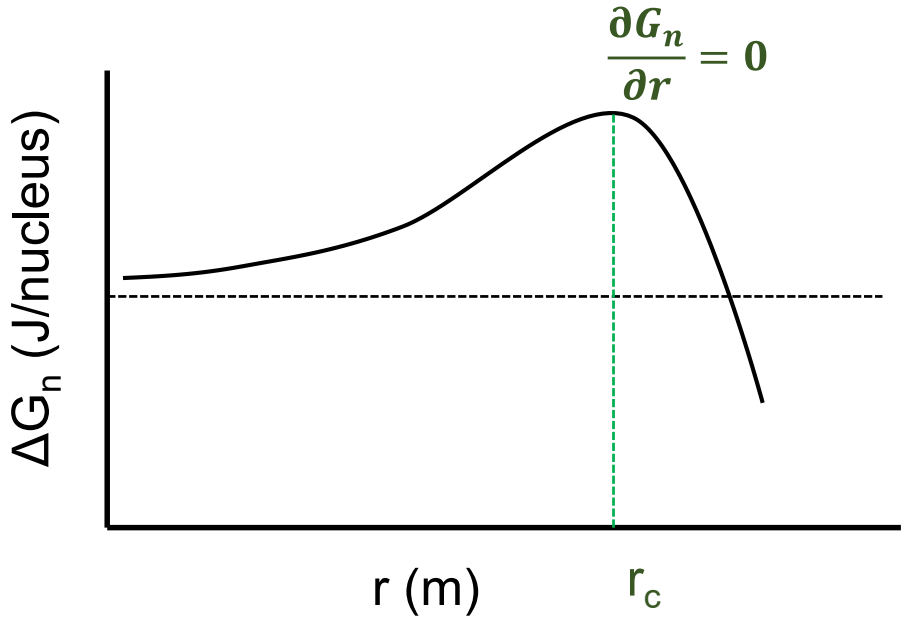

Figure 1-4: Free energy as a function of nucleus radius. The maximum in the profile corresponds to the critical size, r_c, above which stable crystal will form.

Nucleation, the initial step in the formation of a new thermodynamic phase or a new structure via self-assembly or self-organization, can be classified into two main categories: primary and secondary. Primary nucleation refers to the process in which a new phase or structure forms in a system where none had existed before. This type of nucleation itself can be further divided into two types. The first, homogeneous nucleation, occurs when the nucleation process is not influenced by the presence of foreign particles and happens uniformly throughout the liquid or vapor phase. This is when the system spontaneously forms a new phase or structure on its own. The second type, heterogeneous nucleation, occurs on pre-existing surfaces or interfaces within the system. It is characterized by the formation of a new phase or structure being facilitated or catalyzed by the presence of a different phase or structure. On the other hand, secondary nucleation refers to the process where the formation of a new phase is initiated by the existence of a

phase of the same kind. This usually happens after primary nucleation, once a new phase or structure has been formed and can act as a catalyst for further nucleation. In essence, nucleation can either be primary, further divided into homogeneous or heterogeneous, or secondary. Despite its importance in applications, homogeneous nucleation is crucial for studying mechanisms and kinetic modeling, which is the focus of this thesis.

As discussed in Section 1.3.1, crystals can have different structures and polymorphs, so it is important to understand which ones crystallize from a liquid. A fast-nucleating polymorph is more likely to dominate due to the higher number of nuclei that grow, while slow-nucleating polymorphs are less likely to be observed. A fast-growing polymorph may still prevail, even with slow nucleation. Figure 1-5 shows the relationship between Gibbs free energy and temperature for the three major polymorphs of TAGs.

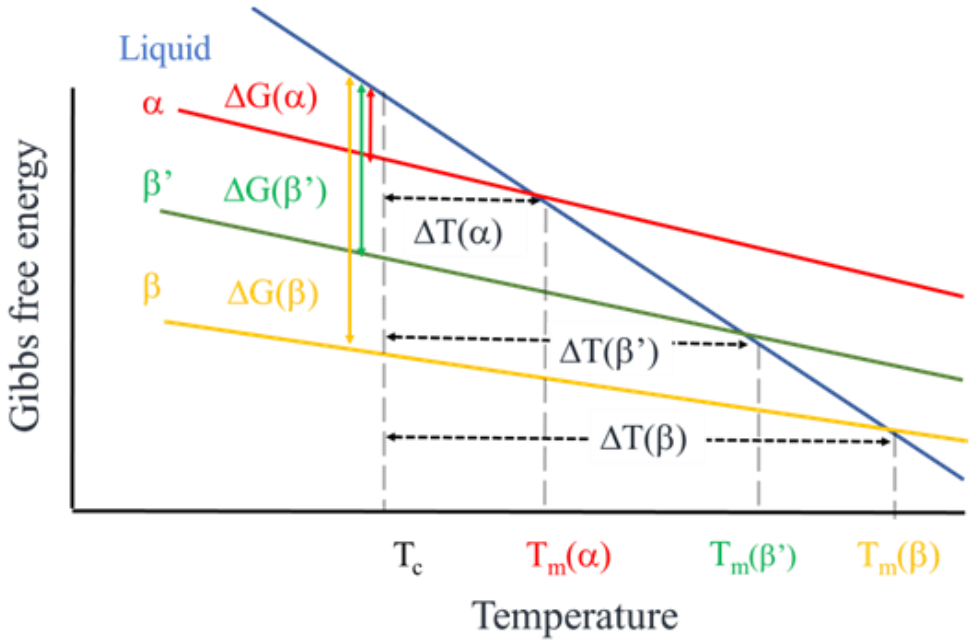

Figure 1-5: Gibbs free energy vs. temperature for the liquid and the three major polymorphic forms of TAGs. The difference of Gibbs free energy (ΔG) and the undercooling (ΔT) for each polymorph are depicted with respect to undercooled liquid at the crystallization temperature, T_c.

There are important factors that affect the crystallization product: thermal stability and cross-nucleation/concomitant nucleation. A fast-crystallizing polymorph may not be the most stable form and could transform during the process. According to Ostwald [19, 20], the least stable polymorph crystallizes first, followed by more stable forms in succession. Cross/concomitant nucleation [21], where a second polymorph nucleates on an initial one, contributes to polymorph diversity in experiments. This second polymorph typically grows faster than the first, dominating the product despite slow independent nucleation. A dominant polymorph must have moderate to fast nucleation and growth rates, remain stable during crystallization, and not cross-nucleate other polymorphs. It's worth noting that crystal nucleation rate is a crucial factor in this process. Understanding cross-nucleation is particularly important. First, from a scientific standpoint, experiments that produce crystals with different polymorphic structures offer structural and thermodynamic information that cannot be obtained when only one phase crystallizes. Second, from a commercial perspective, it is important to avoid process conditions that lead to different polymorphs, as they result in inconsistent materials that do not meet predetermined specifications.

1.3.3 Models used to describe non-isothermal crystallization.

The Avrami model [9] is the most commonly used model to evaluate the isothermal kinetics of crystallization and growth of lipids [22]. It relates experimentally determined kinetics to growth modes and sometimes the structure of the final lipid network. The Avrami equation (Equation 1-4) is formulated as follows:

$$\theta(t) = \frac{C(t)}{C_\infty} = 1 - e^{-Kt^m} \quad \text{1-4}$$

where θ(t) is the relative crystallinity at time *t*, *C(t)* is the absolute crystallinity at time *t*, C_∞ is the final absolute crystallinity, *K* is the crystallization rate constant that includes both the nucleation and growth rates, and *m* is the Avrami index or exponent. Different *m* values represent different types of nucleation, continuous nucleation, growth in less than three dimensions, and heterogeneous nucleation on planar or linear defects. [23]

In industrial applications, crystallization often happens under non-isothermal cooling conditions (i.e., the temperature is decreased as the material crystallizes), resulting in alteration in the physical properties of the end products. Because heat and mass transport conditions evolve as temperature decreases, the nucleation and crystallization rates fluctuate over time. The effect of nucleation behavior on structural properties such as crystal size, crystal shape, and crystalline mass spatial distribution is important to understand.

Several models have been developed to quantitatively describe non-isothermal crystallization. The majority of them are based on the Avrami equation, where the isothermal model is extended with an integral form to account for the time-dependent evolution of temperature, where Equation 1-4 is combined with a rate constant that accounts for the impact of cooling rate.[24] Other models include Ozawa method [25], Harnisch and Muschik method [26], Vyazovkin method [27], Mo method [28], Caze and co-workers' method [29], Malet method[30], and others [31].

Although there are several modifications of the Avrami model, they still suffer certain limitations to model non-isothermal crystallization conditions. Some of these limitations include: 1) The physical meaning of the growth rate constant and the Avrami

exponent cannot be simply related to the non-isothermal case [32]; 2) The applicability of these models is often limited to particular systems or conditions, thereby rendering their predictive capability for crystallization behavior inaccurate for other systems or conditions; 3) Certain assumptions and simplifications, such as constant nucleation and growth rates, are included into the Avrami model and may not always hold true in real-world systems and conditions. This can lead to inaccuracies in predicting the crystallization process; 4) Avrami models frequently fail to adequately represent complicated crystallization dynamics, such as the presence of various nucleation and growth mechanisms, polymorphism, as well as the influence of external factors pressure or the presence of additives.

1.3.4 TAG crystallization and the effect of solid-liquid interfacial energy (surface tension)

The interfacial energy of different polymorphs can have a substantial impact on the nucleation and crystal growth kinetics of TAGs during the crystallization process. A higher interfacial energy polymorph has a greater energy barrier for nucleation and a slower growth rate, whereas a lower interfacial energy polymorph may have a lower energy barrier for nucleation and a quicker growth rate. For example, the α polymorph, the least stable form, has the lowest interfacial energy, enthalpy of crystallization, and melting point temperature, while the β' and β polymorphs have increasing interfacial energy values, heats of crystallization, and melting point temperatures. The occurrence of a less stable polymorph, even when a more stable one has been significantly subcooled, can be attributed to the variations in interfacial tensions among different polymorphs[33]. A minor difference in interfacial tension can lead to a substantial change in the nucleation rate [34],

which typically has a more significant impact than the temperature driving force.

Furthermore, the interfacial energy of a polymorph can affect its stability and proclivity to transform into other polymorphs. Its temperature dependency is a crucial consideration in TAG crystallization since it influences both nucleation and crystal development processes. Interfacial energy may act as a barrier to nucleation, and temperature variations can vary the interfacial energy at the liquid-crystal interface, influencing the critical size of nuclei required for stable crystal formation as well as the overall nucleation rate.

In Chapters CHAPTER 3 **Error! Reference source not found.**and CHAPTER 4, we will provide a comprehensive analysis of interfacial energy calculations in the context of the determined polymorphs. Furthermore, we will investigate the dependence of interfacial energy values on temperature, illustrating how changes in temperature can affect the behavior of different polymorphs. This discussion will help to develop a deeper understanding of the role of interfacial energy in polymorphic systems and offer insights into the factors that govern nucleation and crystal growth kinetics in these systems. Our method presents a sophisticated and superior alternative to the prevailing technique for determining interfacial energy. Traditional approaches rely on two critical assumptions: one, that interfacial energy remains constant, and two, that its value is derived based on the presumption that the nucleation rate is the inverse of the induction time. [35]

1.4 EXPERIMENTAL TECHNIQUES USED TO STUDY TAG CRYSTALLIZATION

There are several experimental techniques used to study the non-isothermal crystallization kinetics of TAGs, including: DSC, X-ray diffraction, nuclear magnetic resonance (NMR), Fourier transform infrared spectroscopy (FTIR), rheometry and turbidimetry. However, the most used techniques are DSC and X-ray diffraction.

1.4.1 Differential scanning calorimetry (DSC)

DSC has emerged as an essential analytical tool for studying TAG crystallization, offering valuable insights into the physical and thermodynamic properties of TAGs and their polymorphic behavior under varying temperature and pressure conditions.

The accurate determination of heat capacity values using DSC is integral to understanding TAG crystallization processes, particularly at temperatures well below the melting point where crystallization predominantly occurs. By obtaining precise heat capacity values, enthalpies at different temperatures below the melting point can be calculated, providing essential information on the energetics of TAG phase transitions, polymorphic forms, and the stability of various crystalline structures. The first premises we based our DSC work on are the followings:

1. Heat capacity values serve as an indicator of the crystalline structures formed and the extent of their solid fraction at a specific time and temperature. By analyzing these values, we can gain determine the proportion of crystals during the crystallization process,

2. Enthalpy values at any temperature can be calculated by finding the integral of the difference in heat capacities between the liquid and solid. This step is important since the enthalpy of crystallization is different from the enthalpy of melting, commonly reported in the literature.

We approached these two premises by analyzing the experimental data obtained from a heat-flux and power-compensated DSCs.

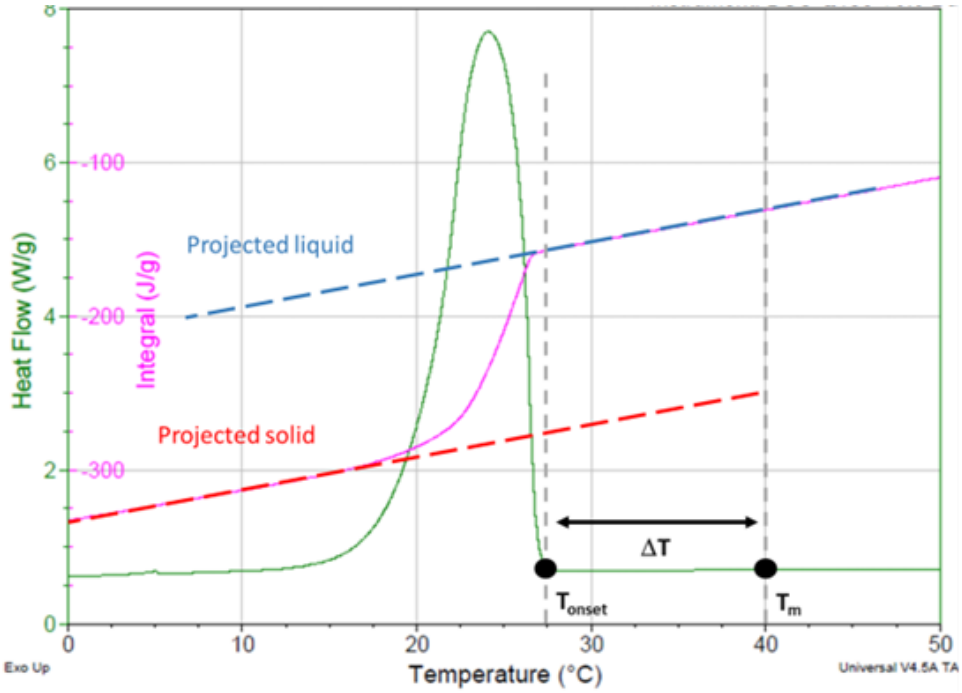

Figure 1-6: DSC trace of MMM sample cooled at 20 C°/min where heat flow signal (green) and the computed running integral (pink) are plotted as a function of temperature.

Figure 1-6 shows a heat flow vs temperature thermogram of a MMM, sample cooled at 20 °C/min. The peak represents the energy associated with crystallizing the sample. The pink line represents the corresponding running integral for the signal. This integral was used to find the enthalpy of crystallization at a given temperature, ΔH_T, as follows.

$$\Delta H_T = \Delta H_m - \int_T^{T_m} \left[C_{pl}(T) - C_{ps}(T)\right] dT \qquad 1\text{-}5$$

This method allows for the calculation of ΔH_m at the melting temperature T_m, given that the heat capacities as a function of temperature in the liquid, C_{pl} (T), and solid, C_{ps} (T), can be experimentally computed with reasonable certainty. In an ideal DSC thermogram, these two functions of the heat capacities can be obtained by projecting a best-fit line in either the liquid or solid sections of the running integral signal (blue and red dashed lines in Figure 1-6). When a molten TAG is cooled, a certain amount of driving force and time are required for the molecules to start aggregating and eventually form a crystal, this driving force is the amount of undercooling ($\Delta T = T_m - T$). The heat capacity term in the right-hand side of Equation 1-6 accounts for the change in enthalpy when ΔH_m is calculated at a temperature other than T_m. This is important as the crystallization takes place at temperatures well below T_m. It follows from Equation 1-6 that the change in entropy at a given temperature, ΔS_T, can also be calculated as follows:

$$\Delta S_T = \frac{\Delta H_m}{T} - \int_T^{T_m} \left[\frac{Cp_l(T) - Cp_s(T)}{T}\right] dT \qquad 1\text{-}6$$

Once the enthalpy and the entropy changes are calculated it is possible to calculate the Gibbs energy using its definition:

$$\Delta G_T = \Delta H_T - T \cdot \Delta S_T \qquad 1\text{-}7$$

As shown in Equation 1-7, the change in Gibbs energy requires the knowledge of both enthalpy and entropy, and these two state functions require the values of heat capacities of the liquid and solid as a function of temperature, as shown in Equations 1-5 and 1-6. With the outlined framework in mind, we initiated experiments on various samples of LLL, MMM, and their binary mixtures to determine their heat capacity values. While this may appear to be a straightforward task, we encountered a significant challenge. Upon conducting numerous DSC experiments, we discovered that the heat capacity measurements were significantly affected by the sample pan's position on the sensors. This variability in heat capacity measurements persisted despite maintaining same variables (temperature ramp, sample size, and the material's liquid state) and adhering to rigorous standards of cleanliness and instrument calibration.

Initially, we thought this phenomenon was exclusive to our DSC instrument; however, similar, or even greater variability was observed when utilizing different DSC instruments from various laboratories. These findings culminated in a published paper in the journal *Thermochimica Acta*, with a comprehensive discussion of the results presented in Chapter 2 of this thesis.

1.4.2 X-ray diffraction (XRD)

X-ray diffraction patterns were acquired to assign peaks to specific polymorphic forms and address any ambiguous cases of polymorph identity. The various polymorphs were identified and compared with literature sources using small-angle X-ray diffraction (SAXD) and confirmed by wide-angle X-ray diffraction (WAXD). The three primary

polymorphs exhibit distinct wide-angle diffraction patterns. The α-phase features a single strong reflection at 0.42 nm. In contrast, the β'-phase is characterized by two prominent reflections around 0.42 nm and 0.38 nm, while the β-phase displays three reflections at 0.46 nm, 0.39 nm, and 0.38 nm.

All the X-ray diffraction data for the current work were done using time-resolved synchrotron X-ray diffraction located in Brookhaven National Laboratories and Argonne National Laboratories. For detailed information about how these data were acquired and analyzed, the reader is encouraged to read these dissertations [36] [37] written by our lab colleagues.

1.4.2.1 Synchrotron X-ray diffraction (XRD)

Synchrotron radiation is generated when ultra-relativistic charged particles are accelerated through magnetic fields in a circular storage ring. Figure 1-7 shows the floor plan of the national synchrotron light source at Brookhaven national laboratory (BNL) where the synchrotron data were obtained.

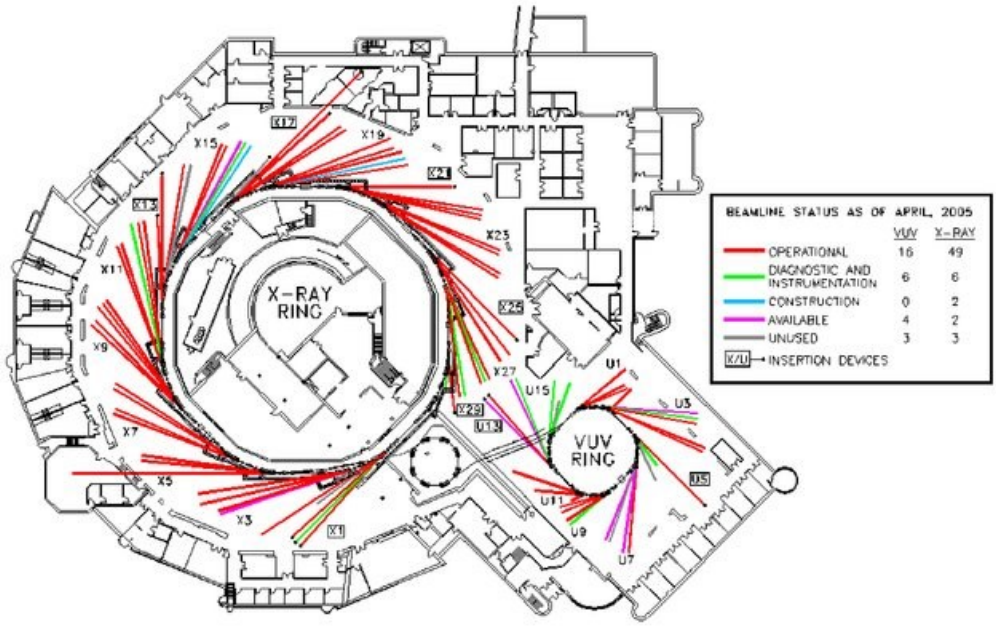

Figure 1-7: Floor plan of the national synchrotron light source at BNL depicting storage rings and beamlines. (Brookhaven National Laboratory)

Synchrotron exhibits higher brightness and intensity compared to conventional x-ray sources. It also possesses features such as high collimation, low emittance, tunability in energy/wavelength, and a high level of polarization.[38] By observing the scattered intensity of an X-ray beam interacting with a sample, various factors such as incident and scattered angles, polarization, and wavelength can be determined. X-ray scattering enables the characterization of time-resolved effects due to its fast data acquisition. A monochromatic x-ray beam interacts with a sample, with some x-rays scattered and others penetrating without interaction. The scattered X-rays are detected by 2-D small and wide-angle detectors perpendicular to the direction of the beam. The detectors are located behind the sample as shown in Figure 1-8.

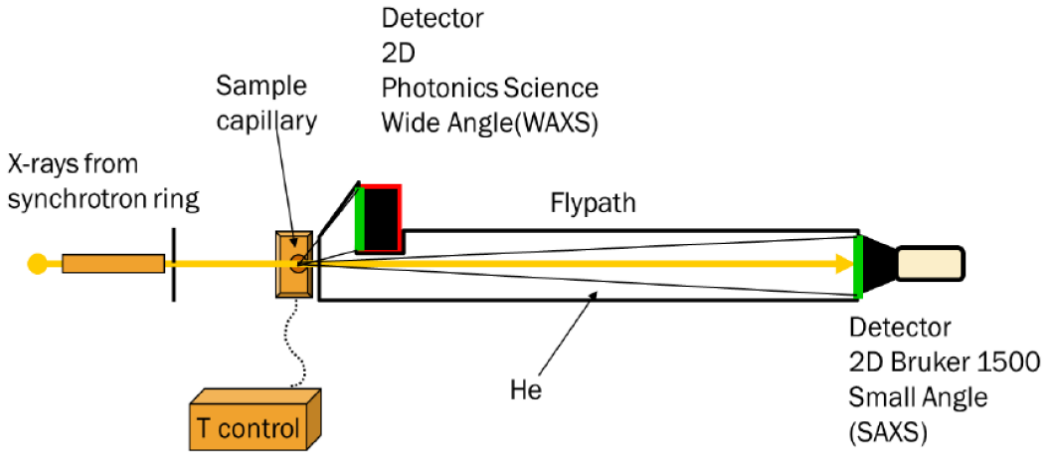

Figure 1-8: Setup for X-ray diffraction performed at BNL (drawing by Dr. Gianfranco Mazzanti).

The main components of this setup are as follows.

1) Sample capillary holder: This goniometer-mounted aluminum holder with a set of Peltier elements for precise sample temperature control. A thermistor (15 kOhm, TS-67, Oven Industries Inc, Mechanicsburg, PA, US) was positioned alongside the capillary to monitor the temperature, providing reproducibility to ± 0.01 °C. Additionally, the holder included an x-ray window.

2) Temperature controller: The temperature control of the system relied on adjusting the voltage across the Peltier elements. A PID (proportional, integral, derivative) algorithm was utilized to compute the voltage applied to the Peltier. A LabVIEW program established the desired temperature profile and provided the set point for the PID algorithm.

3) LabVIEW program: The program, jointly developed by Dr. Gianfranco Mazzanti and Dr. Stefan Idziak, and later improved by Pavan Batchu, was implemented in the National Instruments LabVIEW environment. Its purpose was to control the temperature of the

capillary cell and log temperature and other operating parameters. The program featured a graphical user interface (GUI) that allows users to input a temperature profile, as shown in Figure 1-9. Within the LabVIEW program, multiple parallel loops were employed to dynamically calculate the set point temperature based on the current stage in the temperature profile and time. The calculated set point temperature was then communicated to the temperature controller. The program's key functions included generating a log file for each temperature cycle, recording the time, actual temperature, and set point temperature of the capillary cell. Additionally, it communicated the temperature of the capillary cell to another program responsible for capturing and saving diffraction patterns from one of the detectors.

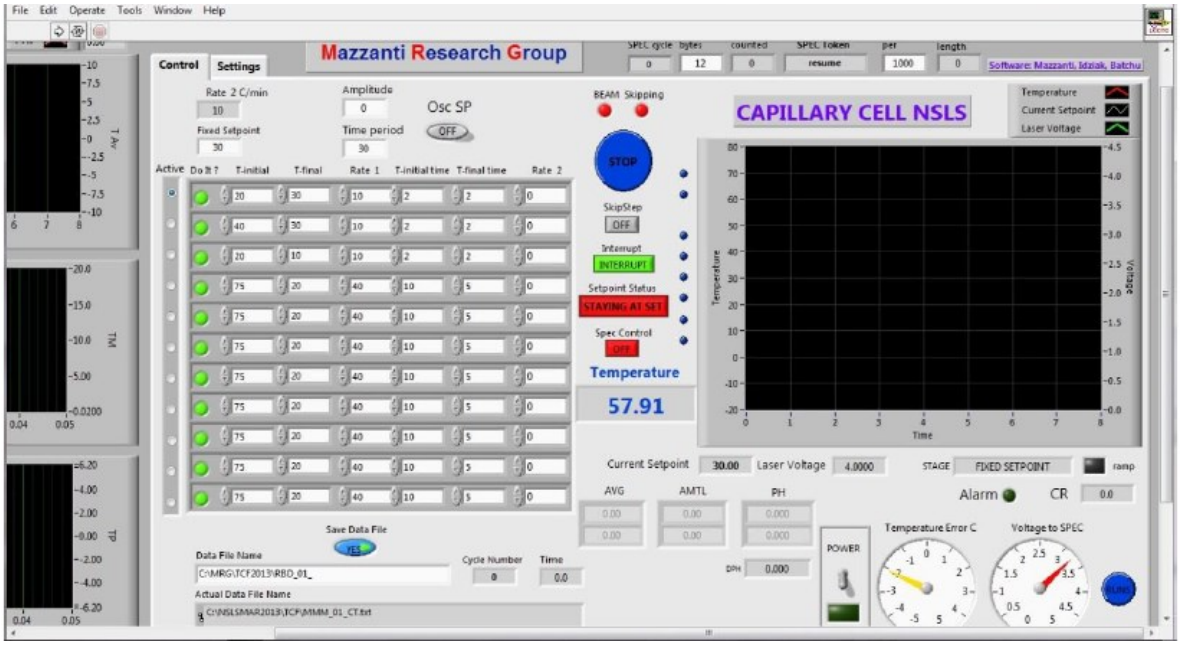

Figure 1-9: A screenshot of the capillary cell temperature control program's GUI showing different functionalities of the program.

3) Small angle diffraction pattern detector: A Bruker 1500 2D detector was employed for capturing diffraction patterns in the small angle region. The detector had a pixel size of 0.2004 mm, and the pixels on the camera are binned to a resolution of 512 x 512. Positioned at a distance of 1059.47 mm from the sample holder, the precise distance between the capillary cell and the detector was determined by analyzing the diffraction patterns of a silver behenate standard. The acquisition of images using this detector was controlled by the 'Bruker Smart' program. To automate the acquisition of diffraction patterns, a program called 'SPEC' interacted with Bruker Smart to acquire and save images for a specified duration. The acquired diffraction patterns were saved after subtracting the 'Dark field image' from each acquired image.

3) Wide angle diffraction pattern detector: A Laue camera, manufactured by Photonic Science in Robertsbridge, East Sussex, UK, was also available as a 2D X-ray detector in the beamline hutch. This special camera is typically used for x-ray backscatter experiments. In our experimental setup, we utilized this camera to simultaneously capture wide-angle diffraction patterns with small-angle diffraction patterns. The camera had a pixel size of 0.3387 mm and was placed at a distance of 341.1 mm from the sample. The precise distance between the sample and the detector was determined by analyzing the diffraction patterns of different orders obtained from an aluminum oxide sample (Al_2O_3). A custom plug-in for the ImagePro software ran independently of the other systems and was used to capture WAXD patterns at constant time intervals as defined by the user.

4) SPEC control: The UNIX-based software, developed by Certified Scientific Software in Cambridge, MA, was specifically designed for controlling and acquiring data from XRD systems. Acting as the centralized control for the beamline hutch equipment, this software controlled various aspects of the experimental setup, including detector and sample post positioning. It also managed functions such as adjusting beam size through slit opening and closing, attenuating the x-ray beam to the desired intensity, and more. An essential feature was its capability to automate the capture and storage of XRD patterns at regular time intervals by communicating with the 'Bruker Smart' software.

X-rays are utilized for imaging crystals through the constructive interference of diffracted X-rays from different atomic layers, resulting in a detectable signal. The directions of scattered X-rays depend on factors described by Bragg's Law.[39] The constructive interference between ray, scattering from adjacent rows of atoms in a crystal, occurs when the incident and reflected angles are equal, as schematically illustrated in Figure 1-10.

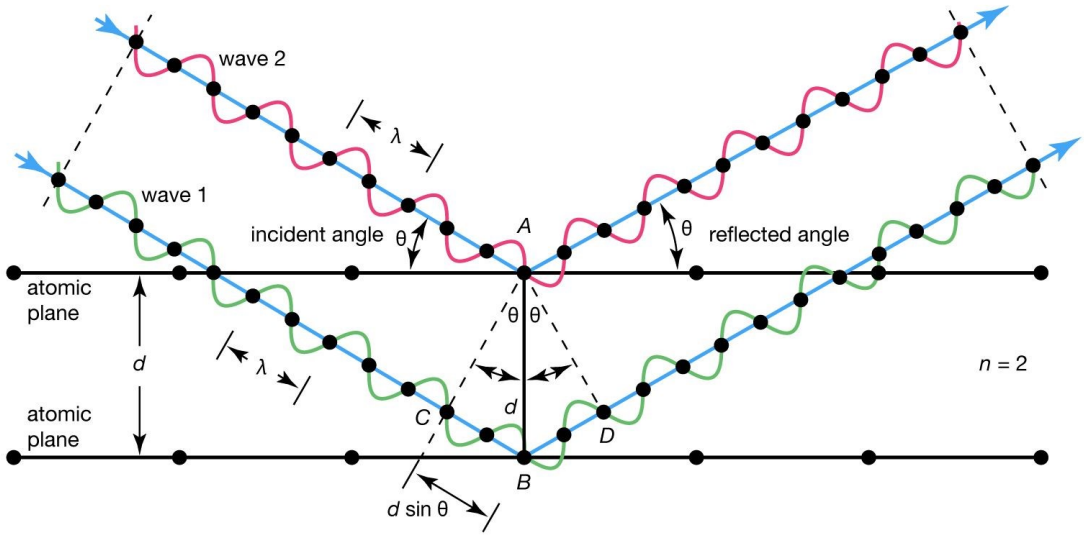

Figure 1-10: X-ray diffraction through a crystal. [40]

The path difference CB+BD represents an integer number of wavelengths, n λ, where n denotes the interference order, and λ represents the wavelength. Constructive interference follows the relationship in Equation 1-9., known as Bragg's law of diffraction. For crystalline materials, the interplanar distance (d-spacing) revealing information about the distances between atoms or molecules is obtained by converting the peak position in reciprocal space into real space using the relation $d = 2\pi/\theta$. This relationship is based on the scattering vector in small-angle X-ray scattering (SAXS) according to Equation 1-8 based on Bragg's equation, Equation 1-9.

$$q = 4\pi/\lambda \quad (1\text{-}8)$$

$$n\lambda = 2 \cdot d \cdot \sin\theta \quad (1\text{-}9)$$

Time-resolved synchrotron radiation x-ray diffraction was mainly used to determine the crystal morphology, phases, crystallization kinetics, and polymorphism for all TAGs.

1.4.2.2 Data processing

Several steps were taken to analyze the diffraction patterns captured at the Synchrotron facility. Firstly, unwarping was applied to eliminate distortions caused during the image transfer from the CCD detector to a chip through a bundle of tapered optical fibers. Filtering was then conducted to address discrepancies caused by defective points on the CCD surface and zingers resulting from cosmic radiation, both of which contribute to noise in the diffraction patterns. Subsequently, each Debye ring was converted into radial plots, representing average radial intensities as a function of the scattering vector 'q'. Precise determination of the center of each Debye ring was crucial prior to this conversion process. Lastly, a normalization procedure was performed on all the radial plots collectively to enable meaningful comparisons.

1.4.2.3 Diffraction pattern analysis

The data analysis involved the utilization of 'Igorpro 6' software developed by Wavemetrics Inc, located in Portland, OR, US. This software facilitated the separation of each diffraction pattern into background and diffraction peaks. The peak fitting process began by providing initial guess values manually. Subsequently, Igorpro employed a Levenberg-Marquardt algorithm to determine the optimal set of parameter values for each fitted distribution function. The objective was to minimize the sum of squared errors between the experimental and calculated patterns. The calculated pattern was obtained by summing the fitted statistical distribution functions along with the background component. Figure 1-11 illustrates different components of the data analysis. The top part displays the residuals, showing the discrepancies between the experimental and calculated patterns. In the center part, the red curve represents the actual experimental diffraction pattern, while the blue curve represents the calculated pattern derived from the baseline function and the two initial distribution functions. The green line/curve corresponds to the baseline function. Finally, the bottom part of the figure provides a description of each of the individual distribution functions that were initially guessed during the analysis process.

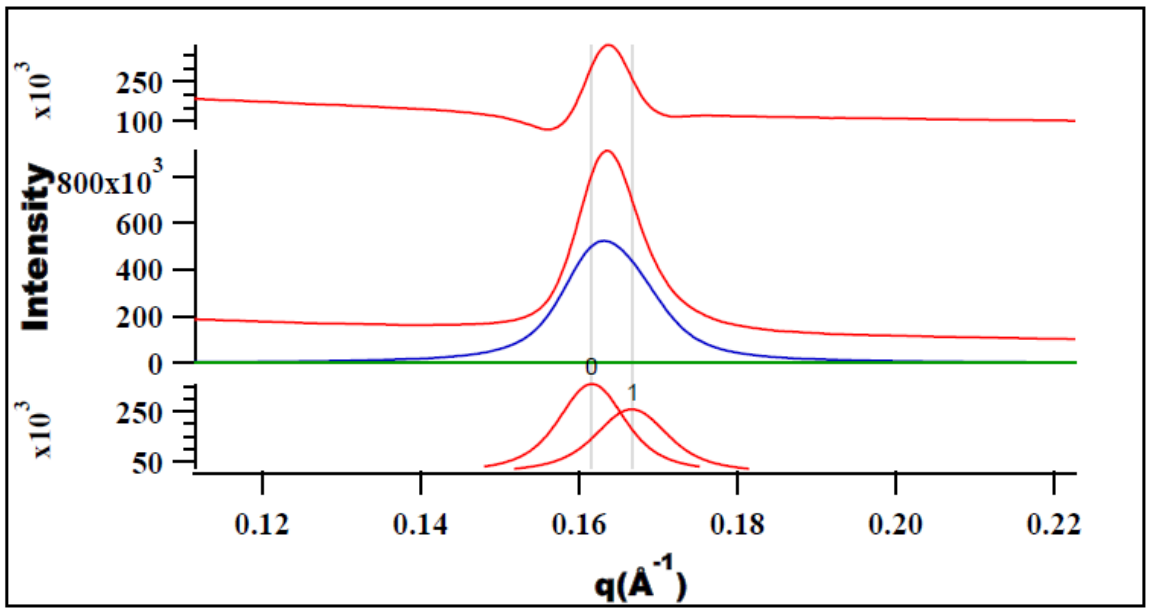

Figure 1-11: A sample diffraction pattern with two guess 'Voigt' peaks on a quadratic background in Igorpro.

1.4.2.4 Types of statistical distribution functions used in peak fitting

A rearranged form of a Gaussian function, Equation 1-10, was used in Igopro to fit the peaks.

$$P_G = y_0 + A.e^{\left[-\left(\frac{x-\epsilon}{width}\right)^2\right]} \qquad 1\text{-}10$$

Where P_G is the peak Gaussian, ϵ is the peak position or the value at which the function has the maximum amplitude, y_0 is the offset of the distribution function, the '*width*' is the full width at half maximum of the function which is $\sqrt{2}.\sigma$, and A is a function of the amplitude.

A Lorentzian function was also used in the peak fitting, which is shown in Equation 1-11.

$$P_L = y_0 + \frac{A}{(x-\epsilon)^2 + B} \quad \text{1-11}$$

Where P_L is the peak Lorentzian, and B is the width and amplitude of the function. The rest of the variables are the same. Sometimes these two functions (Gaussian and Lorentzian) are not good enough to describe the peaks, where a Voight function was used to fit the peaks.

1.5 OBJECTIVES

The primary goal of this study is to develop a comprehensive understanding of the nucleation kinetics of TAGs during the crystallization process, with the overarching question being: "If we have a liquid TAG and we cool it down at a controlled linear cooling rate, how do we predict what polymorph(s) is/are formed? Can we predict at what temperature it/they will form?" This knowledge will contribute to optimizing the crystallization conditions and enhancing the properties of TAG-based products in various industries, such as food, cosmetics, and pharmaceuticals. To achieve this objective, the following specific aims have been identified:

1.5.1 Investigate the nucleation kinetics of TAGs.

This study aims to elucidate the nucleation kinetics of TAGs under various cooling rates. The CNT and Fisher-Turnbull approaches will be employed to determine the nucleation

rates of TAGs. We will determine the onset of crystallization of a trilaurin sample cooled at different cooling rates, paying special attention to details related to DSC calibration and variability associated with using different sample pans and pan placements. The study will also explore the limitations of existing models and propose novel approaches to overcome these limitations.

1.5.2 Investigate the role of interfacial energy in TAG nucleation.

This study will explore the impact of solid-liquid interfacial energy on the nucleation kinetics of different TAG polymorphs. The dependence of interfacial energy values on cooling rates will be investigated, and the effect of these changes on the behavior of different polymorphs will be examined. A comprehensive analysis of interfacial energy calculations will be conducted, and novel methods for determining interfacial energy will be proposed to overcome the limitations of traditional approaches.

1.6 ORGANIZATION OF THIS THESIS

In this dissertation, simulation and computational techniques are used to determine the nucleation rate of β' polymorphs and the subsequent appearance of α polymorphs, offering crucial insights into our present understanding of crystallization kinetics and nucleation processes. The significance of determining precise enthalpy and entropy values

through our proposed framework is highlighted in Section 1.4.1, utilizing heat capacities. Chapter CHAPTER 2 delves into how the pursuit of finding accurate heat capacities has expanded the comprehension of how DSC works and clarifies why obtaining precise heat capacities has been challenging. Chapter **Error! Reference source not found.** presents a m odel based on CNT to compute the nucleation rate for nanoplatelet-like nuclei, as opposed to the more commonly referenced spherical shape in the literature. The identification of emerging polymorphic forms at the onset temperature is achieved using time-resolved SAXD and WAXD data obtained from synchrotron experiments, while their onset temperatures are determined through DSC. Our model incorporates a temperature-dependent interfacial energy and an activation energy barrier reliant on both temperature and the number of molecules in the embryos. In Chapter CHAPTER 4, we build upon the findings from Chapter CHAPTER 3 to elucidate why the α polymorph materializes after the formation of the β' polymorph, which might initially appear to contradict Ostwald's Rule of Stages. Lastly, in Chapter CHAPTER 5, conclusions are offered and recommendations for future work are provided.

CHAPTER 2 THE EFFECT OF THE SAMPLE PAN POSITION ON THE DETERMINATION OF THE SPECIFIC HEAT CAPACITY FOR LIPID MATERIALS USING HEAT FLUX DSC

2.1 PUBLICATION INFORMATION

This chapter is a modified version of a manuscript, originally published as:

Omar Al-Qatami & Gianfranco Mazzanti (2022). The effect of the sample pan position on the determination of the specific heat capacity for lipid materials using heat flux DSC. *Thermochimica Acta*, *710*, 179148

2.2 ABSTRACT

Accurate measurements of specific heat capacity for lipids as a function of temperature, C_p (T), is needed for modelling their crystallization behavior. DSC has been the main technique to determine specific heat for numerous materials, including lipids. Key experimental conditions (heating/cooling ramps, sample size, purge gas, and temperature modulation) that affect the measured heat flow, from which C_p (T) is calculated, have been extensively discussed in the literature. Usually, DSC manufacturers provide what they consider to be the best experimental conditions to measure accurate C_p (T) values with the least uncertainties. The successive nature of this method requires the user to perform each step separately, which means that the user needs to take out the empty pan from the DSC furnace to load either the standard material (usually sapphire) or the sample and place it back again into the furnace. Following this method will result in a different pan

placement on the sensor each time the DSC furnace is opened, which consequently influences the heat flow signals.

This paper is intended to quantitatively evaluate the uncertainties in C_p (T) measurements due to the pan position on a heat-flux DSC sensor. Due to his effect, relative expanded uncertainty U values were ~1.5%, and at least 15-25% as a result of pan placement. The sapphire uncertainty values were much smaller than those from the trimyristin (MMM) sample. With the assistance of Fourier finite-element (FEM) simulation, the effect of the different thermal diffusivity of MMM and sapphire on the C_p (T) measurements is elucidated.

2.3 INTRODUCTION:

The specific heat capacity at constant pressure, C_p, is one of the fundamental thermophysical and thermodynamic properties that characterizes the physical state of materials. It is an essential parameter for the calculation of thermodynamic functions. The knowledge of C_p is also necessary to establish energy balances, obtain enthalpy and entropy values, and evaluate the temperature effect on phase equilibria. It also serves as a sensitive indicator of any structural changes to the material during phase transition. Thus, the determination of accurate C_p values as a function of temperature has acquired much attention in the literature.

DSC has been extensively and widely used as the main instrument to determine C_p for many materials. For lipids and TAGs, DSC has been used to determine C_p a function of temperature, in both solid and liquid states. [41-54]

To get a sense of the reported C_p values as a function of temperature in the literature, C_p

(T) data for liquid trimyristin, MMM, and soybean oil are shown in Figure 2-1and Figure 2-2, respectively. Similar trends have been reported for other TAGs and oils. For example, see references [51, 53] for tricaprin (CrCrCr), tricaprylin (ClClCl) and tricaproin (CoCoCo); and references [43-45, 47, 53, 54] for trielaidin, EEE, trilaurin, LLL, tripalmitin, PPP, and tristearin, SSS. The same behavior was observed for several vegetable oils such as sunflower, olive, walnut, and sesame oil in reference [50] and rapeseed and corn oils in reference [41].

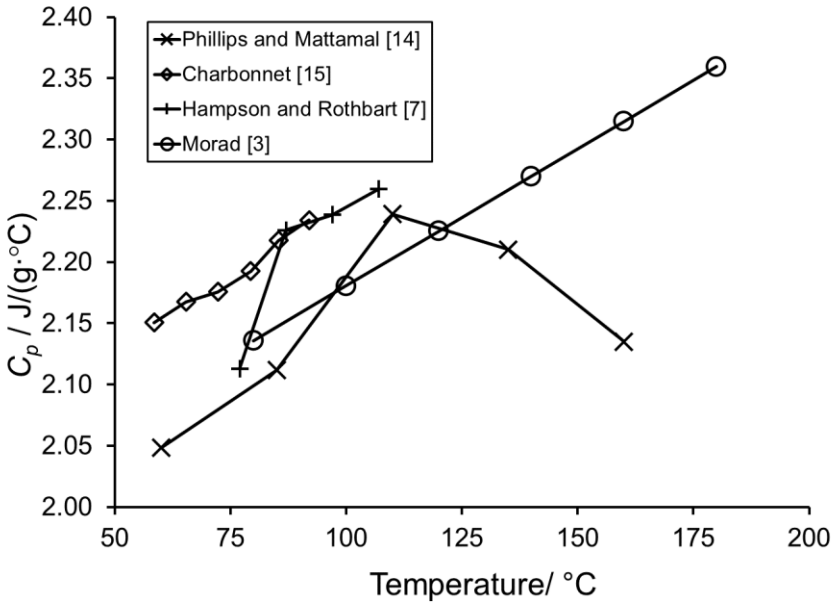

Figure 2-1: Reported C_p (T) values for liquid MMM. [46, 53-55]

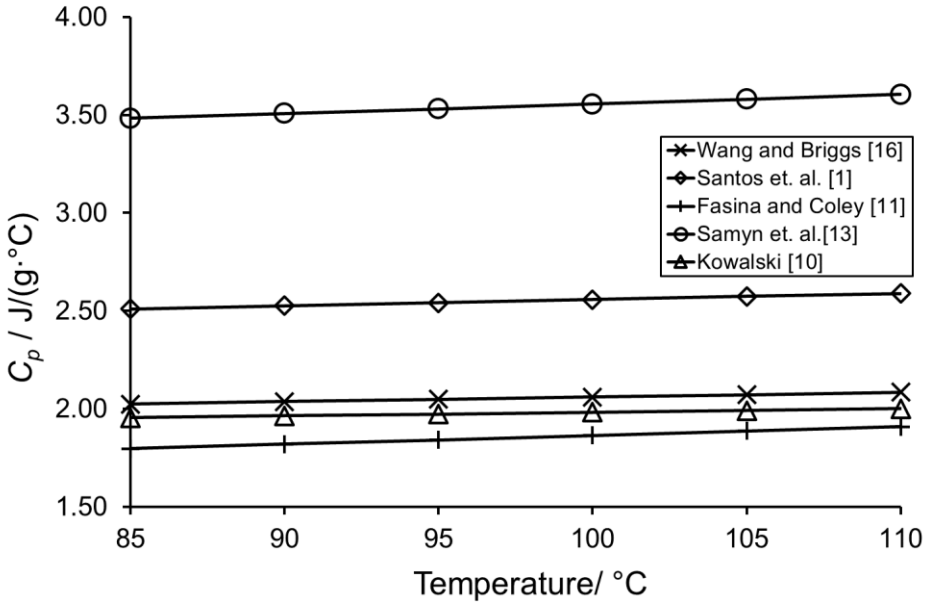

Figure 2-2: Reported C_p (T) values for soybean oil as a function of temperature. [41, 49, 50, 52, 56]

Figure 2-1 and Figure 2-2 show the variability in C_p (T) reported in the literature for MMM and soybean oil respectively. This variability makes it difficult for one to choose the values to be used, for example, in thermodynamics modeling. It is hence important to study why such discrepancies in C_p (T) values are reported in the literature. Possible reasons could be related to the DSC instrument used, the sample and/or the user. Instrumental factors include calibration procedures, heating/cooling ramps, type and flow rate of purge gas, and the type of pans used. For example, Table 2-1 shows the instruments and samples conditions used to obtain the values in Figure 2-1and Figure 2-2. Sample-related factors include thermal contact between the sample and pan, the state of the sample (solid, liquid, multiphase), heat transfer characteristics (heat conductivity/ diffusivity/ capacity), the mass of the sample, and the configuration of the sample in the pan (flat, powder, irregular).

Table 2-1: DSC instruments, heating ramps, and sample sizes used to obtain the data used in Figure 2-1 and Figure 2-2

DSC	Heating ramp/	sample size/ mg	Ref
Soybean Oil			
Predictive model using Rowlinson–Bondi equation	N/A	N/A	[57]
Shimadzu DSC-50	10	22	[41]
TA Instruments DSC-Q100	20	8 to 10	[50]
TA Instruments DSC-Q2000	10	5	[52]
DuPont 990 DSC	20	"several milli-grams"	[49]
MMM			
Semi adiabatic copper calorimeter	0.5	not mentioned	[54]
DSC-1B, PerkinElmer	10	10	[53]
DSC-1B, PerkinElmer	10	10 - 23	[46]
Seiko heat-flux DSC	17	21	[55, 58]

DSC users could also contribute to this discrepancy by introducing unintentional contamination in the sample, or in the DSC furnace (sample leak from the pans). The question is: if all the factors above were thoughtfully considered, why are there still discrepancies in the C_p (T) found?

Careful calibration of DSC instruments is a prerequisite to attain reliable quantitative heat flow signals from which C_p calculations are performed. To achieve proper calibration, one needs to understand the principles of a metrologically accurate calibration, rather than just trust a standard general calibration process. For instance, it is important to understand why some DSC instruments only allow a certain range of temperature ramps to be used in the calibration process, although these ramps could be different from those used in the actual experiments. A case in point, in TA Instruments Tzero^{TM} Q series DSCs, the calibration can only be performed with temperature ramps between 10 and 200

°C/min, even if the experiments will be conducted at 5 °C/min. In the work of Morad *et al.* [58], the optimum experimental conditions to obtain reproducible C_p values were determined for their heat-flux DSC instrument with liquid LLL in a temperature range from 50 to 150 °C. These parameters were found to be a heating ramp of 17 °C/min, a sample mass of 21 mg, and a nitrogen purge flow rate of 50 mL/min. Reproducible C_p values of TAGs were obtained with a precision of ±1% (n=4) in this work of Morad *et al.* [58]

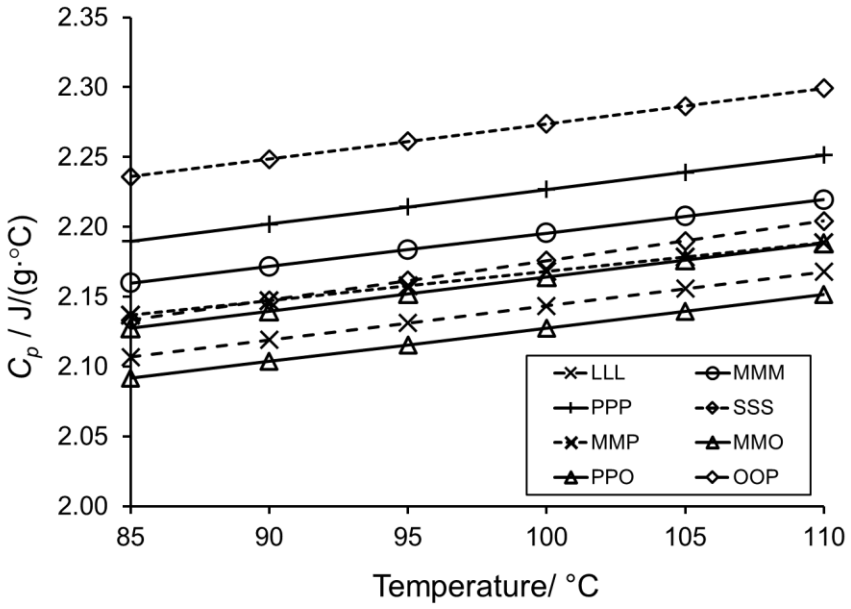

Figure 2-3: The C_p (T) for some mono- and mixed -acid liquid TAGs, as reported by Morad *et. al*. [58] The linear trends of the data are also shown.

Morad *et al*. [58] measured the C_p values of four monoacid TAGs including LLL, MMM, PPP, and SSS and four mixed-acid TAGs including 1,2-dimyristoyl-3-oleoyl (MMO), 1,2-dimyristoyl-3-palmitoyl (MMP), 1,2-dipalmitoyl-3-oleoyl (PPO) and 1,2-dioleoyl- 3-palmitoyl (OOP) using a Seiko DSC 220 heat-flux instrument. These data are presented in Figure 2-3.

Between 50 and 150 °C, the relationship between the C_p of the liquid TAGs and temperature followed a linear relationship, with excellent goodness of fit.[58] The accuracy of the values was not discussed in Morad's work [58]. Accuracy is evaluated by the closeness to reference values. Yet, "accurate" C_p values for TAGs and lipids have not been unambiguously reported in the literature. The "optimum" conditions suggested by Morad *et al.* [44] are instrument dependent, meaning that they do not necessarily apply to other DSCs. Morad's work indicates that there is no universal sample size and temperature ramp for the determination of reproducible C_p values with heat-flux DSCs but rather parameters that are optimized to obtain "precise" measurements that are presumed to be "accurate." For example, Morad [44] selected 21 mg for the sample size because it is recommended by the manufacturer, which is half of the capacity of the pan. However, this amount is too large for the TA instruments hermetic pans used in DSC Q100.

The work of Morad emphasized the importance to select the proper experimental conditions to obtain optimal heat flow signals. It is worth discussing them here to put the scope of this study into context. Some of these conditions are inter-related so they will be paired together.

2.3.1 Sample size and temperature ramp

The selection of the heating ramp depends on the sample size used, *i.e.,* there is an optimum heating ramp for each sample size. To obtain a strong signal to calculate C_p it would be ideal to use large sample sizes and fast temperature ramps. This, however, leads to a broad temperature gradient in the sample and hence yields erroneous C_p values. Furthermore, faster temperature ramps usually require more transient time before the actual

temperature ramp stabilizes to the programmed ramp value. Therefore, the sample size and temperature ramp must be optimized for the type of instrument used. The optimum values should be selected using a model (mathematical logic) that considers the thermal properties of the sample and of the sample containers (e.g., thermal conductivity) to minimize the thermal lag. Schick [59] showed that, as expected, the sample mass should scale inversely with the temperature ramp. For slow ramps, it is recommended to use larger sample masses to get a good signal-to-noise ratio whereas a small amount of sample should be used at faster ramps to minimize the thermal lag effect.

2.3.2 Purge gas/flow

A purge gas is used during DSC experiments to provide an inert atmosphere to the DSC cell as well as rid the cell from any off gases from the sample; these conditions are important to attain reproducible measurements. The most used gases are nitrogen, helium and argon with a typical flow rate range from 25 to 50 mL/min. The thermal conductivity of helium gas (157 mW/(m·°C) at 27 °C) is six times larger than that for nitrogen (26 mW/(m·°C)), which makes nitrogen a good thermal insulator and helium a good conductor. Hill et al. [60] showed that the C_p (T) values computed for a sapphire sample were lower when helium was chosen as the purge gas instead of nitrogen. This observation was explained by the relatively faster dissipation of heat from the sample due to the higher thermal conductivity of helium. It was report in a study that different purge gases significantly influenced the uncertainty in the measured C_p values using sapphire spacers.[61]

2.3.3 Configuration of the sample, pan, and sensor and the resulting thermal contact conductance.

The effect of the configuration of the sample, the pan, and the sensor on the heat flow is manifested in the heat transfer characteristics of the interfaces. Thermal lags are the result of the heat transfer resistance in these interfaces. Some resistance exists at the interface between the sensor and the pan and between the pan and the sample. An additional resistance exists within the sample itself. If the sample is not evenly distributed across the pan, then more heat flux is delivered to areas with less sample material than those with more materials over a given time interval. Höhne and Gloggler [62] discussed the effect of the position of the sample in the sample pan on the temperature difference between the sample and reference furnaces. They [62] mentioned that "… a temperature gradient in the bottom of the sample holder leads to different temperature reading using different positions of the sample or different sample pans. The [63]consideration of these rather small effects leads to a distinct increase in the accuracy and precision of the instrument." Their experiment was done to measure the heat of fusion using a power compensated DSC for three samples: indium, lead, and zinc with thermal conductivity values, *K*, as approximately 80, 35, 116 W/(m·°C) at 27 °C, respectively. However, for metal liquid samples, the temperature gradient discussed by Höhne and Gloggler would be very small in all samples. The gradients in TAGs are expected to be much larger since their *K* values are much lower, *ca.* 0.2 W/(m·°C). Hatta *et al.* [64] suggested that certain length of the sample (thickness) should be used in order to obtain accurate heat capacity measurements (within 1%) using MDSC. They pointed out that even when the thickness requirement is met, it is important to consider the effect of the heat transfer conductance between the sample and

the pan, and that between the pan and the sensor, as they considerably cause deviation to the measurements. Xu *et al.* indicated that [65] the heat capacity of the sample and the calibration reference material should be very close to obtain accurate heat capacity results. They related this observation to the high thermal gradient profile in the sample itself which significantly changes the heat flow signals each time the sample was run. In this study, heat capacity values for MMM sample are almost 2.5 times larger than that of the sapphire, so uncertainty to the measured values was to be expected.

The pan type and the crimping method contribute as well to the flow of heat from the sensors to the sample. It is ideal to have a flat pan bottom to enhance the thermal contact in the sensor/pan interface. Hill *et al.* [60] found that C_p (T) measurements for a sapphire disk were reproducible when open, hermetic and non-hermetic pans were used. However, they found that the C_p (T) measurements obtained from TA instruments pans were less reproducible compared to the Perkin Elmer ones. They attributed this finding to the relatively high pan mass of TA instruments pans (*ca.* 57 mg), compared to that of Perkin Elmer (*ca.* 26 mg). They also noted that the poor reproducibility of the C_p (T) values was not due to the flatness of the bottom of the pans. However, the flatness of the pans used in the work of Wunderlich and Varma-Nair [66] was the key to obtain reproducible and reliable C_p (T) measurements due to the improved thermal contact. The same conclusion was also attained elsewhere [67].

Wunderlich and Varma-Nair [66] attempted to measure C_p (T) for a lubricant oil, heptadecane, and water in the liquid state in the temperature range 37 – 87 °C using a TA instruments DSC 2910, and the samples were contained in TA instruments hermetic pans. The error percentage in the measurements was similar between water and heptadecane (3

to 6 %), but this error was at least twice as much for the lubricant oil (13%). They concluded that it was impossible to reliably measure C_p (T) in the liquid state with this instrument.

2.3.4 Temperature modulation

Modulated differential scanning calorimetry, MDSC, has been extensively used in the literature to measure C_p (T), and its effectiveness has also been closely evaluated. The selection of the proper temperature modulation variables of amplitude and frequency is the key to obtaining accurate C_p (T) measurements. The selection of the modulation variables is to be determined based on the sample size, temperature ramp, purge gas, and pan type. The benefits of MDSC over conventional DSC and its applicability and effectiveness to obtain absolute C_p (T) values has been strongly debated in the literature. The main controversy is about the modulation amplitude and the resultant heat flow. Verdonck *et al.* [68] concluded that MDSC enables the separation of any overlapping phase transitions and computes the thermal conductivity of insulating materials; however, MDSC should not be used as a replacement for conventional DSC when investigating an unknown material [68]. Cao *et al.* [69], however, indicated that MDSC is incapable of determining C_p values, contradicting the work of Wunderlich *et al.* [70] who concluded that the C_p of a material could be directly measured by MDSC. Cao *et al.* [69] concluded that the ability to separate the reversing and non-reversing heat flow signals is artificial. . Cao *et al.* [69] also noted that terms like “reversing” and “non-reversing” are misleading, and the frequency used in the modulation does not mean the frequency of crystal lattice vibration occurring in the sample and therefore is not probing directly such lattices. The debate remains open, even

if a large body of authors who use MDSC choose to ignore it in their publications.

When the effect of all these factors are carefully considered, C_p (T) measurements uncertainties are reported within 3- 5% [62], 1.5 % [71] and even 1% [72]. These studies, however, did not discuss the influence of the position of the pan on the sensor on the measured heat capacity values. Furthermore, they have been conducted with materials whose thermal diffusivity is much larger than that of liquid TAGs. Therefore, this work aims to demonstrate and quantify the affect of the placement of pans on DSC sensors (sample or reference) on the calculated C_p values using both good and poor thermally conductive materials. To show this variation, the C_p values for a MMM sample were calculated. This effect was tested by loading the sample pan into the furnace, applying a temperature ramp, taking the sample pan out of the DSC furnace once the run was finished, then reloading the sample pan back in again and repeat the procedure. This process was performed while keeping the other experimental conditions exactly the same, and the reference pan was never moved unless otherwise stated for different type experiments, *i.e.*, testing the effect of the reference pan placemen on the reference sensor. All the measurements for the MMM sample were conducted while the sample was in the liquid state. Having it in the liquid state is important to avoid the complexity associated with polymorphism that appear when this material crystallizes. Additionally, having the sample in the liquid state ensured that thermal contact between the sample and the bottom of the sample pan was optimum, as recommended by Merzlyakov and Schick [73].

2.4 EXPERIMENTAL

2.4.1 Materials

Trimyrsitin (MMM) sample was purchased from Sigma Aldrich (product number: T5141) with purity ≥ 99% determined with gas chromatography (GC) and used without further purification. The sapphire sample used from the TA Instruments MDSC® kit (TA Instruments MDSC® Sapphire Calibration Kit, part number: 970370.901).

2.4.2 DSC instruments

The experiments were performed using two heat-flux DSC instruments, DSC Q100 and DSC Q200 (TA Instrument, New Castle, DE, US). The DSC Q100, used a refrigerated cooling system (RCS) vapor compression refrigerant as the main coolant. N_2 was used as purge gas. The DSC Q200 used liquid N_2 as a coolant, LNCS, and He was used as purge gas. The flow rates for the nitrogen and helium gases were 50 and 25 ml/min respectively.

2.4.3 Calibration

The same calibration materials and procedure were used to calibrate both instruments, except for the sapphire disks. Each of the two instruments was calibrated for its resistances and capacitances using its sapphire disks. All the aluminum pans used were hermetically sealed and mass matched to ± 0.005 mg of the same reference pan. This was done to optimize the measured heat flow signal for C_p measurements.

Prior to calibrating the DSC instruments, it was ensured that the DSC furnace and the two sensors were cleaned using a fiberglass brush, and the residues were subsequently

removed using clean compressed air. To verify the efficiency of the cleaning process, an empty cell run (no sample or reference pans) was conducted from -60 to 250 °C using a cyclic temperature ramp (heating and cooling) of 20 °C/min. If further cleaning was required, a cotton swab dampened with acetone was used to clean the cell. Subsequently, a dry cotton swab was used to dry off the cell followed by an empty cell run to verify that all contaminants were removed. If the cell was still contaminated, the cell was "burned out" as a last resort to remove all the contaminants by heating the cell to 550 °C with dry clean air as the main purge gas. A cyclic run was conducted before the calibration process to ensure cleanliness and minimize the "first run effect", as suggested by TA Instruments, over the temperature range -60 to 250 °C, to verify that all contaminants have been eliminated. Calorimetric measurements usually drift from zero baseline during the first run compared with subsequent runs under the same conditions. It has been suggested that the first temperature measurement is systematically higher than the subsequent ones due to improved heat transfer between the sample and the bottom of the crucible in the later runs.[74]

To allow the instrument electronics to reach "equilibrium" and get rid of the air in the furnace, the instrument was turned on at least 30 min before the experiments at a nitrogen flow rate of 25 mL/min. Subsequently, the instrument was calibrated using the "calibration wizard option" where the T4 heat flow option "cell resistance and capacitance, cell constant, and temperature calibration" was selected. The T4 heat flow procedure compensates for subtle differences in thermal resistance and capacitance between the reference and sample sensors in the DSC cell, i.e., corrects for the asymmetry between the reference and sample sensors.[75]

DSC Q100 incorporates Tzero™ heat flow theory which is composed of four terms as follows:

$$Q = \frac{\Delta T}{R_r} + \Delta T_0 \left(\frac{1}{R_s} - \frac{1}{R_r}\right) + (C_r - C_s)\frac{dT_s}{dt} - C_r \frac{d\Delta T}{dt} \quad 2\text{-}1$$

where Q is the heat flow rate (W/g), DT is the measured temperature difference between the sample and reference calorimeters, DT_0 is the measured temperature difference between the control sensor and the sample calorimeter, T_0 is the control temperature, R is the sensor thermal resistance, C is the sensor heat capacity and subscripts r and s represent the reference and sample, respectively [75]. This calibration method includes three separate calibration runs. The first is performed with an empty cell, and the second with two sapphire discs (TA Instruments Tzero™ Calibration Kit, part number: 970345.901) with similar masses to determine R and C values for the reference sample sensors in Equation 2-1. The first two runs are heated through the same heating range at 15 °C/min. The third calibration run involves running indium as a standard with known enthalpy to determine the cell constant. The cell constant is a correction factor calculated by dividing the theoretical enthalpy value of indium by the one measured during the calibration process.

It should be noted that Q in Equation 2-22-1 is a combination of two heat flow values Q_s and Q_r ,and is calclated as follows [76]

$$Q = Q_s - Q_r \quad 2\text{-}2$$

where Q_s and Q_r are calculated as follows

$$Q_s = \frac{(T_0 - T_s)}{R_s} - C_s \cdot \frac{dT_s}{d\tau} \quad 2\text{-}3$$

$$Q_r = \frac{(T_0 - T_r)}{R_r} - C_r \cdot \frac{dT_r}{d\tau} \qquad 2\text{-}4$$

Heat resistances and capacitances are obtained during the calibration process to account for any differences in the heat flow between the two sensors, sample, and reference sensors, due to possible manufacturing imprecision. This will consequently provide a signal close to 0 W/g if a run is conducted in an empty furnace.

Hence heat flow, Q, in Equation 2-1 should only result from the measured temperature values, T_s, T_r and T_0. Both, T_s, T_r are measured using type E (chromel-constantan) area thermocouples fixed on the underside of the sensors; T_0 measures the furnace temperature. As in any heat-flux DSCs, the difference in heat flow between the two sensors will result in the change in the measured temperatures that used again by the analyzer to calculate Q in Equation 2-1. This difference is produced from a combination of effects on the heat flow resistance / conductance and capacitance from both sensors.

2.4.4 Specific heat capacity determination

All experiments were conducted at a heating ramp of 15 °C/min, which is the same ramp used in the calibration process. In the case of DSC Q100, heating ramps of 10, 15, and 20 °C/min are recommended to obtain representative values of the calorimeter's calibration parameters (ΔT and ΔT_0) during calibration. According to the DSC Q100 manufacturer, any ramp lower than 10 °C/min will not produce reliable heat resistances and capacitances for the sensors.

The values of specific heat C_p in this work were obtained following the procedure

described and illustrated in detail by the ASTM-1269 standard [77]. This *modus operandi* is known in the literature as the classical three-step method [74]. The measurement involved three consecutive runs under an identical thermal regime. This regime used in this work was iso-scan-iso with heating and cooling ramp of 15 °C/min.

In the first run, the heat flux was recorded using two empty pans mass-matched within 50 µg. The second run was carried out with a sapphire disc. The C_p values of sapphire are well known over a wide temperature range [78]. Sapphire has a relatively good thermal conductivity [~ 24 W/(m·°C)]. The sapphire disc was placed in the sample pan, where it had a good thermal contact with the bottom of the pan. The pan was then placed on the sample sensor of the DSC and the same temperature ramp used in the first step was repeated.

Finally, the sapphire sample is replaced by a known amount of a sample with unknown C_p and the same temperature ramp is run again. The same two pans should be used throughout the procedure.

A MMM sample was placed in a TA Instruments hermetic pan and measured within ± 0.005 mg using a Cahn microbalance (model C-33, California, US). All the DSC measurements to determine C_p were carried out in the liquid state over a temperature range of 55 - 120 °C. This temperature range was selected to ensure that the sample remained in the liquid state and avoid complex crystalline behavior.

The three signals (baseline, sapphire, and sample) from which heat flow values were extracted are shown in Figure 2-4. The instant C_p values at each temperature were calculated with the following equation, using the three-step method: [74, 79]

$$C_p = \frac{Q_s - Q_e}{Q_r - Q_e} \cdot \frac{m_r}{m_s} \cdot C_r \qquad 2\text{-}5$$

where Q is the absolute heat flow signal (mW), and m is the mass (mg) of the material. C_r is the specific heat of sapphire at the temperature at which C_p is calculated. The subscript e represents the heat flow from the empty pan.

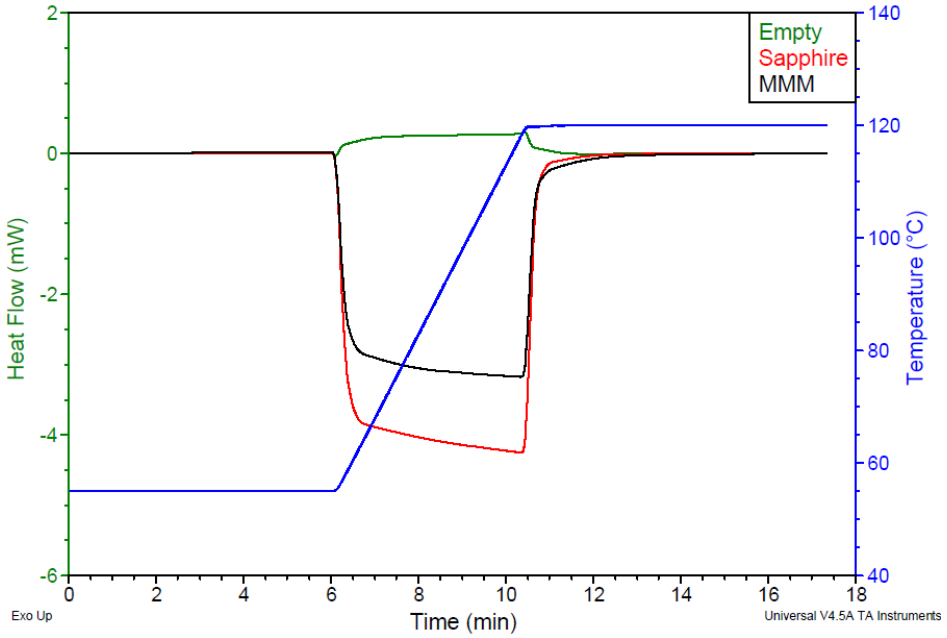

Figure 2-4: Example of normalized heat flow signals (baseline, sapphire, and MMM) as a function of time, obtained from a heat flux DSC Q100. The signals were used to determine C_p using Equation 2-5.

When possible, the same pan should be used in the three runs, i.e. empty pan, sapphire, and the sample. In these experiments, however, a different pan was used for each material (empty, sapphire, MMM) since they had to be hermetically crimped. To reduce variability due to the use of different pans, each pan was mass matched to ± 0.005 mg of the same single empty reference pan.

Each cycle included heating and cooling the sample at 15 °C/min. Each of these heating and cooling ramps was preceded and followed by isothermal periods. The

isothermal periods were used to perform a normalization process of the three signals, as explained in detail by Hesse [80]. It is important to apply this normalization to these isothermal segments to account for the variations in the heat flow signals introduced by the operation of the DSC at different temperatures and in between runs. It is also intended to minimize variability caused by take-out-put-back of pans, as illustrated by Sarge and Poessnecker [67]. The successive nature of this method requires the user to perform each step separately, which means that the user needs to take out the empty pan from the DSC furnace to load either the standard material (usually sapphire) or the sample and place it back again into the furnace. Following this method will result in a different pan placement on the sensor each time the DSC furnace is opened, which consequently influences the heat flow signals.

Once the run was done, the sample pan was taken out of the furnace and then put back in, carefully placing the pan on a position as concentric as possible on the sample sensor. The run was then started.

2.5 RESULTS AND DISCUSSION

2.5.1 Sapphire

The pan placement effect was first evaluated for a sapphire sample because its thermal properties are well characterized and documented over a wide range of temperature [78]. These values were compared to the experimentally determined C_p (T) to evaluate for accuracy. In this set of experiments, the same sapphire disk of 21.610 ± 0.005 mg used in the second step mentioned in Section 2.4.4 was tested for the take-out-put-back effect.

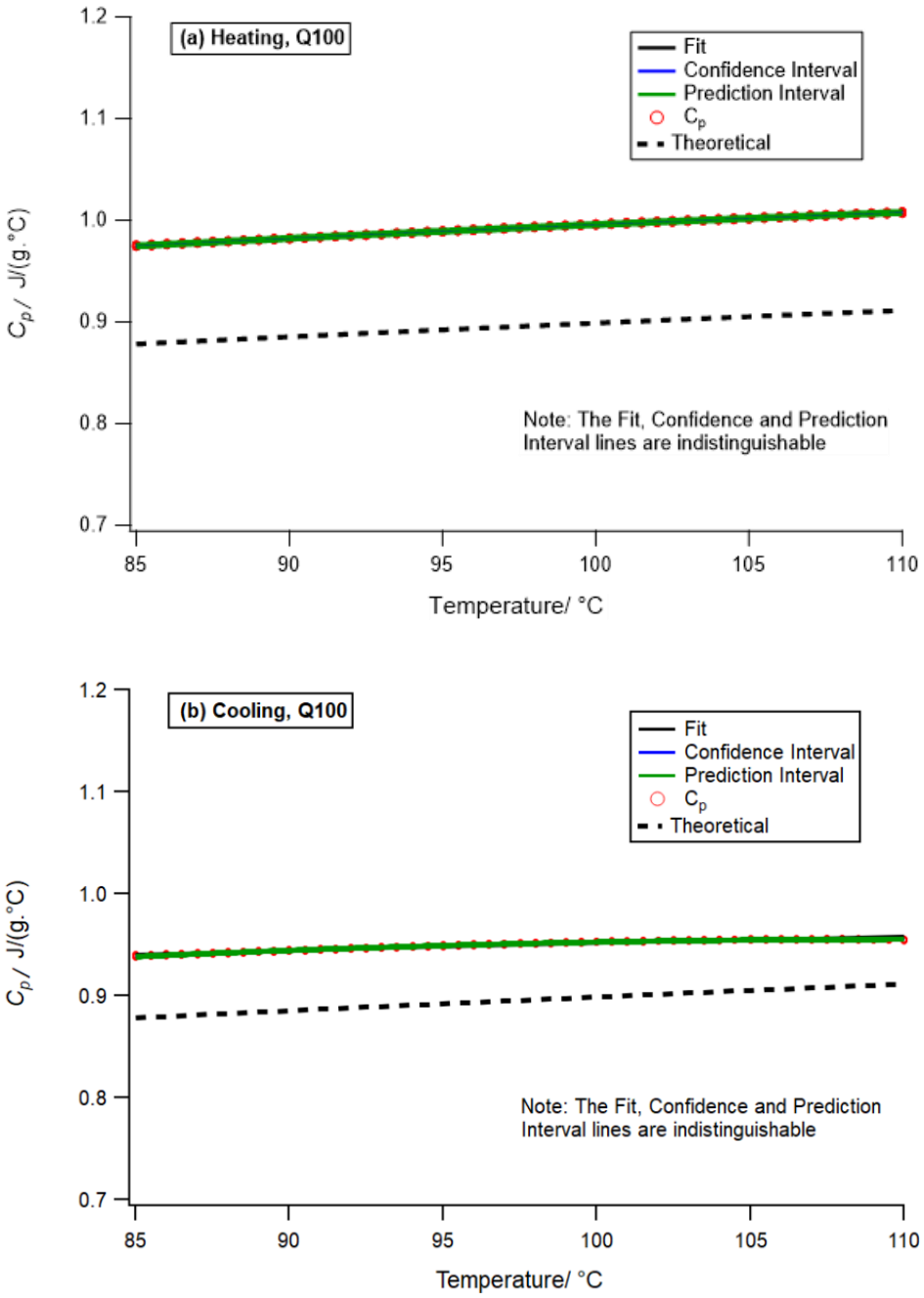

Figure 2-5: C_p (T) values for sapphire during (a) heating and (b) cooling at 15 °C/min using a DSC Q100. Sample mass was 21.610 ± 0.005 mg. (n=10)

The uncertainty of the measurements in the present study were calculated according to the Guide to the Expression of Uncertainty in Measurements (GUM) [81] and shown

in Table 2-2. The systemic uncertainty contributors to C_p measurements such as those from temperature calibration, sample/reference weight measurements, cell constant calculations were not considered in the uncertainty budget, as the current study focuses only on the effect of the pan placement on DSC sensor. Any other factors were kept the same when possible. Their minimum value would be that of the uncertainty of the values determined for the sapphire disc, summarized in Table 2-2.

The standard uncertainty of the C_p measurement $u(y_i)$ is a function of the effect of pan placement added to the common 'minimal background'. The repeatability test was performed when both the reference and sample pans were not moved, and the results are shown in Figure 5. In this context, repeatability is defined as the closeness of the values measured successively under the same conditions. The calculated C_p values during cooling and heating are shown as red dots. A best-fit line as well as the confidence and prediction intervals at 95 % confidence (coverage factor $k = 2$) were computed and plotted.

As depicted in Figure 2-5, the C_p (T) measurements for the sapphire disc showed a relative expanded uncertainty $U(C_p)/ C_p$ value of 0.2 % for both heating and cooling. Their respective relative accuracies, however, were -10.0 and -5.0% with respect to the theoretical values (dashed line). Two other sets of pan placements conditions were also investigated. These conditions included: set#1: the reference pan was kept unmoved, while the sample pan was re-introduced; and set#2: the sample pan was kept unmoved, while the reference pan was re-introduced. The C_p (T) values calculated from set#1 and set#2 are shown in Figure 2-6 and Figure 2-7 respectively.

Wilthan [82] investigated the effect of pan positioning on the sensor for three different DSC instruments; one DSC had a robotic arm, but the others did not, so pans were manually placed. It was found that there was no significant effect of sensor pan position on C_p values among the three DSCs. This was due to the fact that the DSC sensors without the robotic arms are shaped like a "well" with the pans sitting nearly in the same spot, which contributed to the insignificant variation in the C_p values. The DSCs used in this study, on the other hand, have sensors with flat surfaces that allow pans to sit freely anywhere.

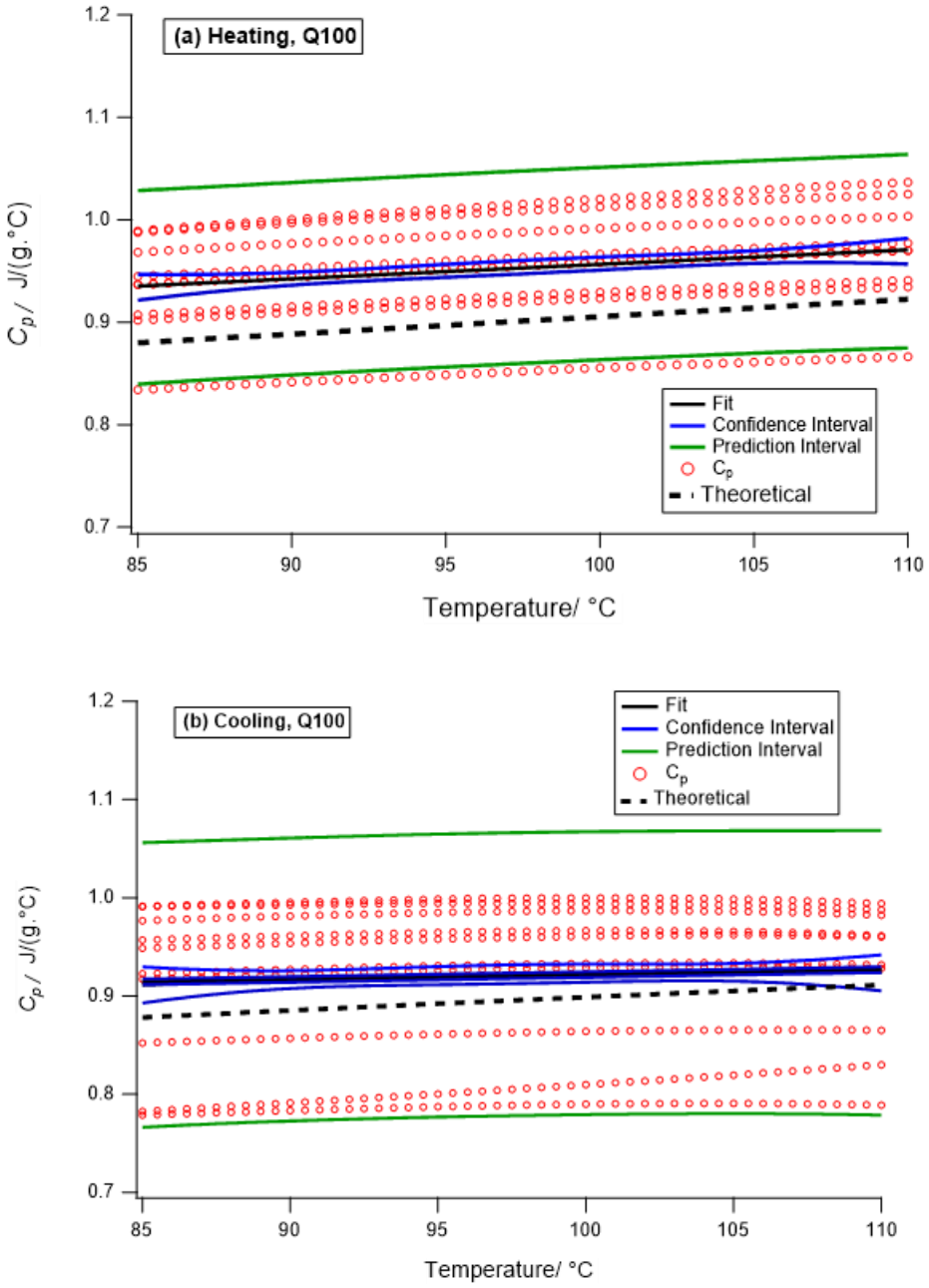

Figure 2-6: C_p (T) values for a sapphire disk during (a) heating and (b) cooling at 15 °C/min using a DSC Q100. Reference pan was kept fixed. The sapphire disk mass was 21.610 mg. (n=10)

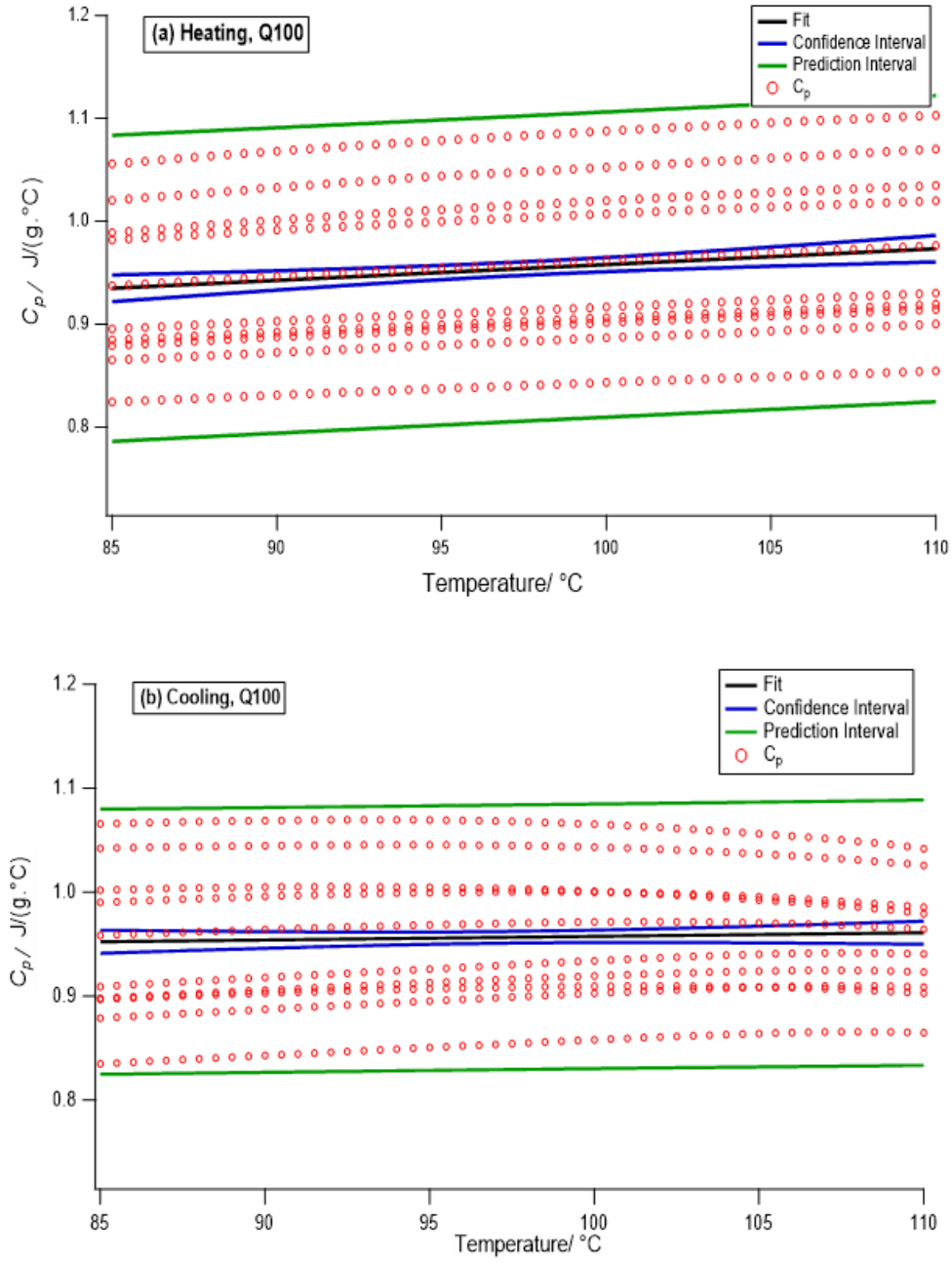

Figure 2-7: C_p (T) values for the sapphire sample during (a) heating and (b) cooling at 15 °C/min using a DSC Q100. Take-out-put-back the reference pan while the sapphire pan is kept fixed. The sapphire disk mass was 21.610 mg. (n=10)

Table 2-2 shows that the sensitivity coefficient from set#1 are larger than those for set#2, and the lease when neither of the pans was moved. This indicates that temperature transient between the sensor and the sample (sapphire disk) is strongly affected by the thermal resistance/conductance path due to the pan on placement on the sensor. In set#2, the reference pan was empty, hence there was less resistance in the heat flow, which resulted in a lower sensitivity coefficient compared to set#1. The DSC used in these sets of experiments (DSC Q100) clearly demonstrated its sensitivity in detecting small changes in the temperature due to variations in the thermal gradient because of pan placement.

The relative accuracy values do not appear to differ much between different pan placement conditions, even when neither of the pans were moved, with values ranging from -2.2 to -9.9%. The lesser relative accuracy values could be explained by the relative excellent thermal conducting characteristics of the sapphire sample, which resulted in a lesser heat resistance and hence much reduced thermal gradient within the sample itself. In addition, the sapphire sample is a disk-shaped crystal with improved contact area between the disk and the pan, and hence much less thermal gradient variability within the sapphire sample. All these factors contributed to the consistent relative accuracy values for the sapphire, though still not accurate.

It is also observed that effect of the direction of the temperature ramp (i.e., heating or cooling) was more pronounced in the set#1 compared to that in set#2. This signifies the entirely different mechanisms of how the DSC controls/measures the temperature heating and cooling. During heating, the sample and the reference pans serve as the “heat sink”, with the heat going from the sensors to the pans. This means that the thermal

conducting characteristics for both the sample and reference pans, including those of the sample itself, shape, and contact area, will have the major influence on the achievable temperature. During cooling however, the opposite scenario is observed. Heat will be conducted from the pans to the sensor, and since the thermal conducting characteristics of the sensors are far better, less uncertainty on the relative precision was achieved. Another important factor in this asymmetry is the heat resistance introduced by heat convection from the nitrogen gas surrounding the pans [83], which will be different between heating and cooling. There are also other contributing factors that should be considered: 1) the flatness of the pans used, 2) the pan orientation, and 3) the anisotropic thermal expansion of sapphire.[84] This anisotropic thermal expansion of sapphire could cause inconsistent expansion of the sapphire disk during heating and cooling cycles. This inconsistent expansion can change the contact area between the sample and the crucible/reference material, leading to variability in heat transfer and, consequently, in the measured heat capacity.

Table 2-2: Uncertainty budget of the specific heat capacity determination of a sapphire disk. Relative accuracy values were calculated with respect to the reference value obtained from reference.[78] All values were evaluated at 95 °C

Pan take-out-put-back		Ramp	$\bar{y}_i$	Probability distribution	Sensitivity coefficient	df (n-1)	Uncertainty contribution, $u_i(y)$	Relative expanded uncertainty, U	Relative accuracy %
Sample pan	Reference pan				J/(g·°C^2)		J/(g·°C)		
Yes	No	Heating	0.932	Normal	0.160	9	0.075	16%	-6%
Yes	No	Cooling	0.921	Normal	0.170	9	0.078	17%	-2%
No	Yes	Heating	0.973	Normal	0.129	9	0.063	13%	-8%
No	Yes	Cooling	0.952	Normal	0.088	9	0.042	9%	-6%
No	No	Heating	0.989	Normal	0.002	9	0.001	0.2%	-10%
No	No	Cooling	0.949	Normal	0.002	9	0.001	0.2%	-5%

2.5.2 MMM sample

The repeatability test for a MMM sample was first evaluated when neither of the pans were moved. The measured C_p (T) values are represented in Figure 2-8 and compared with Morad *et. al.*[58] values (dashed line). The effect of using pan placement conditions set#1 was investigated in two DSC instruments, DSC Q100 and 200, and presented in Figure 2-9 and Figure 2-10 respectively. Set#2 was only investigated in DSC Q100, and the results are presented in Figure 2-11. The uncertainty of the measurements were calculated according to the GUM approach [81] and shown in Table 2-3. It is shown that relative uncertainty U values were in the order of 1.5% during both and heating and cooling, similar to reported values in [71]. However, the same values were 20-30 times larger in the set#1 conditions. This can be understood from the higher thermal resistance of the heat path when MMM was used. U values are comparatively lower in the set#2 placement condition. This observation is expected because the reference pan is empty and therefore there is no heat resistance contribution from the sample and hence the influence on the measured heat flow would be much smaller. Despite the reference pan being empty, the take-out-put-back of the reference pan caused a variability (higher U) in the measured C_p values larger than that from those when neither of the pans were moved (repeatability test). Although the sensor and the pan are made of highly conductive materials, disturbance to the heat transfer characteristics in the sensor-pan interface due to take-out-put-back of the reference pan still strongly influenced C_p measurements.

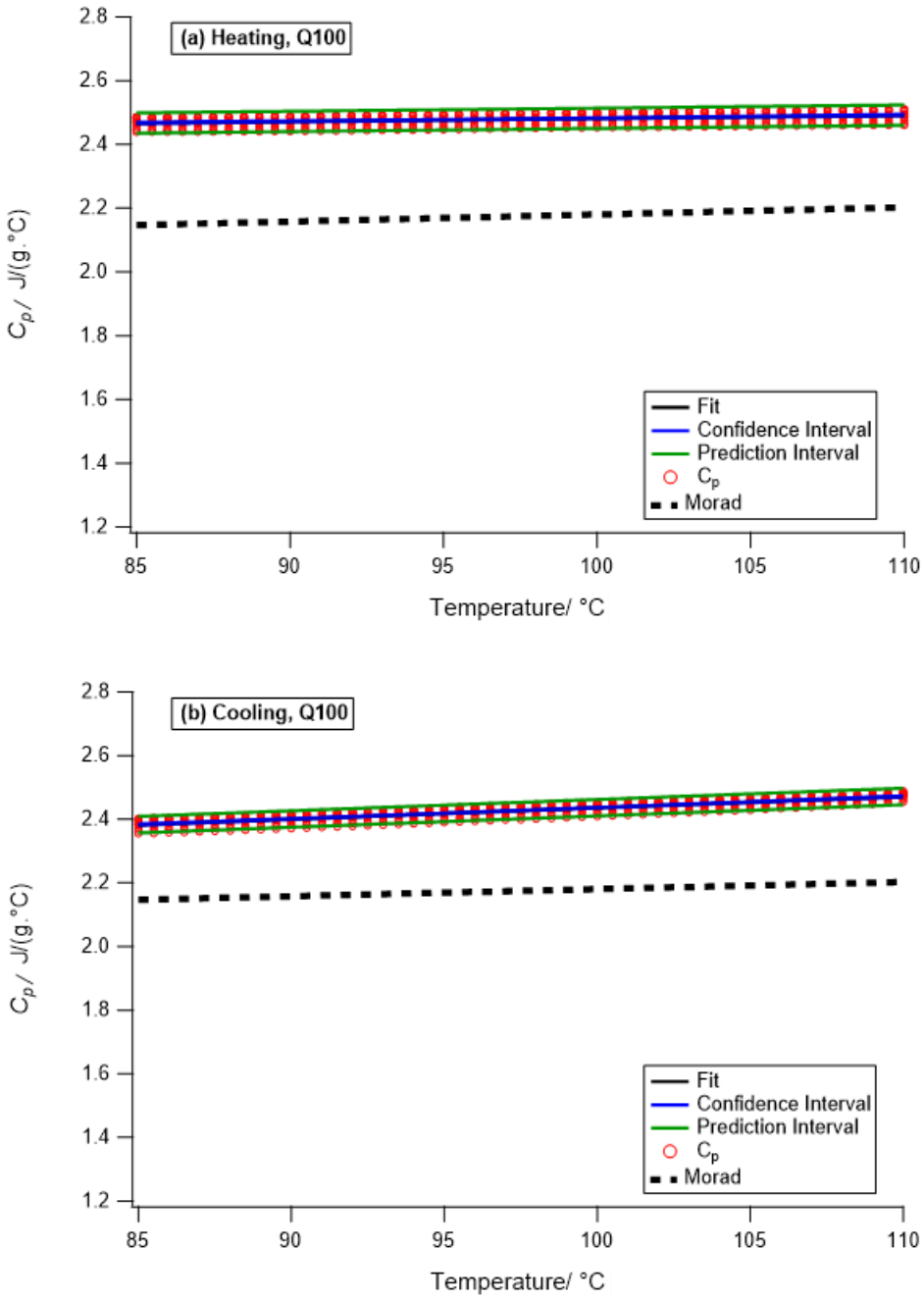

Figure 2-8: C_p (T) values for MMM during (a) heating and (b) cooling at 15 °C/min using a DSC Q100 to test the repeatability of the values. Sample mass was 7.449 ± 0.005 mg. (n=10)

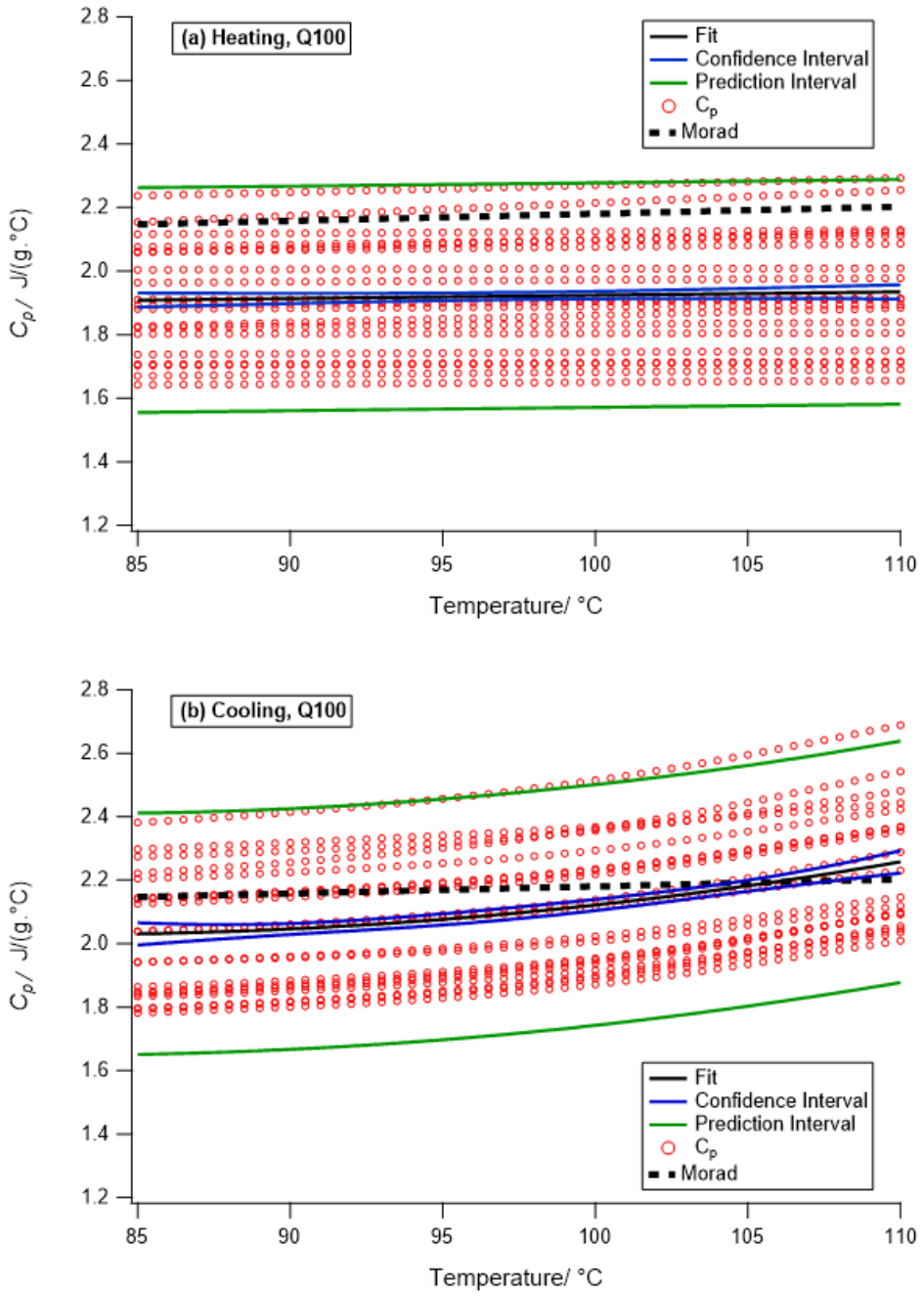

Figure 2-9: C_p (T) values for MMM during (a) heating and (b) cooling at 15 °C/min using a DSC Q100, and values by Morad et. al. [58]Sample mass was 6.049 ±0.005 mg. (n=19)

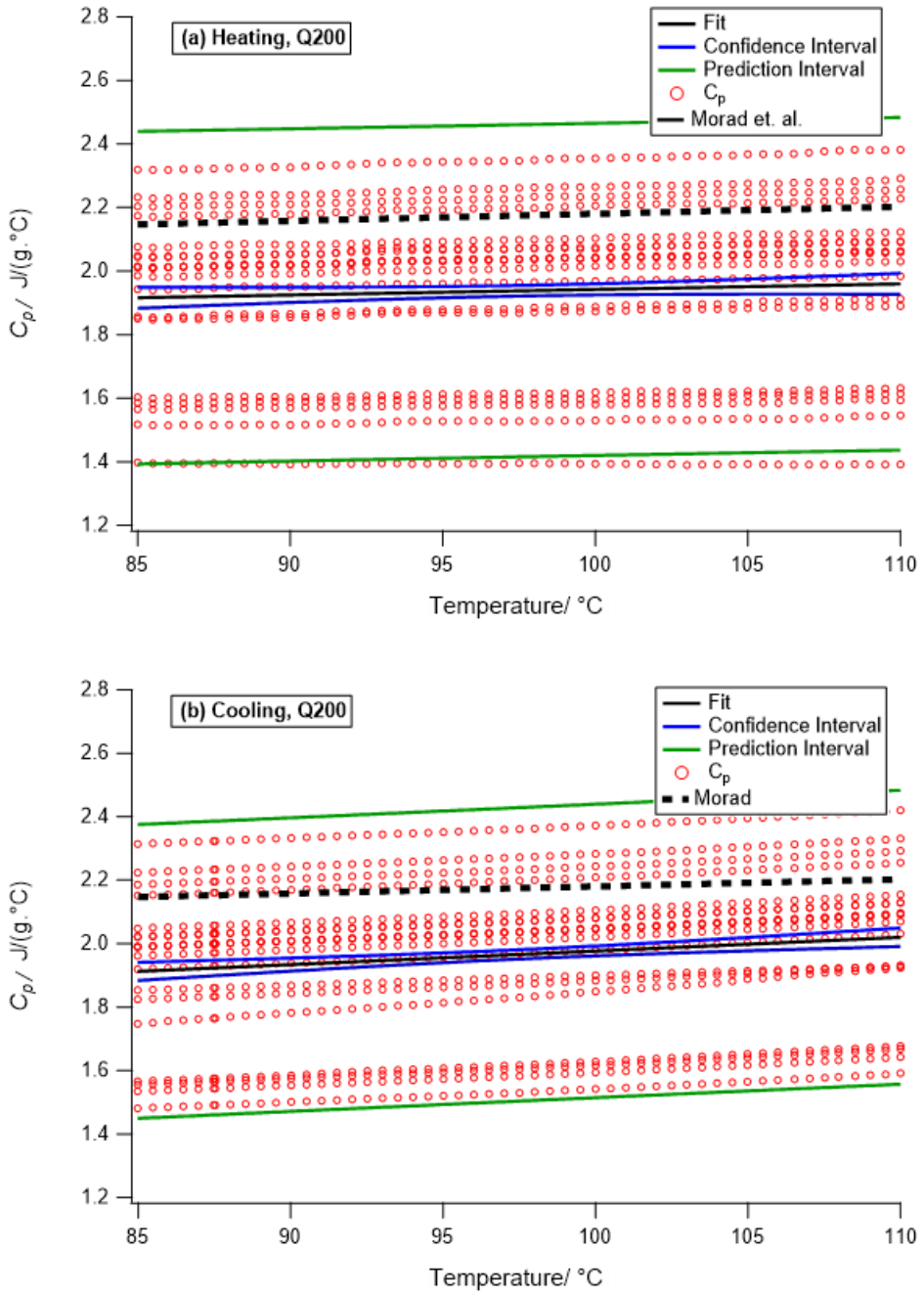

Figure 2-10: C_p (T) values for MMM during (a) heating and (b) cooling at 15 °C/min using a DSC Q200, and values by Morad *et. al* .[58] Sample mass was 7.449 ±0.005 mg. This is the same pan used in DSC Q100 to test for repeatability in Figure 2-6. (n=19)

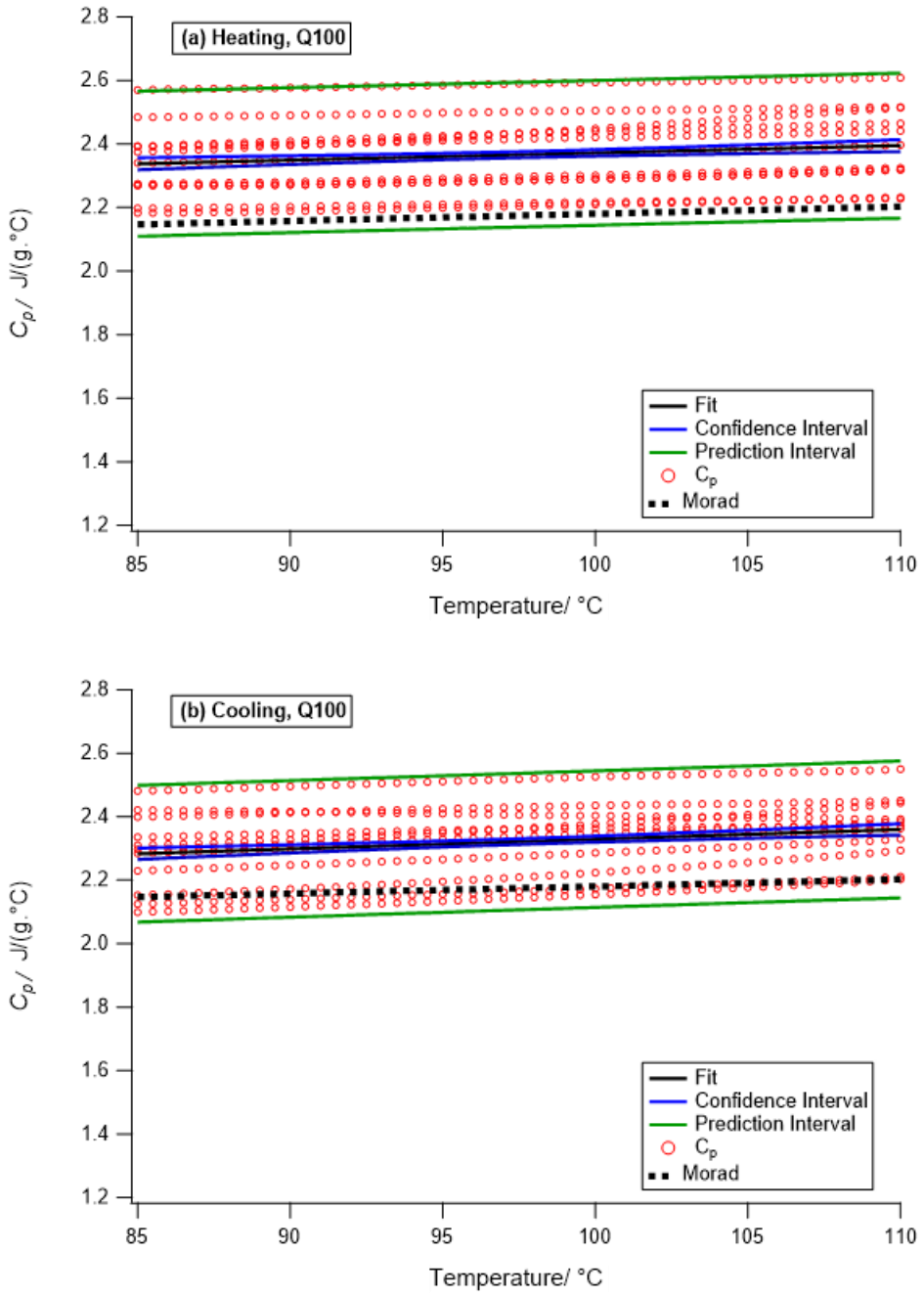

Figure 2-11: C_p (T) values for MMM sample during (a) heating and (b) cooling at 15 °C/min using a DSC Q100. Take-out-put-back the reference pan while the MMM pan is kept fixed. The MMM sample size was 7.449 mg. (n=10)

Table 2-3: Uncertainty budget of the specific heat capacity determination of a MMM sample. Relative accuracy were calculated based on reference values obtained from reference [55]. All values were evaluated at 95 °C.

Pan take-out-put-back		Ramp	$\bar{y}_i$	Probability distribution	Sensitivity coefficient	df (n-1)	Uncertainty contribution, u_i(y)	Relative expanded uncertainty U	Relative accuracy %
Sample pan	Reference pan				J/(g·°C^2)		J/(g·°C)		
Yes	No	Heating	1.845	Normal	0.189	18	0.175	19%	15%
Yes	No	Cooling	1.897	Normal	0.170	18	0.161	17%	13%
Yes	No	Heating*	1.934	Normal	0.288	19	0.279	29%	11%
Yes	No	Cooling*	1.956	Normal	0.252	19	0.246	25%	10%
No	Yes	Heating	2.361	Normal	0.099	9	0.117	10%	-9%
No	Yes	Cooling	2.314	Normal	0.104	9	0.121	10%	-7%
No	No	Heating	2.477	Normal	0.014	9	0.017	1.4%	-14%
No	No	Cooling	2.418	Normal	0.012	9	0.015	1.2%	-11%

*Measurements done with TA Instruments Q200 DSC.

It is also observed from Table 2-3 that the relative uncertainty *U* values were less during cooling compared to those for heating in all experiments. The same observation is also reported for all sapphire experiments but with significantly lower values. The heat flow asymmetry between cooling and heating has been discussed in the literature [74]. Those authors attributed the asymmetry between cooling and heating to the fact that the sample temperature deviates from the set point temperature differently on cooling and heating; however, this deviation should be small in practice according to the same authors. This is true if one only considers that all heat resistances due to conduction are the same between heating and cooling, however heat resistance introduced by the convective heat transfer in the surrounding could be a major contribution to this asymmetry. [85]

During calibration, the resistances and capacitances values used in the Tzero™ algorithm, to account for the heat flow imbalance between the two posts, are only obtained during heating. Although there is a cooling/heating calibration feature available in the calibration package, it is not, in fact, active. This 'cooling' step is meant to be a preconditioning scan to optimize the heat flow signal by reducing the "first run effect". TA instruments DSCs do not use different values of capacitances and resistances for cooling in the T4 heat flow algorithm, although it is reasonable to believe that there should be ones. A temperature calibration method has been proposed to calibrate the old 2920 TA instruments DSCs during cooling [86]. However, according to TA instruments (personal communication), the heating-cooling asymmetry, as well as the effect of different temperature ramps on the heat flow signals, were already addressed in the newly improved Tzero™ furnaces compared to the older 2920 DSCs.

Another possible contributing factor to the observed uncertainty in C_p measurements is the configuration of the sample inside the pan. The sapphire sample is a disk, and its shape does not change with temperature and consequently more evenly distributed heat across the sample. In the case of the MMM sample, however, we observed that the interfacial energy of the liquid MMM sample makes it adopt a concave up configuration, with more sample material on the edges of the pan and less sample at the center of the pan. Upon solidification and melting, the precise shape of that meniscus can change, giving rise to different heat resistances across the sample in the pan. Therefore, the liquid MMM will be more susceptible to changes in heat flow signals when the sample is taken-out-put-back. The heat resistance between the sample and the pan is usually difficult to predict and can change drastically during measurements, as pointed out by Merzlyakov and Schick.[73]

2.5.3 Thermal diffusivity effect and pan position.

To better explain these observations, the heat transfer characteristic of both MMM and sapphire need to be discussed. Table 2-4 shows the literature values of C_p, density, ρ, and thermal conductivity, κ, for both samples. These characteristics were estimated at 95 °C, the C_p value for MMM was extrapolated following the C_p (T) reported by Morad [55]. The thermal diffusivity, α, is calculated by $\kappa/(\rho \cdot C_p)$.

Table 2-4: Characteristic values of thermal properties for MMM and sapphire at 95 °C.

	C_p J/(kg·°C)	κ W/(m·°C)	ρ kg/m^3	α m^2/s
MMM	2150 [55]	0.23 [87, 88]	862 [89]	1.2 x 10^{-7}
Sapphire	899 [78]	24.3 [90]	3970 [90]	9.8 x 10^{-6}

Thermal diffusivity is a measure of how easy/fast a sample can transfer heat across its bulk to attain a homogeneous temperature distribution. The calculated thermal diffusivity value for MMM is about 80 times smaller than that for the sapphire. The relatively high thermal diffusivity of the sapphire sample explains why C_p measurements have lower U values compared to that for MMM in all experiments. High thermal diffusivity value produces lower thermal lags across the sample. The thermal lag experienced by the sapphire disk is much smaller compared to MMM, which resulted in low and similar variability in C_p measurements during heating and cooling in all experiments. It is also observed that the uncertainty was found to be less during cooling versus heating for both MMM and sapphire samples.

2.5.4 FEM simulation of heating and cooling MMM in a DSC pan

The thermal lag expected from the liquid MMM was estimated using the MATLAB partial differential equation (PDE) Toolbox. It uses a finite element method (FEM) to solve two-dimensional partial differential equations. The conduction heat-transfer in the MMM was described by a parabolic equation in radial coordinates. The dependence of thermal diffusivity on temperature was approximated as indicated in Table 2-5. During cooling, gravitational forces due to density gradients are balanced because denser layers are

always below lighter layers. During heating the forces are not balanced, and given enough time, a convection circulatory pattern would be established. The pattern would appear counter clockwise in Figure 2-12.

However, due to the short duration of the heating ramp, it is unlikely that this pattern will be fully developed before the bottom of the pan reaches the higher temperature. After the isothermal wait time at high temperature, the temperature in the liquid becomes uniform and constant, and the density gradients disappear. This condition of more homogeneous temperature that preceded the cooling ramp could explain the less variability in the heat capacity values.

The pan is represented as an axisymmetric truncated cone in cylindrical coordinates (r,z). The axis of symmetry (rotation) is the z axis, antiparallel to gravity (arrow). The volume of the sample is 8.63 µl at 80 °C, which corresponds to 7.449 mg. The horizontal dashed line indicates the surface of the liquid in the absence of interfacial tension. The curved lines represent the surface at 60 °C and 120 °C. The angle at the contact point is highlighted by the projections of its tangent line. At 60 °C the contact angle θ_c is 15.2°, whereas at 120 °C the angle is 11.5°.

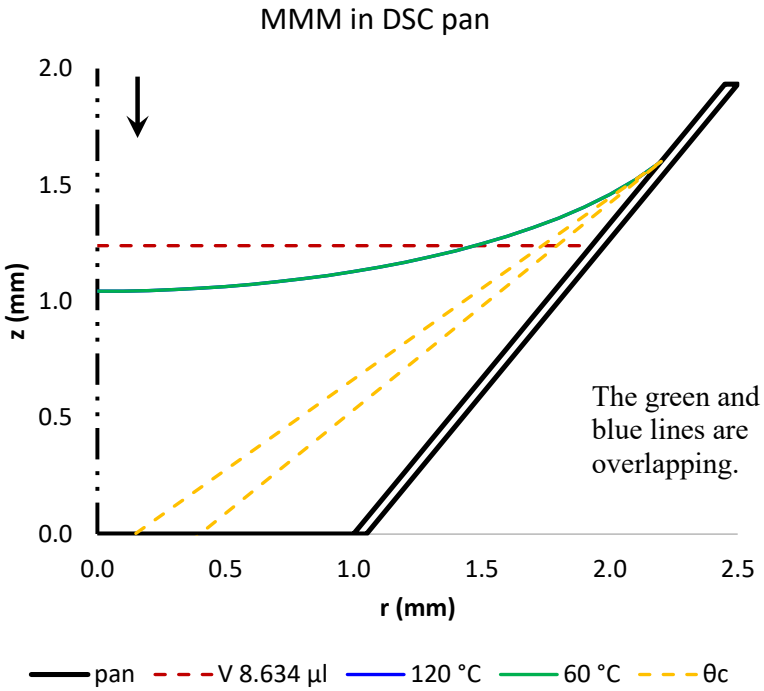

Figure 2-12: FEM simulation of MMM sample in aluminum pan.

Table 2-5: Properties of the materials used in FEM simulation.

Property	Units	Liquid MMM (T in °C)	Aluminum
Thermal diffusivity, α	mm^2/s	$0.107 + 1.8\times10^{-4}\cdot T$ [91]	91 [92]
Density, ρ	kg/mm^3	$(917.362 - 0.683\cdot T)\times10^{-9}$ [93]	2698×10^{-9} [92]
Specific heat capacity, C_p	$J/(kg\cdot°C)$	$(2.0 - 0.002\cdot T)\times10^{3}$ [55]	921 [92]
Thermal conductivity, κ	$W/(mm\cdot°C)$	$(0.20 - 0.85\times10^{-4}\cdot T)\times10^{-3}$ [91]	226×10^{-3} [92]
Surface tension, σ	N/m	$(32.69 - 0.0625\cdot T)\times10^{-3}$ [94]	--
Mass	mg	7.449	
Thickness	mm		0.036

Surface tension estimated using data for PPP and ClClCl in reference [94]

The ellipsoid of revolution approximately describing the surface is defined by three parameters: the centre on the z axis, z_h, the semiaxis in the r direction "a", and the semiaxis in the z direction "b". The volume of liquid and contact angle were used to approximate the liquid surface as an ellipsoid of revolution at 60 °C and 120 °C. The surface at both temperatures has been plotted in Figure 12, along with the level that the sample would have in the absence of surface tension (red dashed line). The two ellipsoidal surfaces are

barely distinguishable (green and blue). For the simulation of the 7.449 mg sample, r_c = 2.201, z_h = 1.971, A = 2.40, and B = 0.9284. From FEM it was possible to simulate the temperature distribution of the MMM sample in the DSC pan at the end of cooling and heating, as depicted in Figure 2-13.

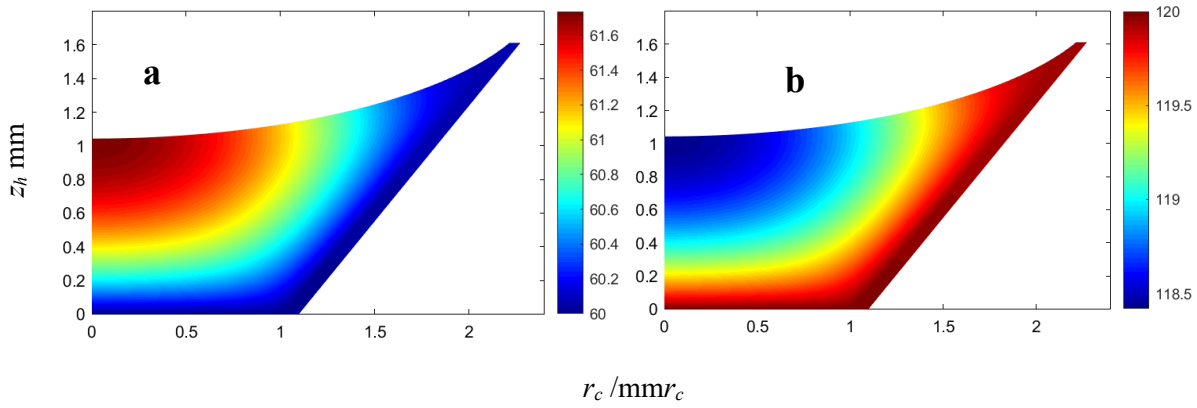

Figure 2-13: FEM Simulation: (a) end of cooling and (b) end of heating of 7.449 mg of MMM in DSC pan.

Given the information from Figure 2-13, the temperature lag values were computed during heating and cooling and illustrated in Figure 2-14. At the highest expected temperature difference across the sample, *i.e.* bottom of the pan and the warmest and coldest spot during cooling and heating respectively, the temperature difference (thermal lag) did not exceed 1.5 °C. It was also observed that the temperature difference in the bottom of the pan during cooling and heating ranged between 1.26 and 1.8 °C at 65 and 115 °C, respectively (Figure 2-14 "b"). The data from Figure 2-13 and Figure 2-14 indicate that these temperature differences do not explain the variability in the measured heat capacities. To verify this, the difference in heat capacities between heating and cooling was calculated and plotted as a function of temperature in Figure 2-15 for a run using DSCQ200. As demonstrated in the same figure, the difference in heat capacities was less than 1% between cooling and heating. Hence the low thermal diffusivity effect of MMM does not

explain the observed uncertainty in heat capacities. It is very likely that the temperature distribution across the DSC sensors were not homogeneous, leading to either under- or over-estimated heat flow to the sample and reference pans. The temperature inhomogeneity in calorimetry was reported in the literature. [95]

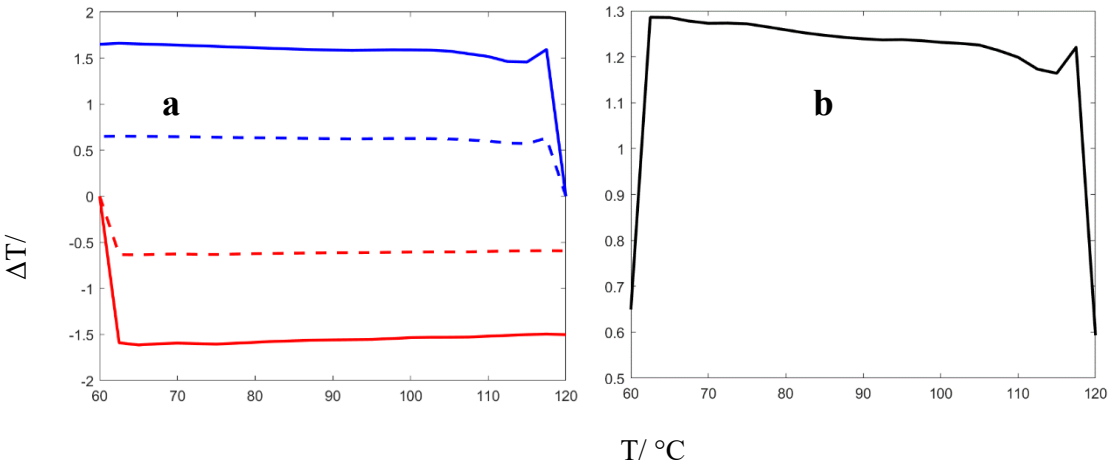

Figure 2-14: (a) Temperature difference between bottom of the pan and: (- red) coldest spot during heating, (-- red) average temperature; (- blue) warmest spot during cooling, (-- blue) average temperature; (b) Difference between cooling and heating average.

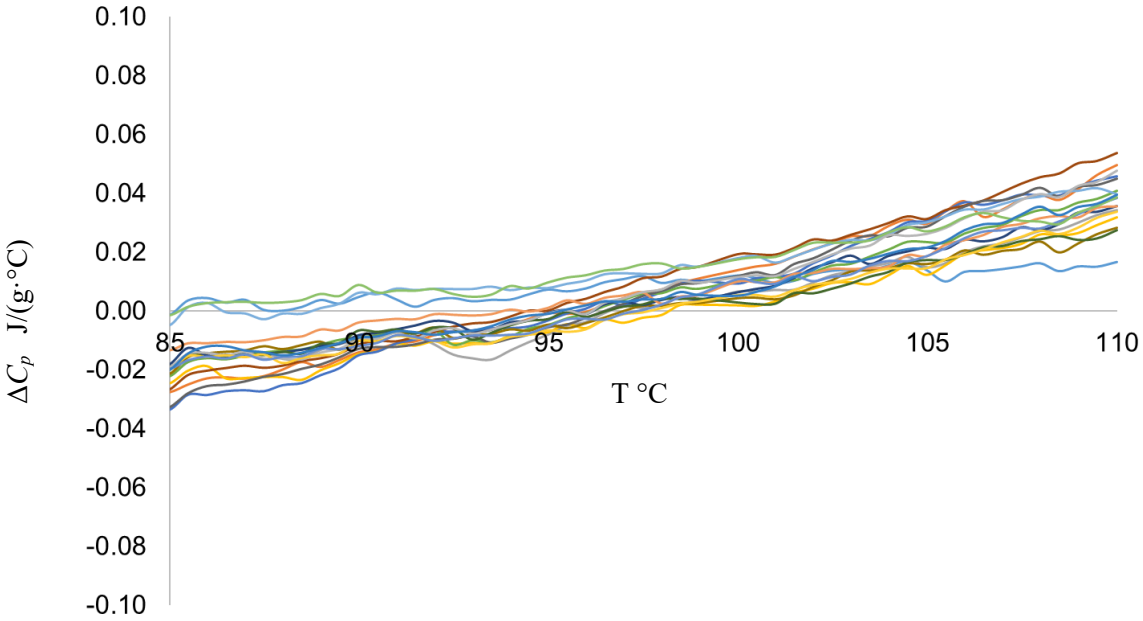

Figure 2-15: ΔC_p=cooling-heating values as function of temperature obtained from the same run using DSC Q200.

2.6 CONCLUSIONS

This paper has shown that the pan placement on the DSC sensor has a significant effect on the calculated uncertainty of the C_p measurements. This effect was found to be much higher for MMM sample compared to that of the sapphire disk, with relative uncertainty U values 10-25% for MMM and 9-16% for the sapphire disk. These values are much higher than what is commonly reported in the literature (1-5%). The differences in thermal conductivity and shape/configuration of both samples significantly influenced the uncertainty in the C_p values. As shown with FEM simulations, the effect of thermal diffusivity did not, however, explain the large uncertainty in the heat capacity measurements. It is likely that the temperature distribution across the sensor (sample or reference positions) is not homogeneous leading to different heat flow experienced by the pans, which

resulted in different heat capacity measurements. This study calls DSC users who seek to find accurate C_p values to pay attention to this effect. The effect of the position of the pan on the final heat flow is inescapable because normally a DSC user needs to use multiple pans (replicas) to test for the statistical significance of their observations.

2.7 ACKNOWLEDGMENTS

We acknowledge the support of NSERC, CFI, the Atlantic Innovation Fund, and other contributors which funded the Facilities for Materials Characterization, that were managed by the Institute for Research in Materials at Dalhousie University.

CHAPTER 3 PREDICTION OF THE ONSET NUCLEATION TEMPERATURES OF METASTABLE POLYMORPHS – PART 1 – β' POLYMORPH OF TRIDODECANOYL-GLYCEROL (TRI-LAURIN)

3.1 PUBLICATION INFORMATION

This chapter is a modified version of a manuscript that will be submitted as:

Omar Al-Qatami, Xinyue Zhang, Gianfranco Mazzanti (2023). Prediction of the onset nucleation temperatures of metastable polymorphs – Part 1 – β' polymorph of tridodecanoyl-glycerol (trilaurin). Journal of the American chemical society (JACS). (In preparation).

3.2 ABSTRACT

Perhaps surprisingly, there is no quantitative answer to the seemingly simple question: what is the crystallization temperature of a liquid triacylglycerol (TAG) cooled from the melt at a given cooling rate? And what polymorph will it form? We address the first question using the differential form of the homogeneous nucleation theory of Turnbull and Fisher T&F to calculate the nucleation onset temperatures of a TAG, tridodecanoyl-glycerol (LLL, CAS 538-24-9) cooled from the melt. At the cooling rates explored (2.5 to 15 K/min), the nucleation produces the β′ polymorph, at temperatures that are lower as the cooling rate is faster. The experimental crystallization onset temperatures were obtained from DSC thermograms. The polymorphic forms at the onset temperature were identified using time-resolved SAXD and WAXD data from experiments at a

synchrotron. For this model we introduce a nanoplatelet embryo geometry, an interfacial energy dependent on temperature, and an activation energy barrier that depends on temperature and number of molecules of the embryos. In most works on this topic the geometry is considered spherical, and the interfacial energy and activation energy are considered constant. The interfacial energy was approximated as $\delta = [0.8351 + 0.7506 \cdot (T_m - T)] \times 10^{-24}$ kJ/nm^2. The partial differential equation was adapted to be solved numerically with MATLAB, making this model accessible to many researchers. These four contributions open the possibility to predict onset temperatures for custom time-temperature profiles. This will allow pharmaceutics, cosmetics, nutrition, and many other industrial users to improve their materials' design capability.

3.3 INTRODUCTION

There is a large body of literature on the crystallization and nucleation of triacylglycerols (TAGs) under quasi-isothermal cooling conditions.[96, 97] However, in commercial situations, the temperature changes with time, which is generally referred to as a cooling rate. The processes of crystallization and nucleation under non-isothermal cooling settings are crucial to industry and necessitate specialized models for characterization. [17]

The processes of nucleation and growth underlie many phase transformations. Clusters of atoms with the configuration of the transformation product are postulated to form the starting material, according to the CNT of Turnbull and Fisher T&F. [98-100] Due to their high surface-to-volume ratio, the initial clusters are small and unstable. However, some clusters eventually reach a size beyond which they are stable and transform into nuclei. The rate at which nuclei are created is held constant if the temperature is kept

constant.

In computational chemistry, the accurate and reliable prediction of nucleation rates and pathways remains a challenging obstacle and far from complete. [101] T&F provides a simple thermodynamic framework for calculating the nucleation rate based on the reversible nucleation work required to form a droplet of the thermodynamically stable phase surrounded by the metastable phase. However, the standard CNT is based on two critical assumptions: (i) it uses bulk values for the pressure difference between the two phases, and (ii) the interfacial energy equals the bulk value of a flat interface (≈1). [102] In practice, interfacial energy is frequently treated as a free fit parameter, producing values that may deviate significantly from the corresponding bulk values.

There have been many attempts to describe and model the process of nucleation and the kinetics of fat crystallization in the research that has been done so far. However, it is crucial to acknowledge that these attempts have been impeded by inherent limitations associated with the applied methods, theories and/or assumptions. For example, some researchers believe that the induction time of nucleation, t_{ind}, represents the nucleation rate predominately. Although this method is widely used to explain nucleation kinetics in fat systems[103-107], the induction time is a distinct physical event from nucleation.[17]

In this work we treat the nuclei as monolayer nanoplatelets, in keeping with recent findings. [18] We also introduce a temperature dependent interfacial energy and propose an 'a priori' interpretation of the energy barrier based on the entropy of the activated state. These generalizations are very important for all materials with molecules of a significant aspect ratio, as they form nano-nuclei that are far from spherical.

3.4 NUCLEATION MODEL

The partial differential equation from T&F [5] for the rate of formation of the number of embryos per unit volume, n_i, having "i" molecules is:

$$\frac{\partial n_i}{\partial t} = \left(\frac{-i_s k_b T}{h}\right)\left[n_i\left(\frac{2}{3}A \cdot i^{-\frac{1}{3}} - B\right) + \frac{\partial n_i}{\partial i}\right] \cdot i^{\frac{2}{3}} \cdot exp\left(\frac{-\Delta f^x}{k_b T}\right) \qquad 3\text{-}1$$

where k_b and h are Boltzmann's and Planck's constants, respectively; T is the temperature in K; A and B are both functions of the interfacial and volume energies; Δf^x is the Gibbs activation energy barrier, with respect to average energy between an embryo of "i" molecules and one of "$i+1$" molecules, at a given temperature; $\frac{\partial n_i}{\partial t}$ is the rate of number increase of each class of embryos; and $\frac{\partial n_i}{\partial i}$ is the gradient of the number of embryos of each class with respect to the number of molecules in the embryos. The "i_s" in the first term is the number of molecules at the growing interfaces of the nano-embryo.

The terms of Equation 3-1 depend on the material properties of the liquid and the crystalline solid, *e.g.*, equilibrium melting temperature, enthalpy, specific heat, interfacial energy, and crystallographic dimensions. These properties are a function of temperature.

For pure TAGs, there are three main monotropic polymorphic crystalline forms, α, β', and β in an increasing thermal stability order, often with sub-varieties. [107] In this paper we look at the metastable form β' of tridodecanoyl-glycerol (trilaurin LLL), with a melting point of 308.3 K. The undercooling driving forces of nucleation will only act after crossing the melting temperatures of the more thermally stable polymorphs, β' and β. We focus on nucleation at a constant cooling rate at temperatures higher than the melting point of the metastable form α, 288.7 K. Most literature investigating crystallization of

TAGs explores their mixtures for practical applications. [108, 109] To estimate the energy barrier they use the isothermal version of T&F [110], in which the surface energy is constant with temperature; the nucleus is assumed to be spherical in shape; and the induction time is considered independent of the number of embryos per unit volume. They also use the Hoffman-Weeks [111] extrapolation for the estimate of the reference melting temperature. [103] Of special interest for this work is the recent work to determine the isothermal nucleation rates at different temperatures using the T&F approach. [112] Before the T&F model can be applied to mixed systems, it is necessary to apply it to simple, monoacid, pure TAGs.

In the next three subsections we discuss the terms that form Equation 3-1, providing a detailed explanation of their derivation. The fourth subsection explains the numerical strategy used to compute solutions of this equation to estimate the interfacial energy parameters.

3.4.1 Geometrical properties of the nanoplatelet embryos

The properties of two polymorphs, β'and β, are summarized in Table 3-1. The specific heat of the liquid is independent of the polymorphic forms. The specific heat of the crystals is a second order polynomial. The coefficients in the table are for temperatures in K.

Table 3-1:Properties of tridodecanoyl-glycerol (trilaurin)

	Polymorphic Form		
	β'	β	Ref.
T_m, K	308.3	318.9	[113]
ΔH_m, kJ/mol	86.0	122.2	[114]
v_s, nm^3/molecule	1.103	1.015	[115]
C_{p0}, kJ/(K·mol)	3.46	2.79	[116]
C_{p1}, kJ/(K^2·mol)	-2.26×10^{-2}	-1.68×10^{-2}	[116]
C_{p2}, kJ/(K^3·mol)	5.68×10^{-5}	4.30×10^{-5}	[116]
r_a	2.1	2.4	[18]
d_0, nm, $\xi_0=1/d_0$	3.25	3.12	[113]
m_0, molecules/nm	0.3077	0.3205	
m_1, molecules/nm	1.672	1.556	
m_2, molecules/nm	1.762	1.835	
C_{pLiq}, kJ/(K·mol)	$1.222 + 2.443\times10^{-3}\cdot T$		[43]

The embryos are assumed to be a monolayer nanoplatelet made of pairs of molecules in complementary vertical arrangement side by side, known as 2L (Figure 3-1). [107] Thus $\xi_0 = d_0$. The aspect ratio of the single layer embryo or nucleus is $r_a = \xi_2/\xi_1$. The surface area and the volume of the platelet, as a function of the second dimension $\xi = \xi_1$, are in Equation 3-2.

$$A_p = 2 \cdot (d_0 + r_a \cdot \xi + d_0 \cdot r_a) \cdot \xi; V_p = d_0 \cdot r_a \cdot \xi^2 \qquad 3\text{-}2$$

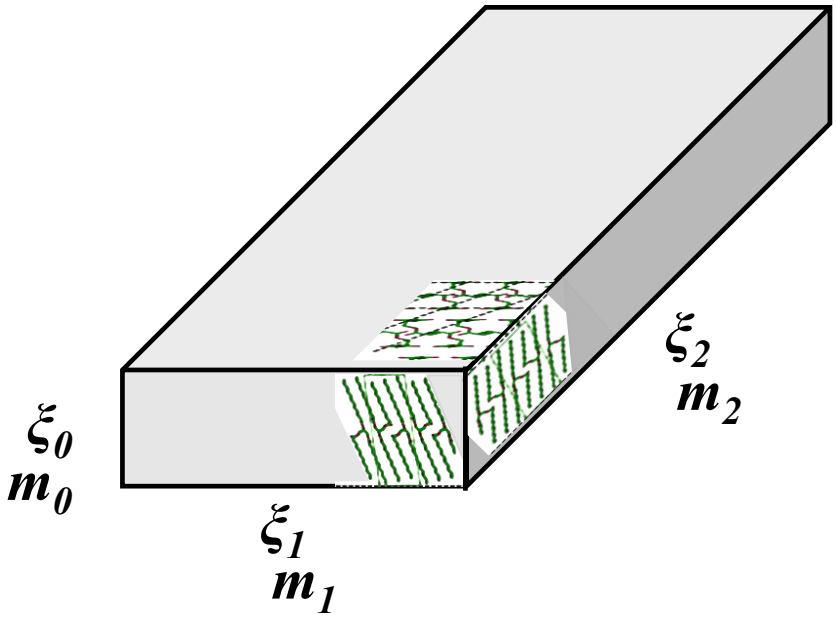

Figure 3-1:Idealized representation of nanoplatelet sizes (ξ0, ξ1, ξ2) and molecules/nm (m_0, m_1, m_2). ξ0 is in the direction of the crystallographic b axis in [117] [18]

Each polymorph has its own aspect ratio. Common values of r_a are around to be around 2.4 for the β polymorph. The values for the other polymorphs have been estimated from crystallographic information. [115] The molar volume of each molecule in an embryo is v_s, in nm^3/molecule. The number of molecules "*i*" in a platelet is, therefore:

$$i = \frac{d_0 \cdot r_a \cdot \xi^2}{v_s} \qquad 3\text{-}3$$

The number of molecules per unit length (molecules/nm) on each side of the platelets are m_0, m_1, and m_2, so that:

$$i = m_1 m_2 \cdot r_a \cdot \xi^2 \qquad 3\text{-}4$$

These values must satisfy the specific volume of a molecule, v_s, by the relationship:

$$\frac{1}{m_0 m_1 m_2} = v_s \qquad 3\text{-}5$$

The "i_s" in the first term of the T&F equation (Equation 3-1) depend on the area/volume ratio of the shape of the embryos, assumed here as monolayer the nanoplatelet crystals. The ratios and molecules per side depend on the polymorph, estimated from the crystallographic information. [115] The platelet thickness ξ in nm is known from X-ray diffraction for the crystals and will be used here as an estimate for the embryos. For a single lamella embryo, $m_0 = 1/d_0$. Thus,

$$i_s = 2 \cdot (m_1 + r_a \cdot m_2) \cdot \xi \qquad 3\text{-}6$$

To put it as a function of the number of molecules in the embryo's platelet:

$$i_s = 2 \cdot (m_1 + r_a \cdot m_2) \cdot (k_0)^{\frac{1}{2}} \cdot i^{\frac{1}{2}} \qquad 3\text{-}7$$

With a convenience constant k_0:

$$k_0 = \frac{v_s}{d_0 \cdot r_a} \qquad 3\text{-}8$$

3.4.2 Gibbs energy and interfacial energy temperature dependency

The Gibbs energy difference at a temperature depends on the properties of the liquid and the solid for a given polymorph. The interfacial energy is δ, and the difference in chemical potential between the phases is $\Delta\mu$. For a pure material $\Delta\mu = \Delta G_{melting} = -\Delta G_{crystallization}$, which we call ΔG_s. ΔF is the Gibbs energy in the context of the "Gibbs-Thomson" equation.[118] Unless otherwise stated, the following equations were developed by the author in collaboration with the research team (Dr. Gianfranco Mazzanti and Xinyue Zhang) for the monolayer nano-platelets.

$$\Delta F = 2 \cdot d_0(1 + r_a) \cdot \xi \cdot \delta - d_0 \cdot r_a \cdot \xi^2 \cdot \frac{\Delta G_s}{v_s} \tag{3-9}$$

thus,

$$\Delta F = d_0(1 + r_a) \cdot (k_0)^{\frac{1}{2}} \cdot 2\delta \cdot i^{\frac{1}{2}} - \Delta G_s \cdot i \tag{3-10}$$

Examples of ΔF at different temperatures are given in the results section, in Figure 3-9(A). At the critical size ξ_c the derivative of the energy is zero, *i.e.*, $\frac{d\Delta F}{di} = 0$. The critical number of molecules i^*, and the critical size ξ_c are:

$$i^* = \left[\frac{d_0(1 + r_a) \cdot \delta}{\Delta G_s}\right]^2 \cdot k_0 \tag{3-11}$$

$$\xi_c = (i^* \cdot k_0)^{\frac{1}{2}} \tag{3-12}$$

The critical size ξ_c depends on the polymorph, with $\xi_{c\alpha} > \xi_{c\beta'} > \xi_{c\beta}$. The dependency of critical size on temperature is illustrated later in the paper in Figure 3-9 (B). The energy at the critical size is:

$$\Delta F^* = d_0(1 + r_a) \cdot (k_0)^{\frac{1}{2}} \cdot 2\delta \cdot i^{*\frac{1}{2}} - \Delta G_s \cdot i^* \tag{3-13}$$

At the melting temperature ΔG_s is zero, and the size is infinite.

As explained in T&F, the free energy of an embryo of "*i*" molecules, ΔF_i, (see Figure 3-8) is often parametrized as

$$\frac{\Delta F_i}{kT} = A \cdot i^{\frac{2}{3}} - B \cdot i \qquad 3\text{-}14$$

The coefficients *A* and *B* depend on the Gibbs energy for the critical nucleus with number of molecules *i** ("Gibbs-Thomson" equation) following T&F. The units of *A* are molecules $^{(-2/3)}$ and the units of *B* are molecules^{-1}.

At the maximum, where $i = i^*$, the derivative $d\Delta F/di$ must be zero. Hence

$$\frac{\Delta F^*}{kT} = \frac{\left(\frac{A}{3}\right)^3}{\left(\frac{B}{2}\right)^2} \; ; \; i^* = \left(\frac{2}{3}\frac{A}{B}\right)^3 \qquad 3\text{-}15$$

The coefficients *A* and *B* in T&F are therefore:

$$A = 3 \cdot \frac{\xi_c \cdot (d_0 + (\xi_c + d_0) \cdot r_a) \cdot 2 \cdot \delta - \xi_c^2 \cdot \frac{\Delta G_s}{k_0}}{kT(i^*)^{\frac{2}{3}}} \qquad 3\text{-}16$$

and for *B*

$$B = \frac{2}{3}\frac{A}{(i^*)^{\frac{1}{3}}} \qquad 3\text{-}17$$

Since $A>0$, from its denominator we have the important relationship:

$$\delta > \frac{d_0}{2 \cdot v_s} \cdot \Delta G_s \qquad 3\text{-}18$$

for β' the value of $d_0/(2.v_s)$ is 1.474 molecules/nm^2.

The Gibbs energy of crystallization at deep undercooling temperature *T* for the bulk material is:

$$\Delta G_s = \frac{-1}{N_A} \cdot \left[-\Delta H_m \left(1 - \frac{T}{T_m}\right) + \int_{T_m}^{T} \Delta C_p dT - T \cdot \int_{T_m}^{T} \frac{\Delta C_p}{T} dT \right] \qquad 3\text{-}19$$

where:

$$\Delta C_p = C_p^s - C_p^l \tag{3-20}$$

The chemical potential ΔG_s is close to linear for ΔT<30, as seen later in Figure 3-8. The slope is k_{Gs}, thus:

$$\Delta G_s \approx k_{G_s} \cdot \Delta T \tag{3-21}$$

The value of k_{Gs} is 4.593×10^{-25} kJ/(molecule·K). ΔG_s is between 7.5 and 9 $\times10^{-24}$ kJ/molecule for ΔT 13 to 20 (295 to 288 K). Thus, the interfacial energy δ must be larger than 11 to 14 $\times10^{-24}$ kJ/nm^2. The interfacial energy δ cannot be just a fixed multiplier of ΔG_s because then values of i^* would not decrease with ΔT in Equation 3-11. However, $\delta/\ \Delta G_s$ must decrease with ΔT. Therefore, at ΔT=0 the value of δ cannot be zero. This makes sense, since it is the interfacial energy of the ideal large crystal at its melting temperature, δ_m.

Laird[27] following Baidakov[28], presents an expression that we adapt here for our interface area and notation as:

$$\frac{d\left(\delta/_T\right)}{dT} = -\frac{e}{T^2} + \frac{\tau}{A_p T}\frac{dA_p}{dT} \tag{3-22}$$

where e is the excess interface energy and τ is the excess interface stress. In our embryo nanoplatelet we are implicitly assuming that the number density is constant, since the specific volume of each molecule is taken as a constant. We have no way at present to quantify the very small density changes in the embryo density due to temperature. Hence the derivative of the area with respect to temperature is zero. For convenience we estimate e as:

$$e = \delta_m + \delta_T \cdot T_m \tag{3-23}$$

where δ_m is the interfacial energy at the melting temperature and δ_T is the increase of interfacial energy per unit temperature of undercooling. This yields from Equation 3-22 a simple first order approximation for δ:

$$\delta = \delta_m + \delta_T \cdot \Delta T \qquad 3\text{-}24$$

From Equation 3-18, the minimal value for the slope δ_T is $\approx 7 \times 10^{-25}$ kJ/(nm^2·K). The values of δ_m and δ_T were then found by fitting the model to the onset temperature data.

3.4.3 Energy barrier of activation

We propose that the exponential part of the T&F equation can be estimated by including the entropic component of the free energy of adding one molecule to an embryo. The process of adding a molecule is represented in Figure 3-2, inspired on T&F. The Gibbs energy of the initial and final embryos, as well as the activated state, are placed at their relative energetic level. As in T&F we used the average energy between the two embryos, $\overline{\Delta F_i}$, as the reference level. Hence,

$$\Delta F^x = \overline{\Delta F_i} + \Delta f^x = \frac{1}{2}(\Delta F_i + \Delta F_{1L} + \Delta F_{i+1}) + \Delta f^x \qquad 3\text{-}25$$

The activation energy that we propose is the entropy part of the Gibbs energy of incorporating a molecule to the embryo. Thus,

$$\Delta F^x = (\Delta F_i + \Delta F_{1L}) - T \cdot \Delta S^x \qquad 3\text{-}26$$

The energy of activation is, therefore,

$$\Delta f^x = \frac{\Delta F_i - \Delta F_{i+1} + \Delta F_{1L}}{2} - T \cdot \Delta S^x \qquad 3\text{-}27$$

The entropy difference from the state embryo of "*i*" and a liquid molecule, to the

activated state, is given by:

$$\Delta S^{x} = \frac{1}{N_A} \cdot \left[\int_{T_m}^{T} \frac{\Delta C_p}{T} dT - \frac{\Delta H_m}{T_m} \right] \quad 3\text{-}28$$

The modified T&F term, Δf^{x}, is then:

$$\Delta f^{x} = \frac{\Delta F_i - \Delta F_{i+1} + \Delta F_{1L}}{2} - \frac{T}{N_A} \cdot \left[\int_{T_m}^{T} \frac{\Delta C_p}{T} dT - \frac{\Delta H_m}{T_m} \right] \quad 3\text{-}29$$

The terms of Equation 3-29 are described by expressions 3-30 to 3-32. the difference between ΔF_i and ΔF_{i+1} is:

$$\Delta F_i - \Delta F_{i+1} = \left(\left(i^{\frac{1}{2}} - (i+1)^{\frac{1}{2}} \right) \cdot k_1 - r_a \right) k_0 \cdot 2 \cdot \delta + \Delta G_s \quad 3\text{-}30$$

ΔG_s and δ are defined in Equation 3-19 and Equation 3-24, respectively. The convenience constant, k_1, is:

$$k_1 = \frac{(1 + r_a) \cdot d_0}{(k_0)^{\frac{1}{2}}} \quad 3\text{-}31$$

The Gibbs energy of the liquid molecule is:

$$\Delta F_{1L} = \frac{1}{N_A} \cdot \left(\int_{T_m}^{T} C_p^l dT - T \cdot \int_{T_m}^{T} \frac{C_p^l}{T} dT \right) \quad 3\text{-}32$$

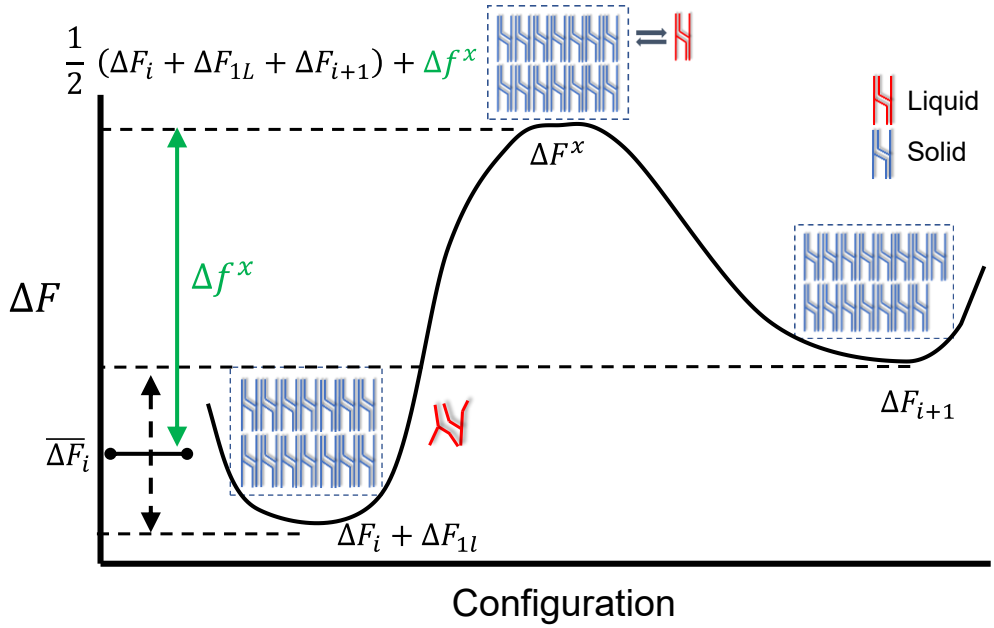

Figure 3-2: A representation of free energy of activation and TAG molecules, modified from Turnbull and Fisher (T&F).

The actual value of the energy barrier, Δf^x, is likely lower than the estimate from Equation 3-29. The Gibbs energy difference between a small embryo and the liquid (less organized than large bulk crystal) is lower than the difference of the bulk phase.[119] The T&F model corresponds to homogeneous primary nucleation. It is experimentally observed that the container affects the observable onset of nucleation, which indicates that heterogeneous nucleation is also taking place. Another reduction of the energy barrier may come from the progressive (zip-like) crystallization of a molecule, rather than its 'all-or-nothing' incorporation to an embryo or to a crystal. Our proposal is thus a first approximation to nucleation and serves as an important base for subsequent refinements.

The expression for the rate of nucleation is complicated, but in the end, it is all a function of thermal properties. They are usually known, except for the interfacial energy of each polymorph. Reported values for δ estimated using spherical geometry are of the

order of 0.1 J/m^2. [120] The asymmetry of the platelets is consistent with three values of δ, one for each surface. [121] The direction of fastest growth corresponds to the lower interfacial energy. The area-averaged value of δ would be:

$$\delta = \frac{\delta_2 \cdot d_0 + \delta_1 \cdot d_0 \cdot r_a + \delta_0 \cdot r_a \cdot \xi}{d_0 + d_0 \cdot r_a + r_a \cdot \xi} \quad 3\text{-}33$$

The subscripts indicate the direction of growth associated with each energy, $\delta_0 > \delta_1 > \delta_2$.

3.4.4 Solving the parabolic partial differential equation

The partial differential equation (PDE), Equation 3-1 is a parabolic PDE. Although challenging, it can be integrated numerically for each polymorph. The integral starts at the melting temperature of the polymorph and ends at the onset temperature of crystallization for that polymorph.

The onset temperature is always lower than the melting point of the β polymorph, otherwise there would be no crystallization whatsoever. Therefore, at all the onsets, there will be a value of the integral for nucleation rate that is larger than zero. The value, however, will be in many cases extremely small, since we did not observe crystallization of β.

For onsets that happen below the melting point of β', the integral runs from the melting point of β' to the onset temperature.

The equation can be reorganized in a standard mode as:

$$\left[\left(\frac{i_s kT}{h}\right) \cdot i^{\frac{2}{3}} \cdot exp\left(\frac{-\Delta f^x}{kT}\right)\right]^{-1} \frac{\partial n_i}{\partial t} = -n_i \frac{2}{3} A \cdot \left(i^{-\frac{1}{3}} - i^{*-\frac{1}{3}}\right) - \frac{\partial n_i}{\partial i} \quad 3\text{-}34$$

Since the changes in n_i are sudden and very large, it is more manageable to solve the problem in its logarithmic space by substituting n_i with an exponential.

$$n_i = e^u \; and \; \partial n_i = e^u \cdot \partial u \tag{3-35}$$

The equation can thus be cast as:

$$c(i,T(t))\frac{\partial u}{\partial t} = s(i,T(t)) - \frac{\partial u}{\partial i} \tag{3-36}$$

With the characteristic terms:

$$c(i,T(t))\frac{\partial u}{\partial t} = \left[\left(\frac{i_s kT}{h}\right)\cdot i^{\frac{2}{3}} \cdot exp\left(\frac{-\Delta f^x}{kT}\right)\right]^{-1} \tag{3-37}$$

$$s(i,T(t)) = -\frac{2}{3}A \cdot \left(\frac{1}{(i)^{\frac{1}{3}}} - \frac{1}{(i^*)^{\frac{1}{3}}}\right) \tag{3-38}$$

$$\frac{\partial}{\partial i} f\left(i,t,u,\frac{\partial u}{\partial i}\right) = -\frac{\partial u}{\partial i} \Longrightarrow f = -u \tag{3-39}$$

The boundary conditions at $i = 2$ and $i = i^*$ are set to satisfy the expression:

$$p(i,t,u) + q(i,t) f\left(i,t,u,\frac{\partial u}{\partial i}\right) = 0 \tag{3-40}$$

At i_l=2, q_l=1; p_l=u_l; f=-u_l and at i_r=i*, q_r=1; p_l=u_r; f=-u_r. After exploration, the initial value chosen for u was -400, which corresponds to $n_i = 2\times10^{-174}$ embryos/nm^3, i.e., a practical zero. Thus, the initial condition is assumed as a uniform and negligible number of embryos. This is for the liquid at temperatures above the melting point of the most stable polymorph. The starting liquid temperature in this work was 373.15 K.

The structure in Equations 3-34 to 3-40 is commonly used in PDE solvers. We wrote code to use the *pdepe()* solver in MATLAB. In standard computers and MATLAB environment the scale of numbers usable are within +/- $10^{+/-307}$. This imposes a limit as to the extent to which solutions of the variable "u" can be calculated. Consider that the changes are more than 10^{614}.

In this work we are interested in the onset of the nucleation event at a particular embryo size i^*. The event itself can be estimated from the trend of the 'catastrophic' increase in smaller sizes. The derivatives tend to an 'effective' infinity ∞_s, i.e., the maximum computational limit of the software.

$$u \to \infty_s; \frac{\partial u}{\partial t} \to \infty_s \; ; \; \frac{\partial u}{\partial i} \to \infty_s \tag{3-41}$$

We assume that the nucleation that produces embryos of the critical size to form at a fast rate coincides with the onset estimated from the DSC thermograms.

As the number of embryos n_i with $i<i^*$ increases, the region of (u,t,i) space within computational range becomes smaller. At the time when the software cannot integrate any further, the integration has often proceeded to between 75% and 93% of that time.

3.5 EXPERIMENTAL PROCEDURES

3.5.1 Materials

Tridodecanoyl-glycerol (LLL, CAS 538-24-9) were purchased from Fluka (via Sigma-Aldrich Chemical Co) with a purity of > 99%.

3.5.2 DSC

Crystallization curves were generated using a heat flux Q100 DSC (TA Instruments, New Castle, DE) equipped with a refrigerated cooling system (RCS). The software was used with the option to obtain raw signals. Cell resistance and capacitance, cell constant and temperature were calibrated following three steps: empty cell check, pure sapphire run, and pure indium run. The sample cell was purged with nitrogen gas flowing at 25 mL/min. Approximately 3−6 mg of sample was placed into hermetically sealed aluminum DSC pans, and an empty sealed aluminum pan was used as a reference.

All the samples were initially heated up to 353 K at a heating rate of 10 K/min, kept isothermal for 7 min to eliminate the effect of 'crystal memory', and then cooled down to 343 K using 9 cooling rates: 25, 20, 17.5, 15, 12.5, 10, 7.5, 5, and 2.5 K/min in a random sequence. 54 cycles (including heating and cooling) were run for each sample without taking the sample out to mitigate variability introduced by pan position.[122] The results were exported from the Universal Analysis software (TA Instruments) into MS Excel format and further processed by a data analyzing method developed by our team in MATLAB.

3.5.3 X-ray diffraction

The synchrotron radiation XRD (SR-XRD) experiments were conducted at the National Synchrotron Light Source (NSLS-I), located at the Brookhaven National Laboratory (Upton, NY, USA), with the synchrotron radiation source at the Exxon Mobil beamline X10A. A Bruker 1500 two-dimensional CCD detector was used to capture diffraction patterns at an exposure time of 5s and another 5s to read and 'unwarp' the images.

The small-angle XRD experiments were conducted at a wavelength of λ=1.09468 Å, with the detector placed at 1014.6 mm from the capillary. The wide-angle XRD experiments were done with the detector located at 136.8 mm away from the capillary. Aluminum oxide and silicon powders were used to calibrate the beam's energy. With a beam size of 0.5 x 0.5 mm, the instrumental resolution was 0.0027$Å^{-1}$. The samples were loaded into a 1.5 mm thin glass capillary that was heated to 343 K for 10 min prior to each experiment. The capillary was cooled under each rate to 263 K and kept there for 5 minutes. The capillary was then heated back to 343 K at a rate of 5.0 K/min. Seven cooling rates were studied: 20, 15, 10, 7.5, 5.0, 2.5 and 1.0 K/min. Using a custom plug-in for ImageJ, the radial averages of the isotropic diffraction patterns were calculated, along with proper normalization of the intensities. Utilizing a modified Levenberg-Marquardt algorithm in Igor Pro 9, the one-dimensional diffraction profiles were fitted to a combination of Gaussian and Lorentzian peak functions.

3.6 RESULTS AND DISCUSSION

3.6.1 DSC thermograms and XRD data

The crystallization onset temperatures were estimated from the sudden change in slope of the thermograms obtained as described in the experimental section. The example in Figure 3-3 shows a set of colling thermograms for a single pan.

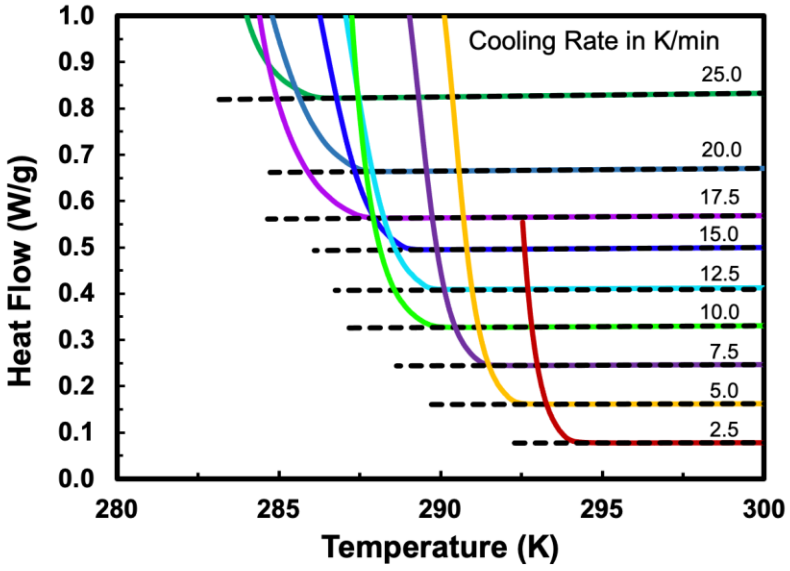

Figure 3-3: DSC Heat flow as a function of temperature at different cooling rates.

The onsets above the melting temperature of the α phase were used for this study. They correspond to cooling rates between 2.5 and 15 K/min. Multiple repetitions were done to obtain the data summarized in Figure 3-4. Performing these repetitions was necessary to account for possible variations in heat capacity due to factors such as pan type and pan placement, as previously discussed in detail. [122] The onset temperatures decreased with the increase in cooling rate, as would be generally expected. The figure shows the

approximation predicted by the model as well, within a 95% confidence interval.

The Hoffman-Weeks[111] extrapolation to zero cooling rate in Figure 3-4 produces a pseudo-melting temperature of around 296 K, which is very far from the actual 308.3 K of β' LLL. This suggests that the actual embryo's melting point is much lower than the melting point of the bulk crystals.

The onset temperatures were the first events to occur during cooling, and it was determined from XRD that they correspond to the to the β' polymorph. The small angle scattering patterns in Figure 3-5 correspond to the 2L β' form of LLL sample cooled at 20 K/min. This was confirmed by the wide angle XRD patterns captured simultaneously (not shown).

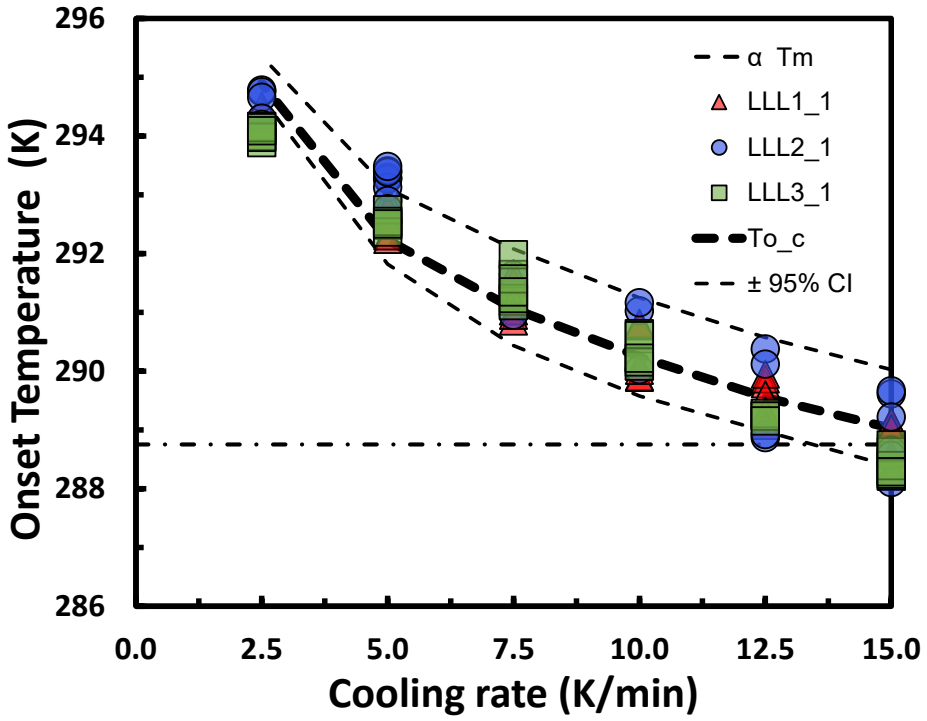

Figure 3-4: Onset temperature of crystallization as a function of cooling rate for the β' polymorph. The dot-dash line indicates the melting temperature for the α phase. The dashed lines are the prediction of the model and its 95% confidence interval.

The example in Figure 3-5 is representative of the other cooling rates explored in this study as well. The scattering peak of the crystallization of the β' polymorph is seen at the onset temperature (at 290.9 K) along with its subsequent growth as cooling continued.

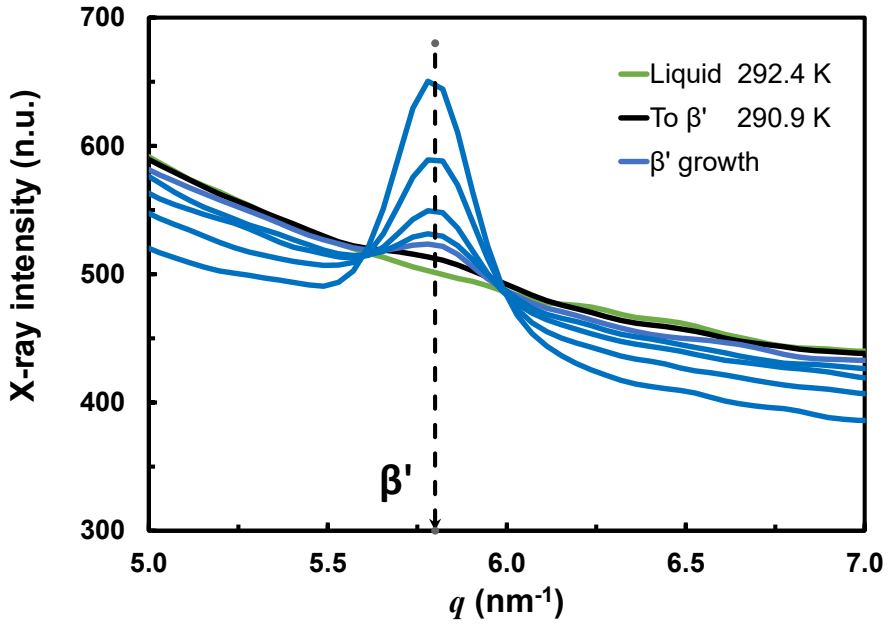

Figure 3-5: X-ray scattering/diffraction intensity for the (003) reflection normalized to account for sample attenuation and incident X-ray beam intensity, as function of scattering vector q (nm^{-1}). The LLL sample was cooled at 20 K/min from the melt in a capillary.

As has been reported[123] experiments done in different sample containers (DSC pans, microscope slides, glass capillaries, etc.) provide a different range of estimated onset temperatures. This is due to different surfaces and different heat transfer geometries and rates. Nonetheless, the melting thermograms confirmed as well the initial formation of phase β', which is consistent with other literature sources. [124] At lower cooling rates the formation of β' was similarly observed.

3.6.2 Non-isothermal analysis

The PDE was solved with an initial estimate of the interfacial energy parameters δ_m and δ_T in Equation 3-24, that were refined afterwards. The slope parameter δ_T was replaced by

a more tangible value, δ_{23}, which is the value expected at the deepest practical undercooling, *i.e.,* $\Delta T \approx 23$ K. The slope δ_T is thus,

$$\delta_T = \frac{\delta_{23} - \delta_m}{23} \tag{3-42}$$

A search algorithm was coded in MATLAB to find the values of δ_m and δ_{23} that minimized the sum of squared errors with respect to the observed onset times, t_r. The time t_r for a cooling rate c_r (K/s), is:

$$t_r = \frac{T_m - T_o}{c_r} \tag{3-43}$$

An example of the time-temperature evolution of $\log(n_i)$ is shown in Figure 3-6, further transformed by logarithmic coordinates. Due to the numerical limit of the computations, the integration stopped before the 'catastrophic' front of growth of the number of embryos of each family reached the critical nucleation size i^*. It was observed that the front followed a smooth path in the coordinate system of the function time t_{uf} and the $\log(i/i^*)$.

The search was done with the set of temperatures at the average, and within two standard deviations from the average (95% confidence interval). The red line in Figure 3-6 shows the front of catastrophic increase in embryo numbers during cooling at 15 K/min. As was done with the quasi-isothermal simulations, the front was extrapolated from the point where the calculation stopped due to overflow.

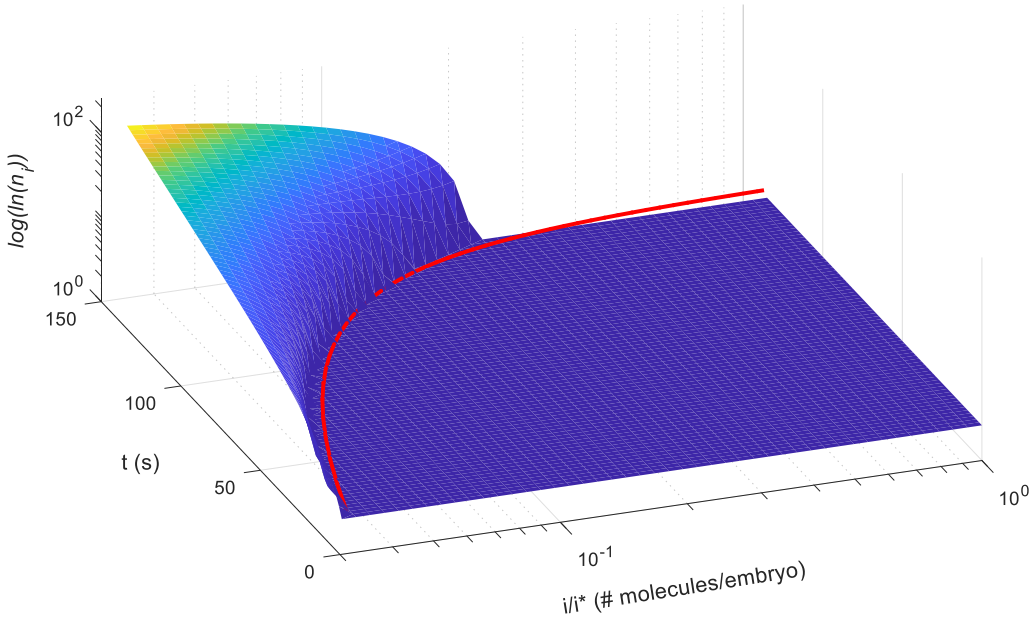

Figure 3-6: Double logarithm of the number of embryos of a class, n_i, as a function of time t_{uf} and the ratio i/i^*, during cooling at 15.0 K/min to T_o 288.74 K. Cooling time t_r = 78.3 s ≈ 54 t_{uf} units. The critical embryo size was i^* = 44 molecules. The red line is the front curve.

The advance of this edge was then used to estimate the actual time t_{rf} needed to reach i/i^*=1, as shown in Figure 3-7. The extrapolation was done with the three-term power law in Equation 3-44 and illustrated in Figure 3-7 (A):

$$t_{rf} = b_0 + b_1 \cdot \left(i/_{i^*}\right)^{b_2} \qquad 3\text{-}44$$

The extrapolated values were converted to estimated real times t_{rf} using Equation 3-44 and then the relative error ϵ_t was calculated:

$$\epsilon_t = \frac{t_r - t_{rf}}{t_r} \qquad 3\text{-}45$$

The sum of the squared errors was minimized by changing δ_m and δ_{23}. The values

obtained from the minimization were $\delta_m = 0.8351\times10^{-24}$ and $\delta_{23} = 18.1\times10^{-24}$ kJ/nm^2. A similar procedure was followed for the temperatures at the 95% confidence interval limits (see Table 3-2).

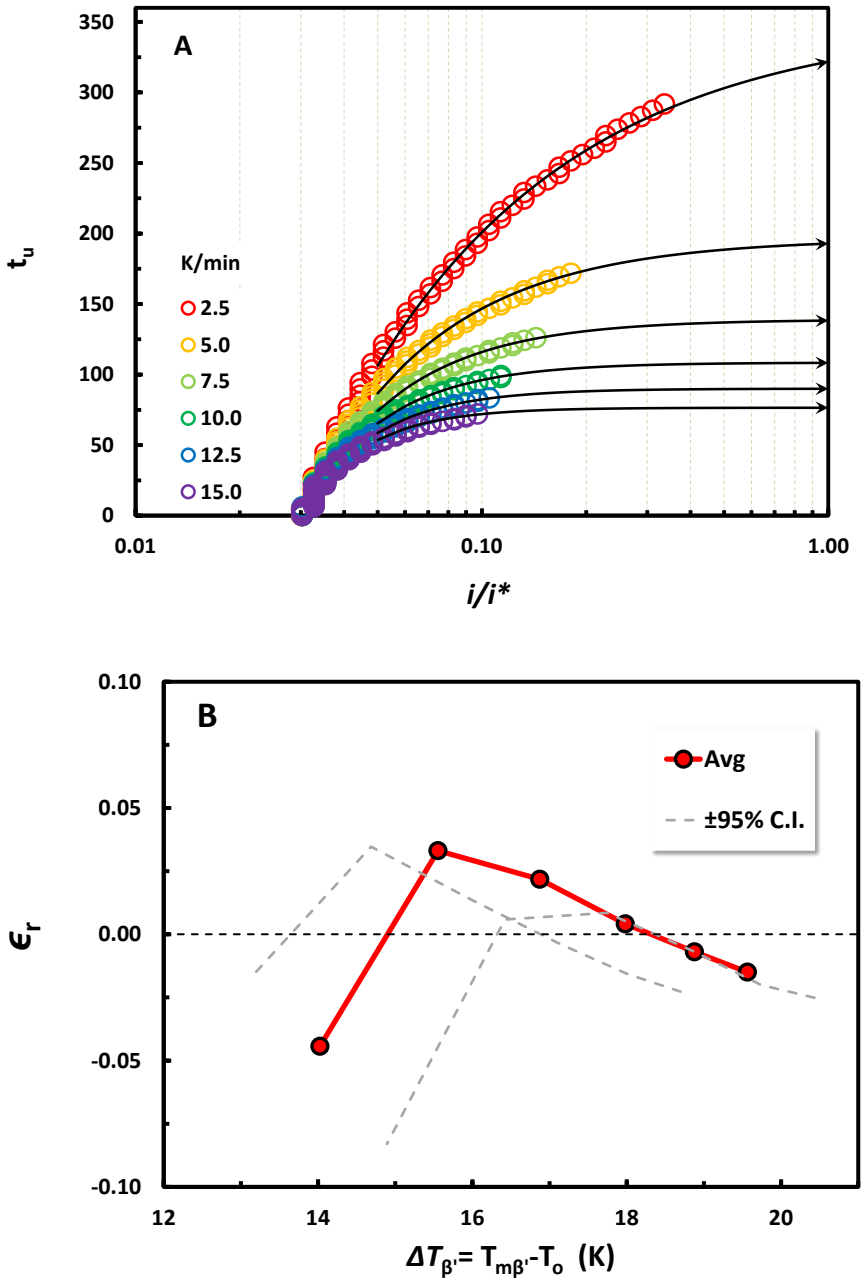

Figure 3-7: (A) Processing time as a function of i/i^* for three cooling rates. The lines show the extrapolation to find the end t_{uf}. (B) Relative error ϵ_t of time estimates as a function of temperature undercooling ΔT (K).

Table 3-2: Parameters for interfacial energy estimation.

	95%-	Average	95%+
$\delta_m \times 10^{-24}$ kJ/nm^2	0.500	0.8351	1.182
$\delta_T \times 10^{-24}$ kJ/nm^2	0.648	0.7506	0.935

The distribution of the relative errors is shown in Figure 3-7 (B). The errors are within 5%, except for the slow cooling rate (small ΔT). The trend is an indication that the approximation of the interfacial energy as a linear function of temperature needs refining.

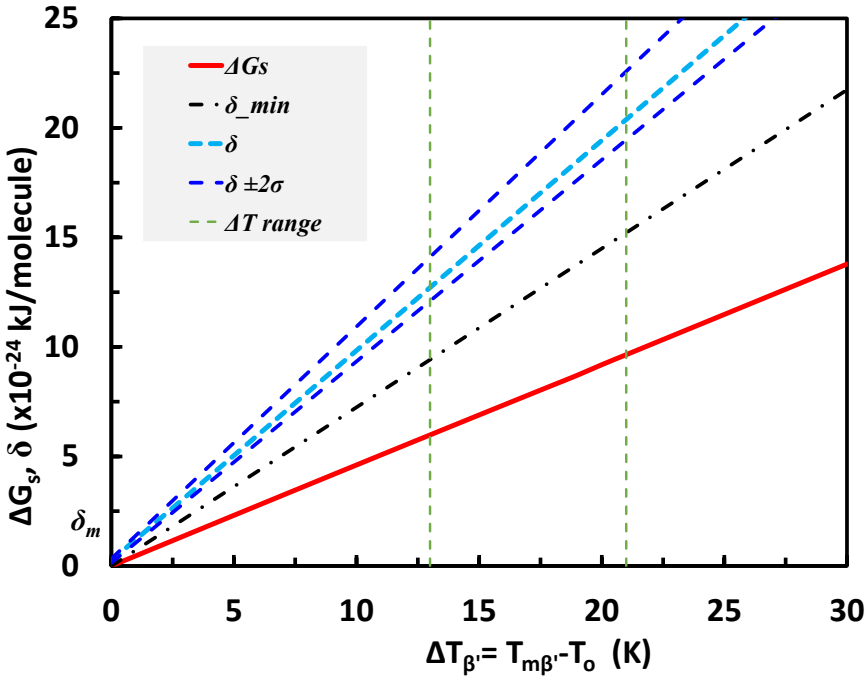

Figure 3-8: Solid-liquid chemical potential ΔG_s, and interfacial energy δ, as a function of undercooling ΔT. (Cf. Eq3-24).

The calculated interfacial energy δ as a function of undercooling ΔT is plotted, along with the chemical potential ΔG_s, in Figure 3-8. The minimal estimate for δ from Equation 3-18 is plotted as a dash dot line.

These interface energy and chemical potential values determine the Gibbs energy ΔF as a function of temperature and number of molecules in the embryo, following Equation 3-10. If the interfacial energy δ was constant, ΔF and ΔF^* values would increase as the temperature increases. The interfacial energy, however, decreases with temperature. Therefore, the ΔF and ΔF^* values decrease with increasing temperature, as seen in Figure 3-9(A). The position of the maxima, i^*, computed with Equation 3-11, decrease slightly with increase in undercooling ΔT. For any pure liquid, as the undercooling increases, the critical nucleus formation size, i^*, is reduced. The increase of interfacial energy with undercooling softens this reduction. Thus, the calculated critical size i^* seen in Figure 3-9(B) changes much less than the i^* values calculated from a constant δ. Therefore, it takes longer to reach the nucleation condition of $i=i^*$when δ increases with ΔT. The nucleus size ξ^* corresponding to $i^* \sim 45$ molecules is around 2.8 nm, with ξ_2^* 5.9 nm.

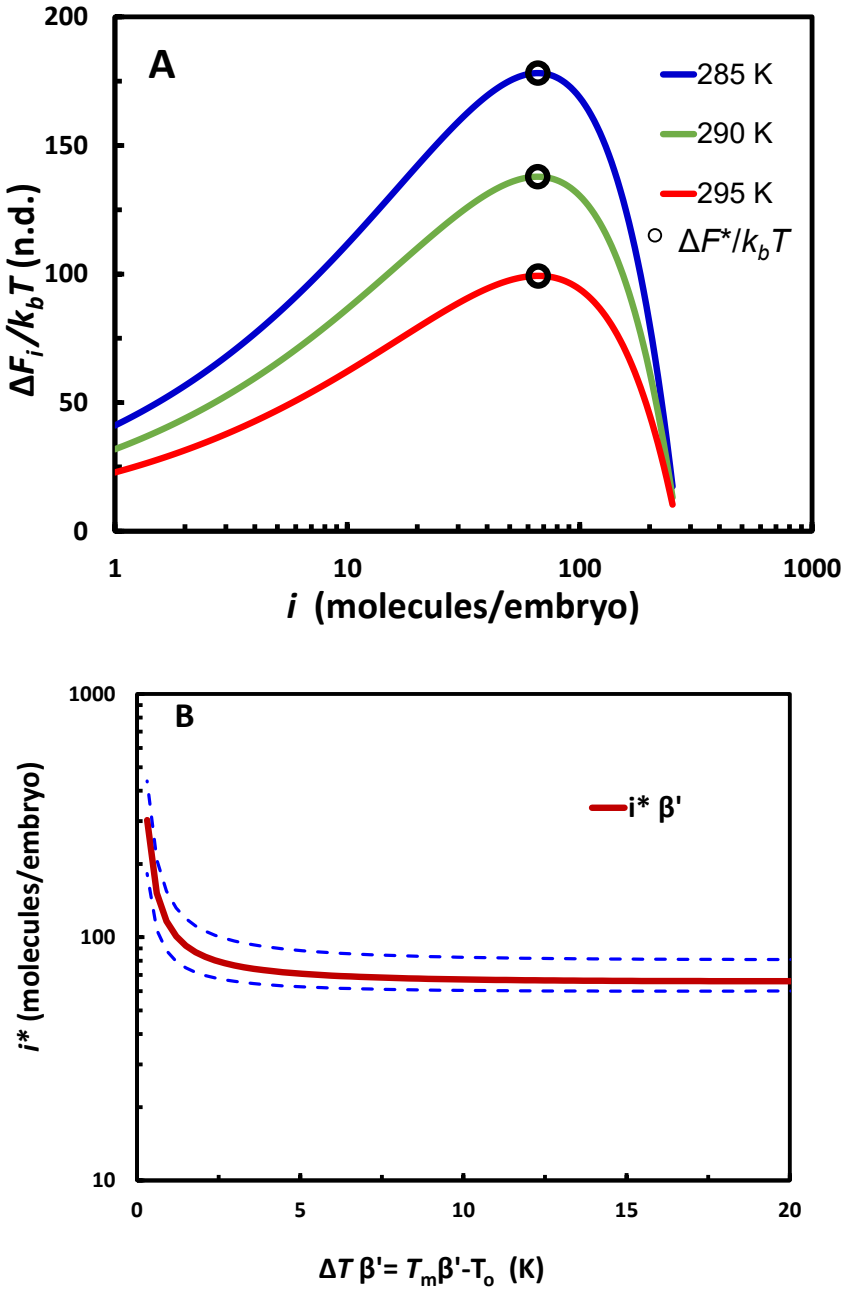

Figure 3-9: (A) Free energy of embryos and nuclei as a function of the number of molecules in a platelet, for the β' polymorph, at three temperatures (see Equation 3-14). (B) Number of molecules per embryo (molecules/embryo) at the critical nucleus size, i^*, as a function of undercooling ΔT (K) with its 95% confidence interval.

3.7 CONCLUSIONS

In this paper, we have presented a conceptual and numerical method to solve the T&F nucleation model [5] for a molecular liquid during its undercooling. Any time-temperature cooling profile requires finding a solution for the partial differential equation (Equation 1) under non-isothermal conditions, which is not trivial. We introduced, for a specific polymorph of triacylglycerol, the mono-layer nano-platelet embryo idea, in contrast to the traditional sphere. Based on the geometrical aspect ratio and specific volume of this embryo, we developed a method to calculate the number of growing molecules on its surfaces per unit time. Moreover, we propose an interfacial energy that is temperature dependent, and an energy of activation that is temperature and size dependent as well. In addition, we considered the energy changes caused by temperature changes in the specific heats of liquids and solids. We created a numerical framework in MATLAB to solve the T&F nucleation model based on the liquid and crystalline solid material properties, such as equilibrium melting temperature, enthalpy, specific heat, interfacial energy, and crystallographic dimensions. This was accomplished by solving complex (stiff) differential equations numerically. Moreover, this framework implements a numerical solution of the T&F model including an interfacial energy that is temperature dependent, and an energy of activation that is temperature and size dependent as well. We proposed that the entropic component of the free energy of adding one molecule to an embryo can be used to estimate the exponential part of the T&F (Equation 3-27). We then proceeded to demonstrate how the T&F model can be used to estimate temperature-dependent interfacial energy. Therefore, it can be used to predict the onset temperature of nucleation at given cooling rates. The pure TAG used in this study is part of a family of materials

extensively used in the pharmaceutical, nutritional, and cosmeceutical industries. More importantly, it provides a methodology to extend these estimates of interfacial energy to many other molecular liquids. This method also sets the foundation required to extend this model to include molecular mixtures.

3.8 AUTHOR INFORMATION

Corresponding Author

* Gianfranco Mazzanti, mazzanti@dal.ca, Department of Process Engineering & Applied Science, Faculty of Engineering - Dalhousie University, Room F2215- 5273 DaCosta Row, Halifax, NS, Canada B3H 4R2.

3.9 AUTHOR CONTRIBUTIONS

The manuscript was written through significant contributions of all authors. All authors have given approval to the final version of the manuscript.

3.10 ACKNOWLEDGMENT

We appreciate the technical support of Steve Bennett at NSLS, and of Pavan K. Batchu for XRD work. Canada NSERC Discovery Grant.

CHAPTER 4 ONSET CRYSTALLIZATION TEMPERATURES OF MOLECULAR LIQUIDS – PART 2 – IS THERE A VIOLATION OF MONOTROPIC POLYMORPHISM OF FORM A IN TRIDODECANOYL-GLYCEROL (TRILAURIN)?

4.1 PUBLICATION INFORMATION

This chapter is a modified version of a manuscript that will be submitted as:

Omar Al-Qatami, Xinyue Zhang, Gianfranco Mazzanti (2023). Onset crystallization temperatures of molecular liquids – part 2 – is there a violation of monotropic polymorphism of form α in tridodecanoyl-glycerol (trilaurin)? Journal of the American chemical society (JACS). (In preparation).

4.2 ABSTRACT

In the second part of this article, we extend our previous investigation on the crystallization temperature and polymorphic forms of liquid triacylglycerols (TAGs), with a focus on the tridodecanoyl-glycerol (LLL, CAS 538-24-9) system. Expanding upon the first part, which utilized the differential form of Turnbull and Fisher's (T&F) homogeneous nucleation theory, we further examine the factors that affect nucleation onset temperatures and the formation of different polymorphs at a range of cooling rates. The nucleation rate for the α polymorph was computed following the differential form of the T&F model using a MATLAB code. To identify the second onsets of the α form, we employed a modified version of the Avrami method. The nucleation of the α polymorph was modeled as heterogeneous secondary nucleation of one polymorph on another, in which the formation of a viable α polymorph nucleus on the surface of the β' crystals is the rate

limiting step.

4.3 INTRODUCTION

The crystallization process of TAGs, which include edible fats, plays a crucial role in various industries, such as food [125, 126], pharmaceuticals [127, 128], and cosmetics[129]. During industrial production, these materials crystallize under non-isothermal conditions, meaning that the temperature changes as the material crystallizes over time. The way these materials crystallize, and their resulting structures are highly sensitive to heat and mass transfer conditions, which in turn significantly influence their mechanical strength, flow properties, and sensory texture.

A particularly important aspect of the crystallization process is the nucleation behavior, as it directly affects key structural features like the number, size, and shape of the crystallites, as well as the distribution of mass within the material. However, despite the importance of understanding nucleation behavior in these complex organic materials under non-isothermal conditions, there are currently no theoretical models that account for the intricate polymorphic transformations these materials undergo during crystallization. For pure TAGs, there are three main monotropic polymorphic crystalline forms, α , β', and β in an increasing thermal stability order and structural density, often with sub-varieties.[107] The polymorphic form of TAGs significantly impacts the physical characteristics of fat-containing products. This influences hardness, melting behavior, texture, glossiness, stability, and mouthfeel. For instance, the most densely packed β-form results in a harder product with a higher melting point, making it more resistant to changes in environmental conditions but potentially giving it a grainy texture. The loosely packed α-form, conversely, produces softer products that melt at lower temperatures and possess a

smoother texture. In between, the β'-form presents a balance of properties.

The study of monotropic transformations in TAGs is crucial due to their significant impact on various applications. One prime example is cocoa butter, a key ingredient in chocolate, which exhibits a complex polymorphism with six distinct polymorphs (I to VI), including two β' and two β forms[130]. For commercial chocolate, TAGs are typically found in the well-organized β_V form. Over time, this form undergoes a transformation into the β_{VI} form, the most stable polymorph of cocoa butter. This change is responsible for the deterioration of chocolate products, a phenomenon commonly known as fat blooming [131]. A deep understanding of the phase behavior of fat-based systems is indeed crucial for controlling and predicting their properties, which ultimately enables the optimization of formulations that use healthier or more sustainable raw materials.

In our previous work[132], we developed a conceptual and numerical method to solve the T&F [5] nucleation model for a molecular liquid during its undercooling. A monolayer nanoplatelet embryo concept, as opposed to the traditional sphere, for a specific polymorph (β' polymorph). These polymorphs were identified at the onset temperatures using SAXD and WAXD studies.

We developed a method to calculate the number of growing molecules on the embryo surfaces per unit time and proposed temperature-dependent interfacial energy and energy of activation.[132] Using a numerical method in MATLAB, a numerical framework was developed which takes into account liquid and crystalline solid properties such as melting temperature, enthalpy, specific heat, interfacial energy, and crystallographic dimensions. This method proved successful in predicting the onset temperature of a tridodecanoyl-glycerol (trilaurin, LLL) sample cooled at different cooling rates.

Compelling experimental evidence strongly supports the idea that nucleation from the melt is a crucial factor in the formation of polymorphs. However, the exact mechanism responsible for selectively generating specific polymorphic structures remains unclear.

We propose that the less stable α polymorph crystallizes on the more stable β' polymorph, a process that appears to contradict the Ostwald 'Rule of Stages'. This rule suggests that metastable polymorphs should transform in a sequential manner into increasingly stable forms. Our theory posits that α polymorphs nucleate from non-polymorph-specific embryos and directly from the liquid. We also hypothesize that the β' polymorphs act as a template onto which α polymorphs start to nucleate, a phenomenon commonly referred to as cross-nucleation [133] or concomitant polymorphism [21] through a heterogenous nucleation process.

In this study, we aim to build upon our previous work[132] by applying the established framework to elucidate the appearance of the α polymorph following β'. The significance of our research lies in its potential to serve as a valuable predictive tool for a range of industries, including pharmaceuticals, chemicals, food science and technology, energy storage, and cosmetics. It also has applications in multiple scientific fields such as materials science, environmental science, and space exploration. This tool offers the unique capability of accurately predicting both the temperature at which crystallization occurs and the subsequent polymorphic form. Historically, predicting such complex phenomena has posed a significant challenge for scientists, making this development a considerable breakthrough in the field.

4.4 NUCLEATION MODEL

In this study, we focus on the T&F [5] partial differential equation, which calculates the rate of formation of embryo populations with "i" molecules per unit volume, denoted as n_i:

$$\frac{\partial n_i}{\partial t} = \left(\frac{-i_s k_b T}{h}\right)\left[n_i\left(\frac{2}{3}A \cdot i^{-\frac{1}{3}} - B\right) + \frac{\partial n_i}{\partial i}\right] \cdot i^{\frac{2}{3}} \cdot exp\left(\frac{-\Delta f^x}{k_b T}\right) \qquad 4\text{-}1$$

where i_s is the number of molecules at the surface of the embryo, k_b and h are Boltzmann's and Planck's constants, respectively; T is the temperature in K; A and B are both functions of the interfacial and volume energies; Δf^x is the Gibbs activation energy barrier, with respect to average energy between an embryo of "i" molecules and one of "$i+1$" molecules, at a given temperature; $\frac{\partial n_i}{\partial t}$ is the rate of number increase of each class of embryos; and $\frac{\partial n_i}{\partial i}$ is the gradient of the number of embryos of each class with respect to the number of molecules in the embryos.

The terms of Equation 4-1 depend on the material properties of the liquid and the crystalline solid, *e.g.*, equilibrium melting temperature, enthalpy, specific heat, interfacial energy, and crystallographic dimensions. These properties are a function of temperature.

In the next three subsections we discuss the terms that form Equation 4-1 providing a detailed explanation of their derivation. The fourth subsection explains the numerical strategy used to compute solutions of Equation 4-1 to estimate the interfacial energy parameters.

4.4.1 Geometrical properties of the nanoplatelet embryos

As this work focuses on the nucleation of both crystallizing polymorphs, α and β', the properties of two polymorphs need to be known and these are summarized in Table 4-1. The specific heat of the liquid is independent of the polymorphic forms. The specific heat of the crystals is a second order polynomial. The coefficients in the table are for temperatures in K. As can be seen in the table, the enthalpy values of these polymorphs are quite different. The enthalpy of melting, the energy needed to change a solid into a liquid, differs between the polymorphic forms of TAGs due to their varying molecular arrangements. The loosely packed α-form requires less energy to melt, hence lower enthalpy, while the densely packed β-form, with stronger intermolecular forces, requires more energy, hence higher enthalpy. The β'-form, being intermediate in packing and stability, has an enthalpy of melting between the α and β forms. The large difference in the enthalpy values between the different polymorphic forms of TAGs can be attributed to the significant differences in the molecular packing arrangements and the strength of the intermolecular forces in the solid forms. It's this variation in structure and stability that affects the amount of energy needed to induce a phase change from solid to liquid.[134]

Table 4-1:. Properties of the polymorphic forms for tridodecanoyl-glycerol (trilaurin)

	Polymorphic Form			
	α	β'	β	Ref.
T_m, *K*	*288.8*	*308.3*	*318.9*	*21*
ΔH_m, kJ/mol	69.8	86.0	122.2	22
vs, nm^3/molecule	1.110	1.103	1.015	23
C_{p0}, kJ/(K·mol)	2.55	3.46	2.79	24
C_{p1}, kJ/(K^2·mol)	-1.62×10^{-2}	-2.26×10^{-2}	-1.68×10^{-2}	24
C_{p2}, kJ/(K^3·mol)	4.86×10^{-5}	5.68×10^{-5}	4.30×10^{-5}	24
r_a	1.8	2.1	2.4	14
d_0, nm, $\xi_0=1/d_0$	3.52	3.25	3.12	21
m_0, molecules/nm	0.2841	0.3077	0.3205	
m_1, molecules/nm	1.781	1.672	1.556	
m_2, molecules/nm	1.781	1.762	1.835	
$C_{p\mathrm{Liq}}$, kJ/(K·mol)	$1.222 + 2.443\times10^{-3}\cdot T$			25

The embryos are assumed to be a monolayer nanoplatelet made of pairs of molecules in complementary vertical arrangement side by side, known as 2L[107] (Figure 4-1). Thus $\xi_0 = d_0$. The aspect ratio of the single layer embryo or nucleus is $r_a = \xi_2/\xi_1$. The surface area and the volume of the platelet, as a function of the second dimension $\xi = \xi_1$, are in Equation 4-2

$$A_p = 2 \cdot (d_0 + r_a \cdot \xi + d_0 \cdot r_a) \cdot \xi; V_p = d_0 \cdot r_a \cdot \xi^2 \qquad 4\text{-}2$$

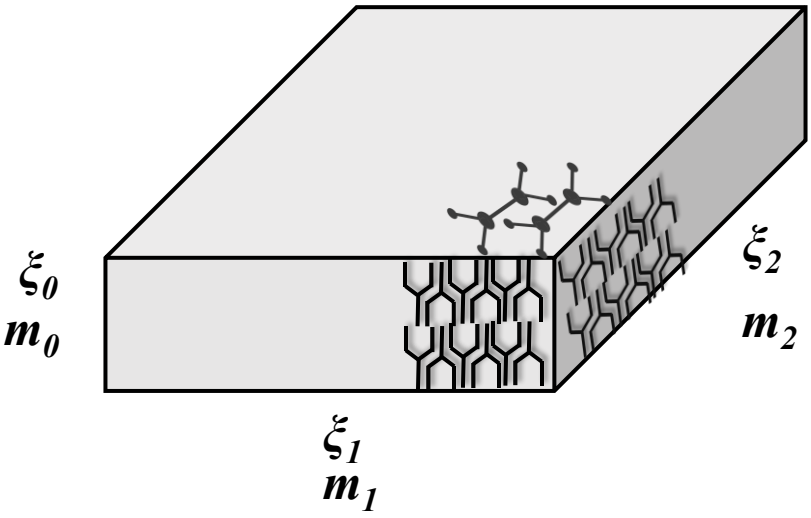

Figure 4-1: Idealized representation of nanoplatelet sizes (ξ_0, ξ_1, ξ_2) and molecules/nm (m_0, m_1, m_2). ξ_0 is in the direction of the crystallographic b axis in references [18] [117]

Each polymorph has its own aspect ratio. Common values of r_a are around 2.4 for the β polymorph. The values for the other polymorphs have been estimated from crystallographic information. [23] The molar volume of each molecule in an embryo is v_s, in nm^3/molecule. The number of molecules "i" in a platelet is, therefore:

$$i = \frac{d_0 \cdot r_a \cdot \xi^2}{v_s} \qquad 4\text{-}3$$

The number of molecules per unit length (molecules/nm) on each side of the platelets are m_0, m_1, and m_2, so that:

$$i = m_1 m_2 \cdot r_a \cdot \xi^2 \qquad 4\text{-}4$$

These values must satisfy the specific volume of a molecule, v_s, by the relationship:

$$\frac{1}{m_0 m_1 m_2} = v_s \qquad 4\text{-}5$$

The "i_s" in the first term of the T&F equation (Equation 4-1) is the number of molecules at the growing interfaces of the nano-embryo. It depends on the area/volume ratio of the shape of the embryos, assumed here as monolayer the nanoplatelet crystals. The ratios and molecules per side depend on the polymorph. They have been estimated from crystallographic information.[23] The platelet thickness ξ in nm is known from X-ray diffraction for the crystals and will be used here as an estimate for the embryos. For a single lamella embryo, $m_0 = 1/d_0$. Thus:

$$i_s = 2 \cdot (m_1 + r_a \cdot m_2) \cdot \xi \qquad 4\text{-}6$$

With a convenience constant k_0:

$$k_0 = \frac{v_s}{d_0 \cdot r_a} \qquad 4\text{-}7$$

To put it as a function of the number of molecules in the embryo's platelet:

$$i_s = 2 \cdot (m_1 + r_a \cdot m_2) \cdot (k_0)^{\frac{1}{2}} \cdot i^{\frac{1}{2}} \qquad 4\text{-}8$$

"i_s" is the maximum number of molecules on the surface of the embryo. This number is the highest for homogeneous nucleation, where each embryo is fully surrounded by liquid molecules. This value is smaller for heterogeneous nucleation because only a fraction of the molecules are in contact with the liquid.

"i_{st}" is the actual number of molecules in contact with the liquid for heterogenous nucleation, given by:

$$i_{st} = x_t \cdot i_s \quad \text{4-9}$$

The fraction of molecules exposed to the liquid is x_t, hence the fraction of molecules between α and β' is (1- x_t).

4.5 NUCLEATION, CRYSTALLIZATION, AND GROWTH

4.5.1 Typical crystallization of a TAG cooled slowly and rapidly.

This section clarifies the terminology used in our work to mitigate misunderstandings. Figure 4-2 exemplifies events that occur when a TAG is cooled below the melting temperatures of its polymorphs. During cooling below the melting temperature of a polymorph, the molecules start to form embryos according to Equation 4-1. This state is labeled 'pre-nucleation' or 'PN' (as shown in Figure 4-2, 'A' and 'C'), since it happens before any embryo reaches a nucleus size. The PN begins as soon as the melting temperature of a polymorph is crossed.

This PN continues until embryos reach a critical size and become for an instant a stable nucleus. Immediately after they start to grow and are no longer a nucleus, but rather a growing nanocrystal. The temperature at which this happens for the first time is termed the 'onset temperature' or 'T_o', determined from experimental observations, primarily from DSC or XRD data. Subsequently, these crystals grow. The rate at which nuclei are formed at a given time/temperature denoted as 'NR' (Nucleation Rate) and the rate at which the crystals grow is called 'GR'.

For illustration, consider the situation where a TAG is slowly cooled (Figure 4-2, 'A' and 'B') and reaches a temperature below the melting point of the α polymorph. At a

temperature, T, where T_m β >T> T_m β', TAG molecules begin to aggregate into the β type and remain so until they achieve a stable size for crystallization. Unless they reach this size, they will not crystallize.

As the temperature continues to drop and T_m β' >T> T_o β', the liquid enters a condition where both polymorphic types can form embryos, but neither crystallizes because they have not reached their respective critical sizes. When T_o β'>T> T_m α, both pre-nucleation states of the β' and β' continue, while the β' type embryos have reached the critical size, leading to their nucleation and growth. This process is reflected in DSC thermograms as the onset temperatures of crystallization. Upon further cooling, and once the temperature reaches T< T_m α, pre-nucleation of the α polymorph will occur. At this stage, the crystallization and growth of the β' polymorph dominates the crystallization process due to its kinetic favorability. These states, including the pre-nucleation (PN), nucleation (NR), and growth (GR) of the polymorphs, are depicted as overlapping colored areas in Figure 4-2 'B'. The red area (representing the pre-nucleation of the α polymorph) is engulfed within the blue area (representing the crystallization and growth of the β' polymorph). This visualization emphasizes that β's crystallization ultimately governs the crystallization process.

Let us now turn our attention to the scenario where a TAG is cooled at a relatively rapid rate, as depicted in Figure 4-2, 'C'. As in the slow cooling scenario, a cascade of events unfolds when T falls below T_m α. However, in this case, the nucleation and growth (NR and GR) of the α polymorph outpace those of the β' polymorph. This happens because the α polymorph becomes more kinetically favorable at this point. Consequently, the onset temperature (T_o α) that is detected experimentally corresponds to the α

polymorph, not the β' polymorph. The grey area in Figure 4-2, 'D' illustrates the crystallization and growth of the α polymorph. The overlapping-colored areas in the figure represent the coinciding events during the cooling process.

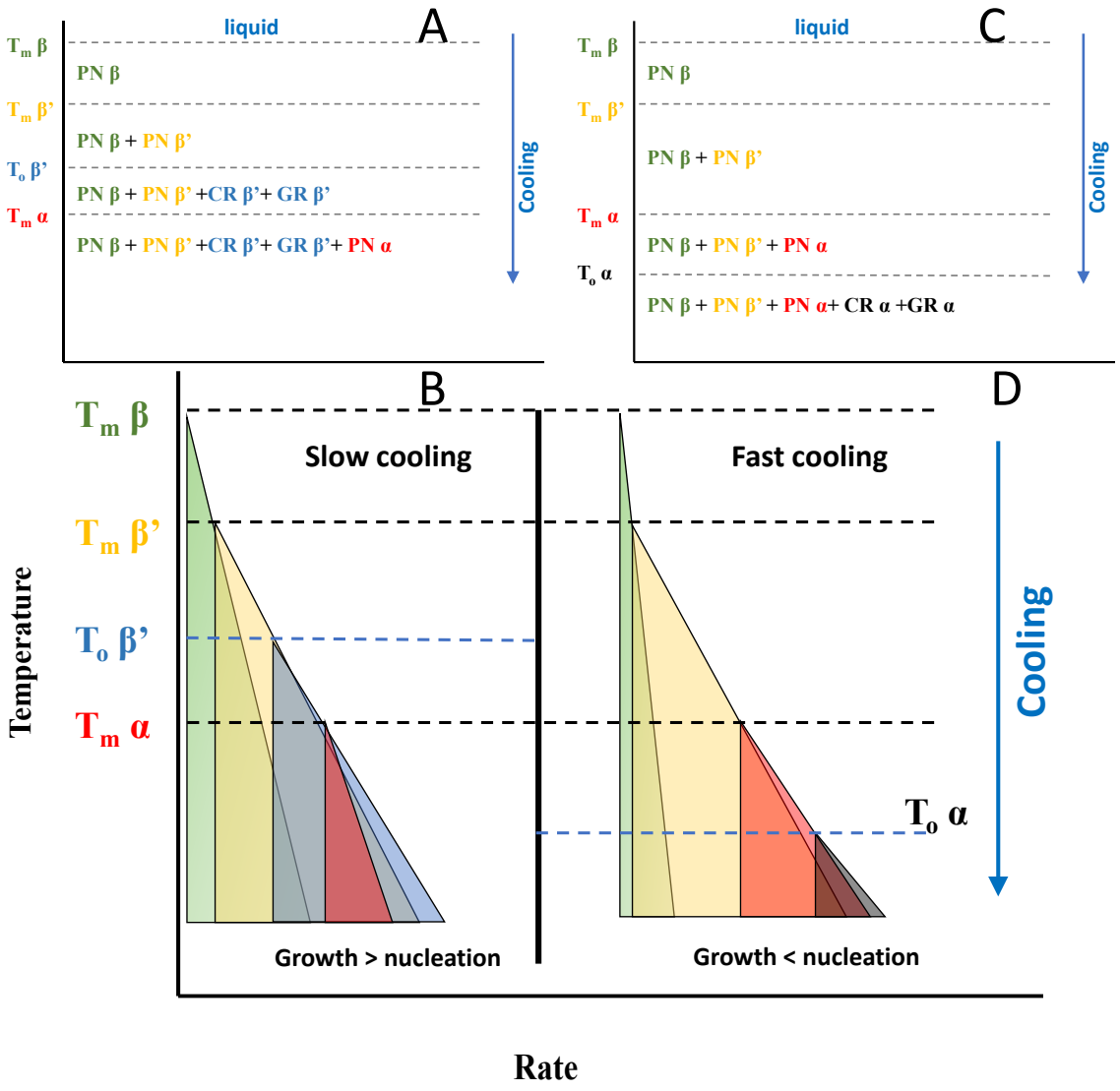

Figure 4-2: Conceptual representation of the possible molecular sates occurred when a liquid TAG is cooled below the melting temperatures of the three main polymorphs during the cooling process. PN: Pre-nucleation, NR: Nucleation, and GR: Growth.

A pertinent question to consider is: How do we discern whether these early-stage formations in the pre-nucleation (PN) region are crystalline structures or merely amorphous

solids exhibiting a glassy phase? The short answer to this question is that we do not know, given the fact that these structures have short-range order too weak to be detected by the techniques used thus far. Despite the nucleation process of TAGs occurring at scales too minuscule for direct observation with standard techniques, it is possible to deduce the formation of crystalline structures based on the observable behaviors and properties during crystallization. Unlike the disorderly structure of an amorphous glass state, crystals are characterized by ordered, repeating structures. These distinct structural differences result in unique physical properties in the resultant materials. Crystalline substances, for instance, display sharp melting points in contrast to amorphous substances, which gradually soften over a temperature range. From our experience and from the literature, it is challenging to form glassy materials with the TAGs despite how fast they are cooled. Furthermore, the observation of sharp crystallization and melting points in DSC analyses and discernible diffraction patterns in X-ray studies suggest crystalline behavior. Other properties, such as hardness, glossiness, and stability—elements influenced by the polymorphic form of TAGs—also correspond with characteristics of crystalline behavior.

4.5.2 Crystallization of LLL cooled slow and fast:

For all the cooling rates explored in the study, both α and β’ polymorphs crystallized at the end of the cooling ramps, but with different proportions. Faster cooling rates produced more of the α polymorphs, as evident from the XRD data. Figure 4-3 represents the possible scenarios of PN, NR and GR for the LLL sample.

Figure 4-3 part 'A' illustrates that the processes of pre-nucleation (PR), nucleation (CR), and growth (GR) for both polymorph types occur when the temperature falls below the

onset temperature of the α polymorph ($T<T_o$ α). The variation in the sizes of the colored regions in parts 'C' and 'D' highlights that both the nucleation and growth rates differ depending on whether the cooling rate is slow or fast.

For instance, the pre-nucleation of the α polymorph, depicted as the red area in parts 'B' and 'C', is more extensive during slow cooling compared to fast cooling. This is attributed to the larger time-temperature trajectory in the slow cooling scenario than in the fast cooling one, which results in higher GR. The time-temperature trajectory[103], visualized as the shaded area in Figure 4-4, directly influences the magnitude of free energy of formation Equation 4-23. Despite the undercooling magnitude being the same (ΔT) for both cooling rates in Figure 4-4, the time-temperature trajectory is significantly larger in the case of slow cooling (shaded area). Consequently, this allows molecules more opportunities to aggregate and interact, leading to the formation of larger, albeit fewer, crystals[135]. In contrast, fast cooling typically results in smaller crystals, but their numbers are generally higher due to reduced time for molecular aggregation and interaction.

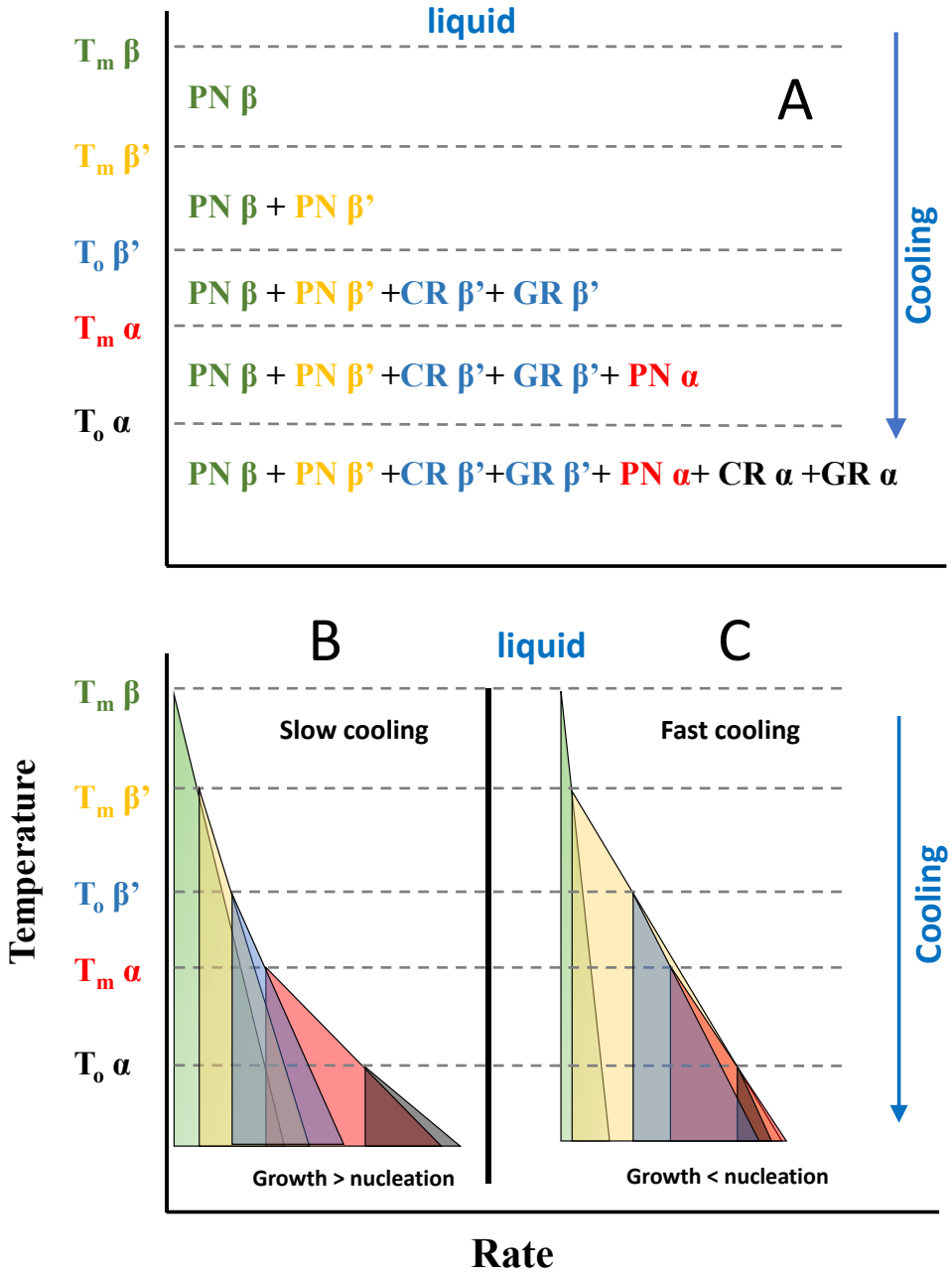

Figure 4-3: Conceptual representation of the possible molecular sates occurred when a liquid LLL is cooled below the melting temperatures of the three main polymorphs during the cooling process. PN: Pre-nucleation, NR: Nucleation, and GR: Growth

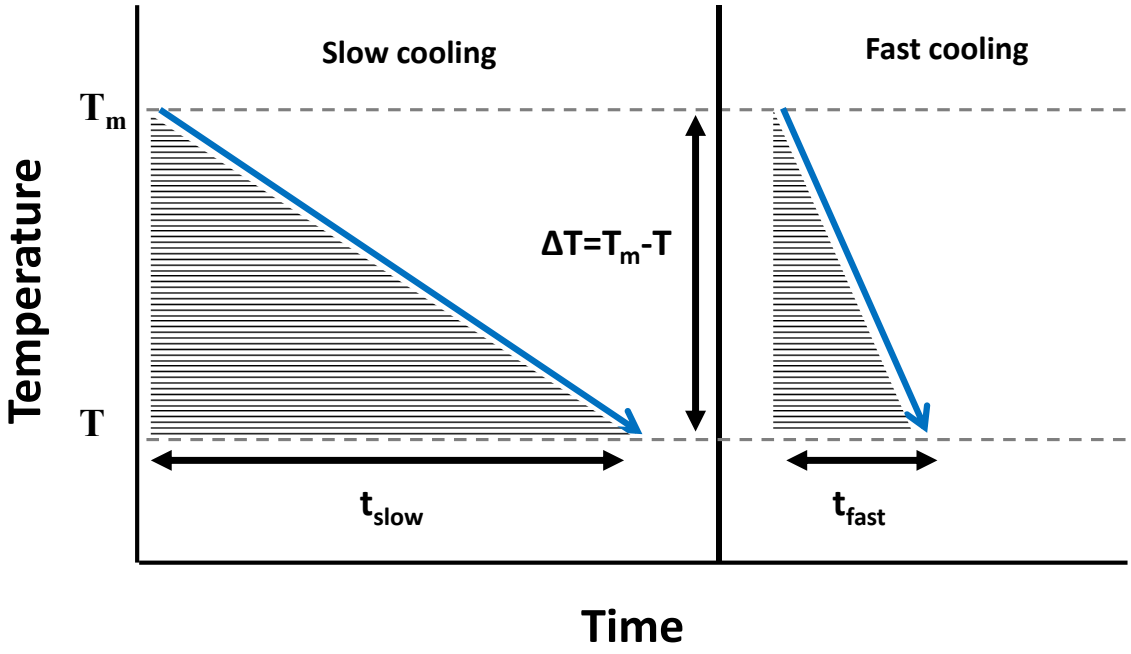

Figure 4-4: The difference in the time-temperature trajectory between slow and fact cooling rates. ΔT is the same in both cases, but the time needed to reach a temperature T (t_{slow}) is longer in the case of the slow cooling rate event (left) compared to that of the fast-cooling rate (right).

4.5.3 Gibbs energy and interfacial energy temperature dependency

The Gibbs energy difference at a temperature depends on the properties of the liquid and the solid for a given polymorph. The interfacial energy is δ, and the difference in chemical potential between the phases is $\Delta\mu$. For a pure material $\Delta\mu = \Delta G_{melting} = -\Delta G_{crystallization}$, which we call ΔG_s. ΔF is the Gibbs energy in the context of the "Gibbs-Thomson" equation:

$$\Delta F = 2 \cdot d_0(1 + r_a) \cdot \xi \cdot \delta - d_0 \cdot r_a \cdot \xi^2 \cdot \frac{\Delta G_s}{v_s} \qquad 4\text{-}10$$

Thus,

$$\Delta F = d_0(1 + r_a) \cdot (k_0)^{\frac{1}{2}} \cdot 2\delta \cdot i^{\frac{1}{2}} - \Delta G_s \cdot i \qquad 4\text{-}11$$

Examples of ΔF at different temperatures are given in the results section, in Figure 3-9(A). At the critical size ξ_c the derivative of the energy is zero, i.e., $d\Delta F/di = 0$. The critical number of molecules i^*, and the critical size ξ_c are:

$$i^* = \left[\frac{d_0(1 + r_a) \cdot \delta}{\Delta G_s}\right]^2 \cdot k_0 \qquad 4\text{-}12$$

$$i^* = \left[\frac{\delta}{\Delta G_s}\right]^2 \cdot k_{i^*};\ \ k_{i^*} = [d_0(1 + r_a)]^2 \cdot k_0 \qquad 4\text{-}13$$

$$\xi_c = (i^* \cdot k_0)^{\frac{1}{2}} \qquad 4\text{-}14$$

The critical size ξ_c depends on the polymorph, with $\xi_{c\alpha} > \xi_{c\beta'} > \xi_{c\beta}$. The dependency of critical size on temperature is illustrated later in the paper in Figure 3-9 (B). The energy at the critical size is:

$$\Delta F^* = d_0(1 + r_a) \cdot (k_0)^{\frac{1}{2}} \cdot 2\delta \cdot i^{*\frac{1}{2}} - \Delta G_s \cdot i^* \qquad 4\text{-}15$$

At the melting temperature ΔG_s is zero, and the size is infinite.

As explained in T&F, the free energy of an embryo of "i" molecules, ΔF_i, (see Figure 3-8) is often parametrized as:

$$\frac{\Delta F_i}{kT} = A \cdot i^{\frac{2}{3}} - B \cdot i \qquad 4\text{-}16$$

The coefficients A and B depend on the Gibbs energy for the critical nucleus with number of molecules i^* ("Gibbs-Thomson" equation) following T&F. The units of A are molecules $^{(-2/3)}$ and the units of B are molecules^{-1}.

At the maximum, where $i = i^*$, the derivative $d\Delta F/di$ must be zero. Hence

$$\frac{\Delta F^*}{kT} = \frac{\left(\frac{A}{3}\right)^3}{\left(\frac{B}{2}\right)^2} \; ; \; i^* = \left(\frac{2}{3}\frac{A}{B}\right)^3 \tag{4-17}$$

The coefficients A and B in T&F are therefore:

$$A = 3 \cdot \frac{\xi_c \cdot (d_0 + (\xi_c + d_0) \cdot r_a) \cdot 2 \cdot \delta - \xi_c^2 \cdot \frac{\Delta G_s}{k_0}}{kT(i^*)^{\frac{2}{3}}} \tag{4-18}$$

and for B:

$$B = \frac{2}{3}\frac{A}{(i^*)^{\frac{1}{3}}} \tag{4-19}$$

Since A>0, from its denominator we have the important relationship:

$$\delta > \frac{d_0}{2 \cdot v_s} \cdot \Delta G_s \tag{4-20}$$

for β' the value of $d_0/(2.v_s)$ is 1.474 molecules/nm^2.

The Gibbs energy of crystallization at deep undercooling temperature T for the bulk material is:

$$\Delta G_s = \frac{-1}{N_A} \cdot \left[-\Delta H_m \left(1 - \frac{T}{T_m}\right) + \int_{T_m}^{T} \Delta C_p dT - T \cdot \int_{T_m}^{T} \frac{\Delta C_p}{T} dT \right] \tag{4-21}$$

where:

$$\Delta C_p = C_p^s - C_p^l \tag{4-22}$$

The chemical potential ΔG_s is close to linear for ΔT<30, as seen later in Figure 4-12. The slope is k_{Gs}, thus:

$$\Delta G_s \approx k_{G_s} \cdot \Delta T \tag{4-23}$$

The value of k_{Gs} is 4.593×10^{-25} kJ/(molecule·K). ΔG_s is between 7.5 and 9×10^{-24} kJ/molecule for ΔT 13 to 20 (295 to 288 K). Thus, the interfacial energy δ must be larger than

11 to 14 $\times 10^{-24}$ kJ/nm^2. The interfacial energy δ cannot be just a fixed multiplier of ΔG_s because then values of i^* would not decrease with ΔT in Equation 4-12. However, $\delta/\ \Delta G_s$ must decrease with ΔT. Therefore, at ΔT=0 the value of δ cannot be zero. A simple first order approximation for δ:

$$\delta = \delta_m + \delta_T \cdot \Delta T \qquad 4\text{-}24$$

From Equation 4-20 the minimal value for the slope δ_T is $\approx 7 \times 10^{-25}$ kJ/(nm^2·K). The values of δ_m and δ_T were then found by fitting the model to the onset temperature data.

4.5.4 Energy barrier of activation

We propose that the exponential part of the T&F equation can be estimated by including the entropic component of the free energy of adding one molecule to an embryo. The process of adding a molecule is represented in Figure 4-5: A representation of free energy of activation and TAG molecules. Modified from T&F.[5] , inspired on T&F. The Gibbs energy of the initial and final embryos, as well as the activated state, are placed at their relative energetic level. As in T&F we used the average energy between the two embryos as the reference level. Hence,

$$\Delta F^x = \overline{\Delta F_i} + \Delta f^x = \frac{1}{2}(\Delta F_i + \Delta F_{1L} + \Delta F_{i+1}) + \Delta f^x \qquad 4\text{-}25$$

The activation energy that we propose is the entropy part of the Gibbs energy of incorporating a molecule to the embryo. Thus,

$$\Delta F^x = (\Delta F_i + \Delta F_{1L}) - T \cdot \Delta S^x \qquad 4\text{-}26$$

The energy of activation is, therefore,

$$\Delta f^x = \frac{\Delta F_i - \Delta F_{i+1} + \Delta F_{1L}}{2} - T \cdot \Delta S^x \quad 4\text{-}27$$

The entropy difference from the state embryo of "*i*" and a liquid molecule, to the activated state[136], is given by:

$$\Delta S^x = \frac{1}{N_A} \cdot \left[\int_{T_m}^{T} \frac{\Delta C_p}{T} dT - \frac{\Delta H_m}{T_m} \right] \quad 4\text{-}28$$

The modified T&F term, Δf^x, is then:

$$\Delta f^x = \frac{\Delta F_i - \Delta F_{i+1} + \Delta F_{1L}}{2} - \frac{T}{N_A} \cdot \left[\int_{T_m}^{T} \frac{\Delta C_p}{T} dT - \frac{\Delta H_m}{T_m} \right] \quad 4\text{-}29$$

The terms of Equation 4-29 are described by expressions from Equations 4-30 to 4-32.

The difference between ΔF_i and ΔF_{i+1} is:

$$\Delta F_i - \Delta F_{i+1} = \left(\left(i^{\frac{1}{2}} - (i+1)^{\frac{1}{2}} \right) \cdot k_1 - r_a \right) k_0 \cdot 2 \cdot \delta + \Delta G_s \quad 4\text{-}30$$

ΔG_s is found from Equation 4-21 , and δ is Equation4-24. The convenience constant, k_1, is:

$$k_1 = \frac{(1 + r_a) \cdot d_0}{(k_0)^{\frac{1}{2}}} \quad 4\text{-}31$$

The Gibbs energy of the liquid molecule is:

$$\Delta F_{1L} = \frac{1}{N_A} \cdot \left(\int_{T_m}^{T} C_p^l dT - T \cdot \int_{T_m}^{T} \frac{C_p^l}{T} dT \right) \quad 4\text{-}32$$

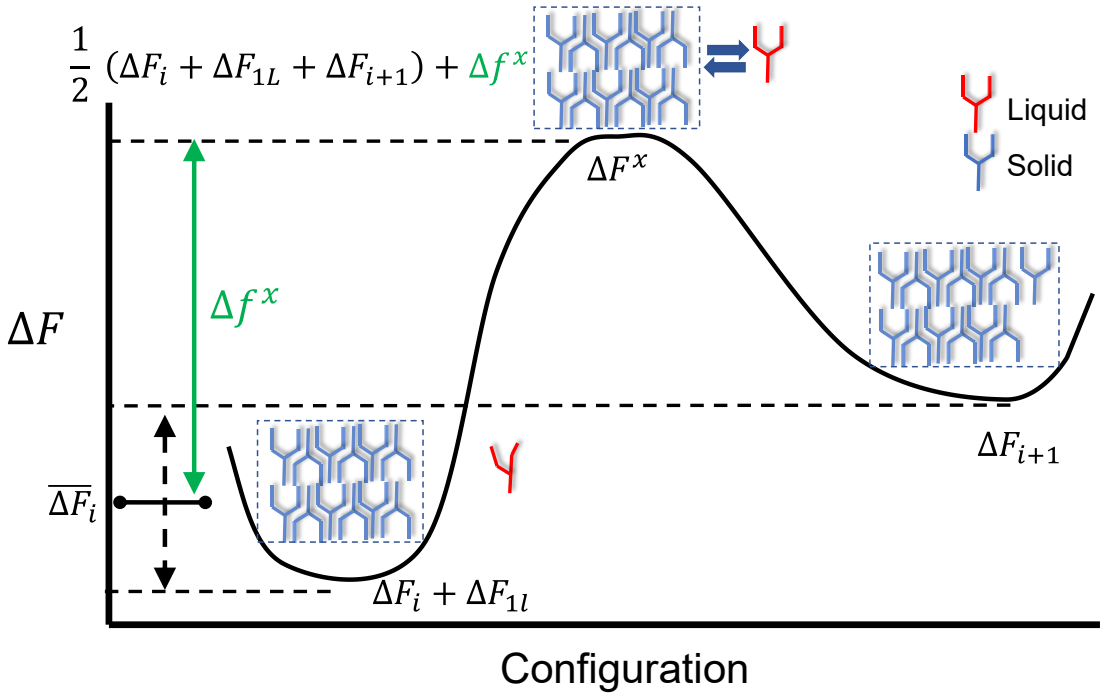

Figure 4-5: A representation of free energy of activation and TAG molecules. Modified from T&F.[5]

The actual value of the energy barrier, Δf^x, is likely lower than this estimate, as the Gibbs energy difference between a small embryo and the liquid (less organized than large bulk crystal) is lower than the difference of the bulk phase[119]. The T&F model corresponds to homogeneous primary nucleation. It is experimentally observed that the container affects the observable onset of nucleation, which indicates that heterogeneous nucleation is taking place. To establish a foundational understanding of nucleation phenomena, however, we initially adopt the model of homogeneous nucleation proposed by T&F. This approach enables us to isolate and understand the basic physical principles that govern nucleation while minimizing the complexities that arise from heterogeneous factors. Once this baseline model is established and validated, we can gradually introduce heterogeneity

into our model, adjusting and refining it as necessary. Additionally, we want to specify the nature of heterogeneity in the nucleation process within this chapter. Our focus is on concomitant crystallization, a phenomenon where one polymorphic form begins to crystallize on the surface of another. In other words, in our case, heterogeneity arises due to the later-crystallizing polymorph growing on the surface of the earlier one. Our proposal thus serves as a first approximation to nucleation and provides an important foundation for subsequent refinements.

4.5.5 Solving the parabolic partial differential equation

The partial differential equation (PDE) of Equation 4-1 is a parabolic PDE. Although challenging, it can be integrated numerically for each polymorph. The integral starts at the melting temperature of the polymorph and ends at the onset temperature of crystallization for that polymorph.

The onset temperature is always lower than the melting point of the β polymorph, otherwise there would be no crystallization whatsoever. Therefore, at all the onsets, there will be a value of the integral for nucleation rate that is larger than zero. The value, however, will be in many cases extremely small, since we did not observe crystallization of β. For onsets that happen below the melting point of β', the integral runs from the melting point of β' to the onset temperature.

The equation can be reorganized in a standard mode as:

$$\left[\left(\frac{i_s kT}{h}\right)\cdot i^{\frac{2}{3}}\cdot exp\left(\frac{-\Delta f^x}{kT}\right)\right]^{-1}\frac{\partial n_i}{\partial t} = -n_i\frac{2}{3}A\cdot\left(i^{-\frac{1}{3}} - i^{*-\frac{1}{3}}\right) - \frac{\partial n_i}{\partial i} \qquad 4\text{-}33$$

Since the changes in n_i are sudden and very large, it is more manageable to solve the

problem in its logarithmic space by substituting n_i with an exponential:

$$n_i = e^u \text{ and } \partial n_i = e^u \cdot \partial u \quad \text{4-34}$$

The equation can thus be cast as:

$$c(i,T(t))\frac{\partial u}{\partial t} = s(i,T(t)) - \frac{\partial u}{\partial i} \quad \text{4-35}$$

In this work we are interested in the onset of the nucleation event at a particular embryo size i^*. The event itself can be estimated from the trend of the 'catastrophic' increase in smaller sizes. The derivatives tend to an 'effective' infinity ∞_s, i.e., the maximum computational limit of the software:

$$u \to \infty_s; \frac{\partial u}{\partial t} \to \infty_s \; ; \; \frac{\partial u}{\partial i} \to \infty_s \quad \text{4-36}$$

We assume that the nucleation that produces embryos of the critical size to form at a fast rate coincides with the onset estimated from the DSC thermograms.

As the number of embryos n_i with $i<i^*$ increases, the region of (u,t,i) space within computational range becomes smaller. At the time when the software cannot integrate any further, the integration has often proceeded to about 60% of the time needed to reach critical size.

4.5.6 Solving the overall interfacial energy of the α polymorph on the surface of the β'

Our DSC and XRD data clearly demonstrate that the α polymorphs form following the crystallization of β' polymorphs. It is crucial that we address two often overlooked, yet highly relevant, concepts within lipid crystallization: cross-nucleation and concomitant polymorphism.[137] By thoroughly examining these phenomena, we can enhance our

understanding and contribute to the broader discussion within the lipid crystallization community. The key distinction between cross-nucleation and concomitant polymorphism lies in the processes through which they take place. Cross-nucleation involves the formation and growth of a new crystal on the surface of a distinct polymorph, whereas concomitant polymorphism refers to the concurrent crystallization of two or more polymorphs exhibiting similar nucleation rates. Cross-nucleation stems from the molecular mechanism that drives concomitant polymorphism, which primarily occurs due to the competing primary nucleation rates of different polymorphs. As such, cross-nucleation represents a specific instance of concomitant polymorphism, wherein one polymorph nucleates on another polymorph's surface, both belonging to the same compound. Cross-nucleation describes the secondary heterogeneous nucleation of a kinetically favorable polymorph on the surface of the kinetically less favorable one. [138] Secondary nucleation occur from pre-existing nuclei whereas primary nucleation results from the presence of foreign particles.[139]

For the heterogenous secondary nucleation, the interfacial energy, δ, is the weighted average for both polymorphs and is defined as:

$$\delta = \delta_{\alpha} \cdot x_t + \left(\delta_{\beta'} - \delta_{\alpha}\right)(1 - x_t) \qquad 4\text{-}37$$

and as discussed in the first paper, δ, is function of the undercooling ΔT (Equation 4-24) and can hence be formulated for each polymorph as follows:

$$\delta_{\alpha} = \delta_{m\alpha} + \delta_{T\alpha} \cdot \Delta T_{\alpha} \qquad 4\text{-}38$$

$$\delta_{\beta'} = \delta_{m\beta'} + \delta_{T\beta'} \cdot \Delta T_{\beta'} \quad 4\text{-}39$$

substituting equations 4-38 and 4-39 into the general equation of δ (Equation 4-24), it follows that:

$$\delta = \delta_{m\beta'} + \delta_{T\beta'} \cdot \Delta T_{\beta'} - x_t\left(\delta_{m\beta'} + \delta_{T\beta'} \cdot \Delta T_{\beta'} - \delta_{m\alpha} - \delta_{T\alpha} \cdot \Delta T_{\alpha}\right) \quad 4\text{-}40$$

with the overall slope and intercept formulated as follows:

$$\delta_T \cdot \Delta T_{\beta'} = \left[\delta_{T\beta'} - x_t\left(\delta_{T\beta'} - \delta_{T\alpha}\right)\right] \cdot \Delta T_{\beta'} \quad 4\text{-}41$$

$$\delta_m = \delta_{m\beta'} - x_t\left(\delta_{m\beta'} - \delta_{m\alpha} + \delta_{T\alpha} \cdot \Delta T_m\right) \quad 4\text{-}42$$

The values for $\delta_{T\beta'}$ and $\delta_{m\beta'}$ are known values obtained from the numerical calculations in the first part of this work[140], hence the unknow values of those for the α polymorphs are obtained as global fitting parameters, where:

$$\delta_{m\alpha} = \frac{\delta_m - \delta_{m\beta'} + x_t\left(\delta_{m\beta'} + \delta_{T\alpha} \cdot \Delta T_m\right)}{x_t} \quad 4\text{-}43$$

$$\delta_{T\alpha} = \frac{\delta_T - (1 - x_t)\delta_{T\beta'}}{x_t} \quad 4\text{-}44$$

4.6 EXPERIMENTAL PROCEDURES

4.6.1 Materials

Tridodecanoyl-glycerol (LLL, CAS 538-24-9) were purchased from Fluka (via Sigma-Aldrich Chemical Co) with a purity of > 99%.

4.6.2 DSC

A heat flux Q100 DSC with an integrated refrigerated cooling system, provided by TA Instruments, was employed to produce the crystallization curves. Raw signals were acquired using the available software. Calibration for the cell resistance, capacitance, constant, and temperature was accomplished in three stages: an initial check of an empty cell, a run with pure sapphire, followed by a run with pure indium. A flow of nitrogen gas at 25 mL/min was used to purge the sample cell. Hermetically sealed aluminum DSC pans held the samples, which weighed between 3 to 6 mg. An empty aluminum pan served as a reference. All samples underwent an initial heating process up to 353 K at a 10 K/min rate and then maintained at that temperature for 7 minutes to eradicate any effects of 'crystal memory'. Afterwards, they were cooled to 343 K utilizing nine different cooling rates (25, 20, 17.5, 15, 12.5, 10, 7.5, 5, and 2.5 K/min) applied in a randomized sequence. A total of 54 cycles of heating and cooling were implemented on each sample without removing it from the setup to minimize variability caused by pan positioning. The Universal Analysis software from TA Instruments was used to export the results to MS Excel, and further data processing was conducted using a method developed by our team in MATLAB.

4.6.3 X-ray diffraction

The experiments using synchrotron radiation XRD (SR-XRD) were carried out at the National Synchrotron Light Source (NSLS-I) at the Brookhaven National Laboratory in Upton, NY, USA. These experiments employed the synchrotron radiation source available at the Exxon Mobil X10A beamline. To capture diffraction patterns, a Bruker 1500 two-dimensional CCD detector was utilized, with each exposure lasting 5 seconds, followed by an additional 5 seconds for image reading and 'unwarping'. For the small-angle XRD experiments, a wavelength of λ=1.09468 Å was used, and the detector was positioned 1014.6 mm away from the capillary. The wide-angle XRD experiments, on the other hand, had the detector set up at 136.8 mm from the capillary. The energy calibration of the beam was done using aluminum oxide and silicon powders. The setup had an instrumental resolution of $0.0027 Å^{-1}$ with a beam size of 0.5 x 0.5 mm. Samples were placed into a thin glass capillary with a diameter of 1.5 mm, which was preheated to 343 K for 10 minutes prior to each experiment. After each experiment, the capillary was cooled down to 263 K at each rate and held there for five minutes. Subsequently, the capillary was reheated to 343 K at a steady rate of 5.0 K/min. Seven cooling rates were investigated: 20, 15, 10, 7.5, 5.0, 2.5, and 1.0 K/min. For data analysis, a custom plugin for ImageJ was used to compute the radial averages of the isotropic diffraction patterns and to normalize the intensities correctly. Finally, the one-dimensional diffraction profiles were fitted to a mixture of Gaussian and Lorentzian peak functions using a modified Levenberg-Marquardt algorithm in Igor Pro 9.

4.7 RESULTS AND DISCUSSION

4.7.1 DSC thermograms and XRD data

The cooling from the melt at different cooling rates produces different proportions between the β' and the α polymorphs. X-ray diffraction in capillaries at the end of crystallization in Figure 4-6 shows an example.

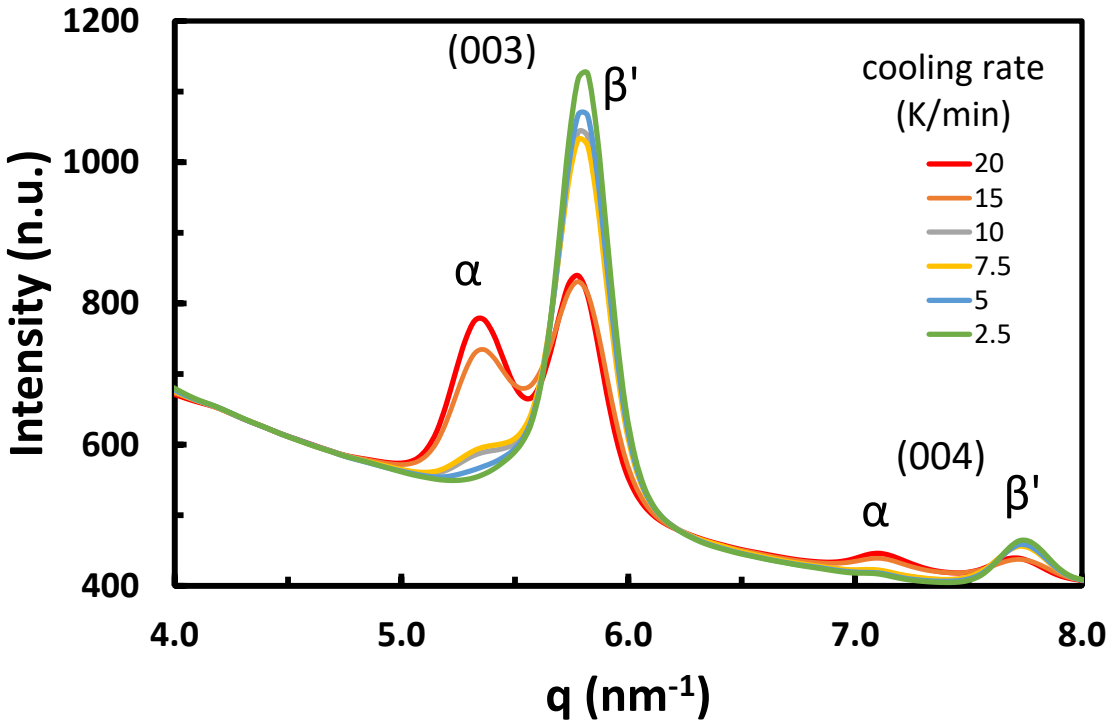

Figure 4-6: Small angle X-ray diffraction (SAXD) intensity for the (003) and (004) reflections, as function of scattering vector q (nm-1), of trilaurin at 253 K. Trilaurin was crystallized from the melt in a capillary using different cooling rates indicated with different colors.

The small angle scattering patterns shown in Figure 4-7 correspond to the 2L β' form of LLL. This was confirmed by the wide angle XRD patterns captured simultaneously (not shown). The first onset of crystallization corresponds to crystals of β'. As the cooling continues, a second onset of crystallization is observed, at a lower temperature. This corresponds to the α polymorph. The example in Figure 4-7 is representative of the other cooling rates as well. It shows the SAXD pattern of a LLL sample cooled at 20 K/min in a capillary. The scattering peak of the crystallization of the β' polymorph is seen at the onset temperature (at 290.9 K) along with its subsequent growth as cooling continued. X-ray scattering/diffraction intensity for the (003) reflection normalized to account for sample attenuation and incident X-ray beam intensity, as function of scattering vector q (nm^{-1}). An examination of Figure 4-6 and Figure 4-7 reveals that the β form did not crystallize under any of the explored cooling rates. This observation can be attributed to its relatively higher activation energy and surface tension values, despite the presence of significant undercooling.

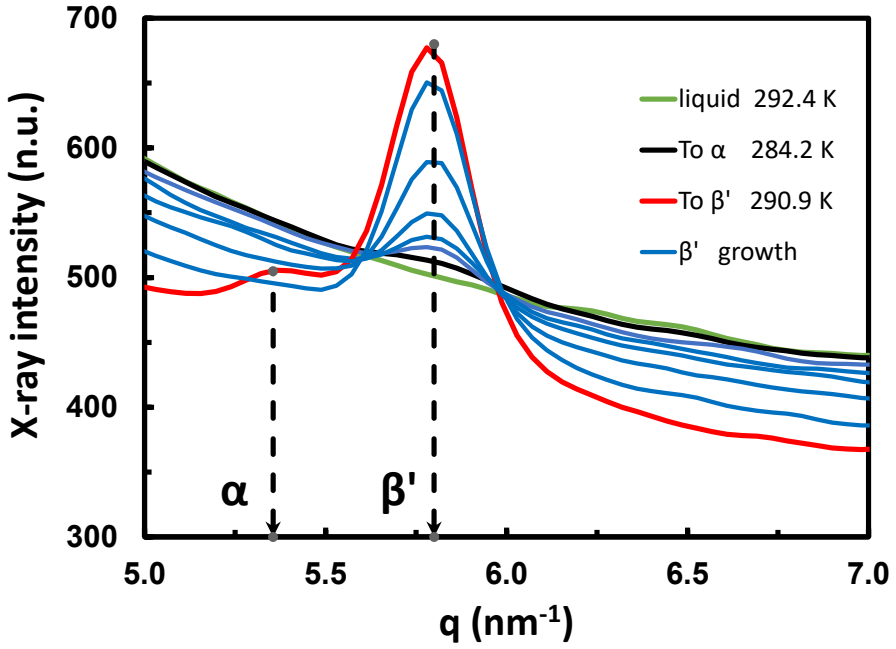

Figure 4-7: X-ray scattering/diffraction intensity for the (003) reflection, as function of scattering vector q (nm^{-1}). The trilaurin was cooled from the melt at 20 K/min in a capillary.

From the DSC thermograms, the first onset of crystallization was estimated from the change in slope in the heat flow signal. To estimate the second onset of crystallization from the liquid, the crystallization events were modeled with a modified the Kolmogorov[7]-Johnson and Mehl[8]-Avrami [9](JMAEK) equation. A modified Avrami function to identify peak signals and detect second onsets, which has the same expression as the probability density function of the Weibull distribution. Details on fitting procedures were done by a research colleague. [141] An example of a DSC thermogram of a LLL sample cooled at 10 K/min is presented in Figure 4-8 ; the second onset estimated from the fitting is also indicated.

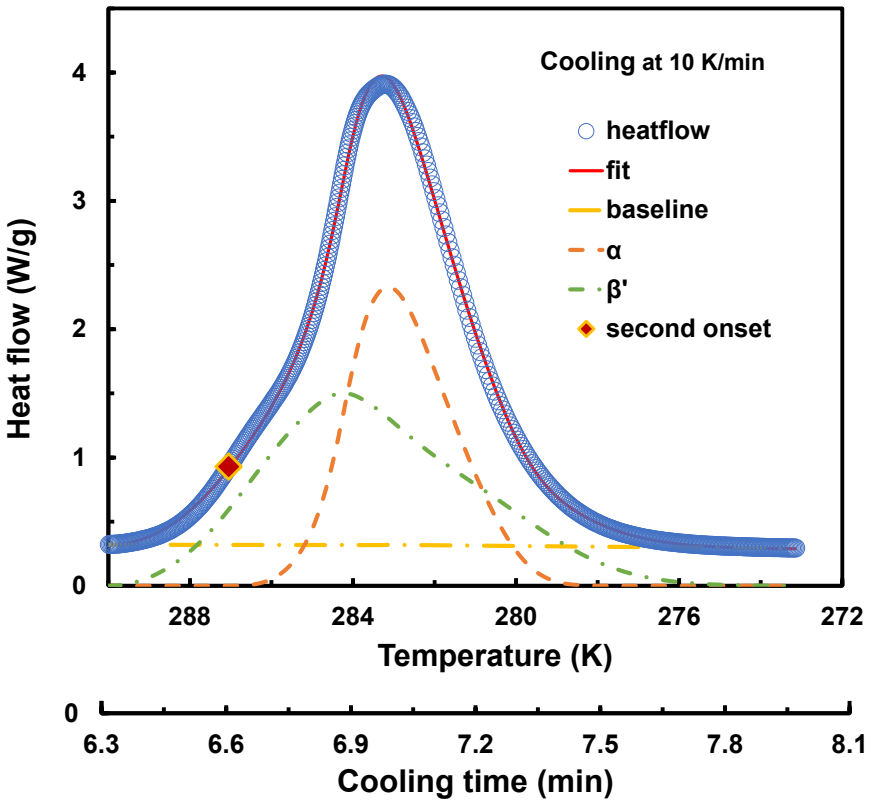

Figure 4-8: Heat flux per unit mass as a function of temperature and time, during the cooling in the DSC of LLL at 10 K/min, starting from the melt at 353 K.

The parameters of the functions can be estimated from their fit to the heat flow as a function of time. To use it as a function of time, we replace the experimental ΔT with the linear relationship provided by the cooling rate, C_R:

$$\Delta t = t - t_o \; and \;\; \Delta T = T_o - T \;\; with \, \Delta T = C_R \cdot \Delta t \qquad 4\text{-}45$$

The value of the characteristic time, b, in the JMAEK model is a constant. However, during non-isothermal crystallization its value is reduced due to the increase in undercooling as time goes by. In the model we have modified the characteristic time to be weak

function of temperature b - $b_1 \cdot C_R \cdot \Delta t$, with $b_1 \geq 0$. The crystalline fraction y_c is then:

$$y_c = 1 - exp[-(r_t{}^a)] \tag{4-46}$$

where:

$$r_t = \frac{C_R \cdot \Delta t}{b - c \cdot C_R \cdot \Delta t} \; and \; \Delta t = t - t_o \tag{4-47}$$

The derivative function with respect to Δt is then:

$$y_{Dt} = \frac{C_R \cdot a \, r_t{}^{a-1}}{b - c \cdot C_R \cdot \Delta t}(1 + c \cdot \, r_t) \cdot exp[-(r_t{}^a)] \tag{4-48}$$

There are eight fitting parameters: a, b, c for the β' polymorph and a, b, c, and $T_{o\alpha}$ for the α polymorph. A fitting program was written using MATLAB. The onset temperatures for the α and β' polymorphs obtained at different cooling rates are presented in Figure 4-9.

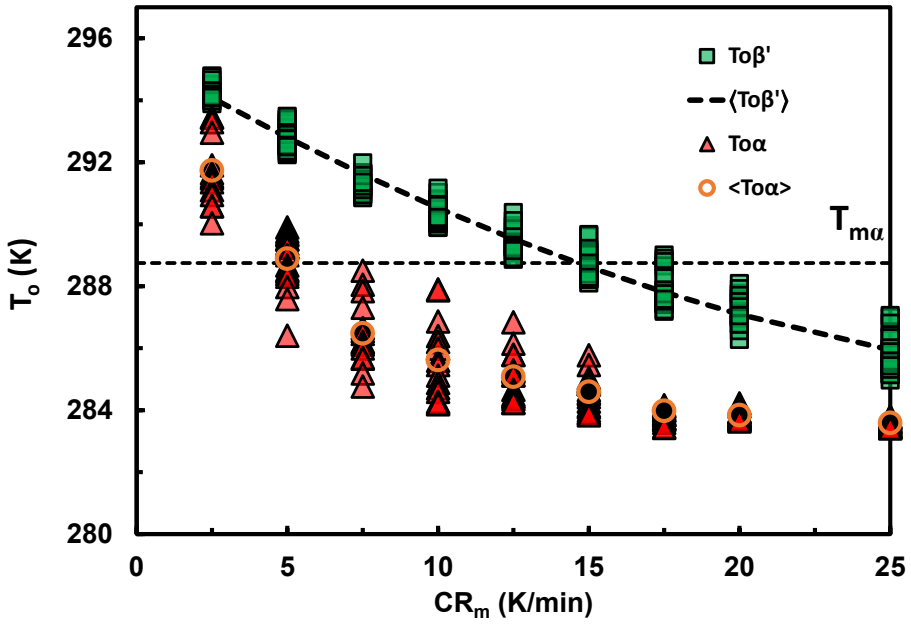

Figure 4-9: Onset temperature of crystallization as a function of cooling rate for the β' phase and for the subsequent α phase. The literature value of the melting temperature for the α phase is indicated.

As has been reported[123] experiments done in different sample containers (DSC pans, microscope slides, glass capillaries, etc.) provide a different range of estimated onset temperatures. This is due to different surfaces and different heat transfer geometries and rates. Nonetheless, the melting thermograms confirmed as well the initial formation of phase β', which is consistent with other literature sources. [142] At lower cooling rates the formation of β' was similarly observed.

4.7.2 Nucleation of the α phase

The PDE was solved with an initial estimate of the interfacial energy parameters δ_m and δ_T in Equation 4-24, that were refined afterwards. The slope parameter δ_T was replaced by a more tangible value, δ_{23}, which is the value expected at the deepest practical undercooling, *i.e.,* $\Delta T \approx 23$ K. The slope δ_T is thus,

$$\delta_T = \frac{\delta_{23} - \delta_m}{23} \qquad 4\text{-}49$$

An example of the time-temperature evolution of $\log(n_i)$ is shown in Figure 4-10, further transformed by logarithmic coordinates. Due to the numerical limit of the computations, the integration stopped before the 'catastrophic' front of growth of the number of embryos of each family reached the critical nucleation size i^*. It was observed that the front followed a smooth path as function of time t_u and the $\log(i/i^*)$.

The advance of this edge was used to estimate the actual time t_{uf} needed to reach $i/i^*=1$, as shown in Figure 4-10. The extrapolation was done with the three-term power law in Equation 4-50and illustrated in Figure 4-11(A):

$$t_{uf} = b_0 + b_1 \cdot \left({}^{i}/_{i^*}\right)^{b_2} \qquad 4\text{-}50$$

A search algorithm was coded in MATLAB to find the values of δ_m and δ_{23} that minimized the sum of squared errors with respect to the observed onset times, t_r. The time t_r for a cooling rate c_r (K/s), is:

$$t_r = \frac{T_m - T_o}{c_r} \qquad 4\text{-}51$$

The search was done with the set of temperatures at the average, and within two standard deviations from the average (95% confidence interval). The red line in Figure 4-10 shows the front of catastrophic increase in embryo numbers during cooling at 15 K/min.

The front was extrapolated from the point where the calculation stopped due to overflow.

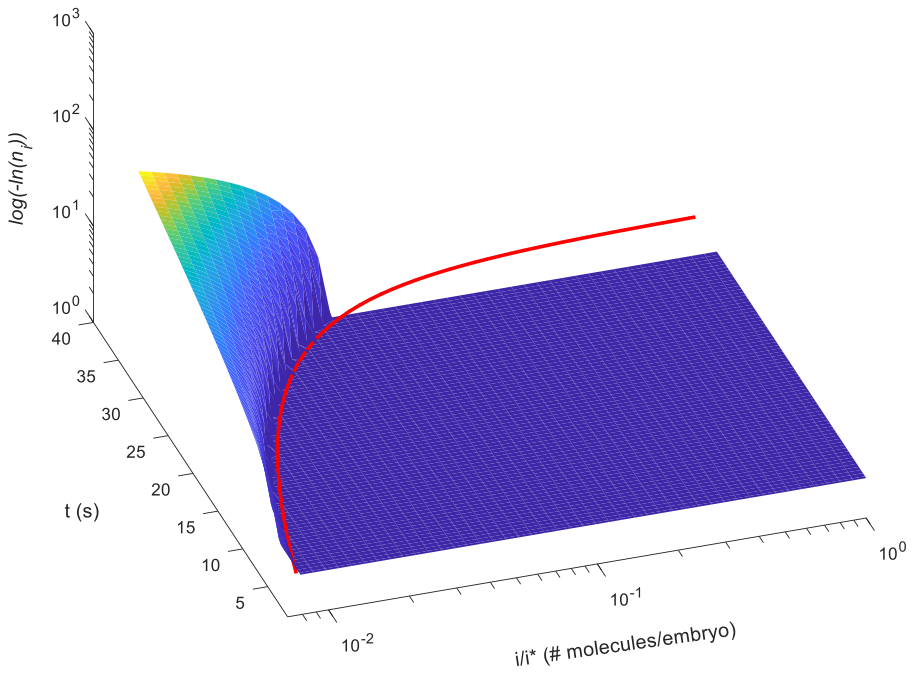

Figure 4-10. Double logarithm of the number of α embryos of a class, n_i, as a function of time t_{uf} and the ratio i/i^*, during cooling at 15 K/min to T_o 284.6 K. Cooling time t_r = 34.4 s. The critical embryo size was i^* = 284 molecules. The red line is the front curve.

The extrapolation was done with the three-term power law used for the quasi-isothermal analysis, Equation 4-50. The fronts and the extrapolation curves for the six cooling rates are shown in Figure 4-11.

The extrapolated values were converted to estimated real times t_{rf} using Equation 4-50 , and then the relative error ϵ_t was calculated:

$$\epsilon_t = \frac{t_r - t_{rf}}{t_r} \tag{1}$$

A similar procedure was followed for the temperatures at the 95% confidence interval limits (see Table 4-2). The errors were less than 1%.

Table 4-2: Parameters for interfacial energy estimation

	95%-	Average	95%+
$\delta_{m\alpha} \times 10^{-24}$ kJ/nm^2	0.05	0.1	N.A.
$\delta_{T\alpha} \times 10^{-24}$ kJ/(K·nm^2)	1.735	2.170	N.A.

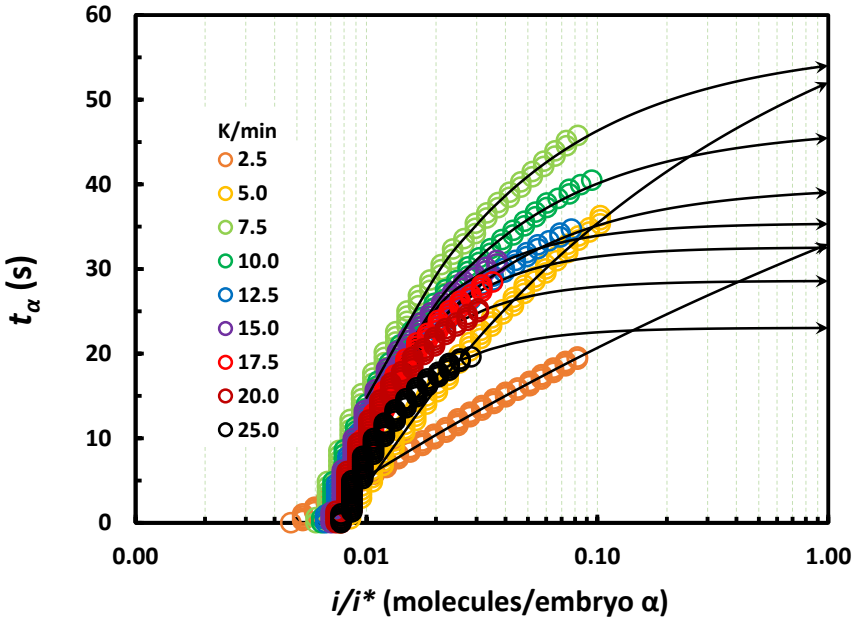

Figure 4-11: Processing time as a function of *i/i** for three cooling rates. The lines show the extrapolation to find the end t_{uf}.

The calculated interfacial energy δ for both polymorphs is plotted in Figure 4-12 as a function of the undercooling $\Delta T_{\beta'}$ with respect to the melting point of β'. The chemical potential values ΔG_s for both polymorphs are plotted as well.

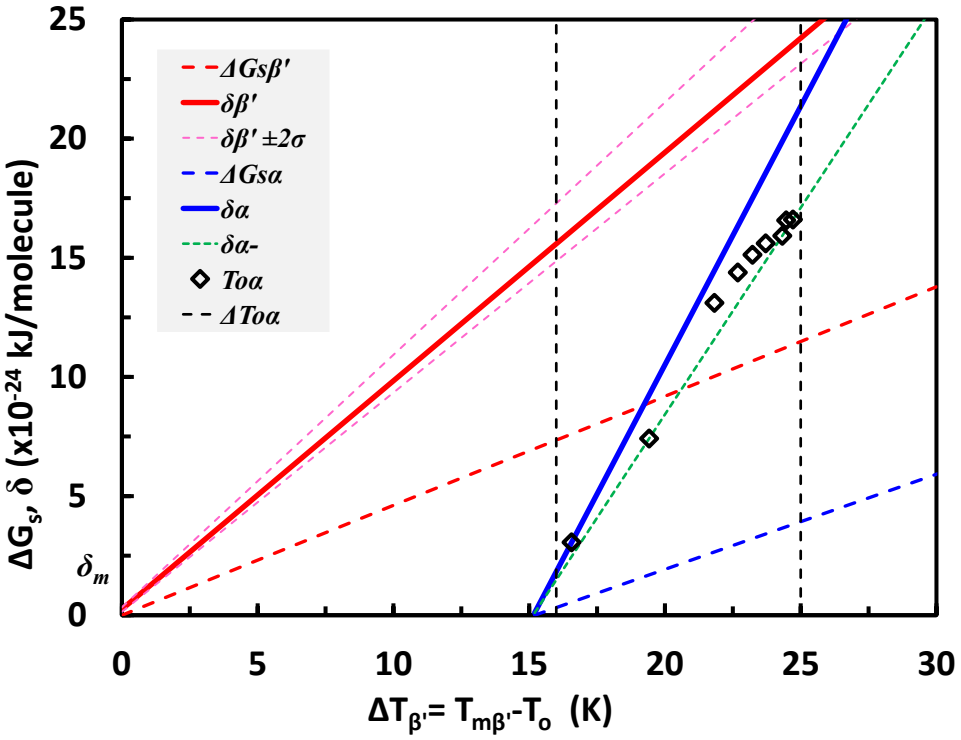

Figure 4-12: Solid-Liquid chemical potential ΔG_s, and interfacial energy δ, as a function of undercooling $\Delta T_{\beta'}$. (Cf. Eq. 4-24)).

These interfacial energy and chemical potential determine the Gibbs energy ΔF as a function of temperature and number of molecules in the embryo, following Equation 4-15. If the interfacial energy δ was constant, the ΔF and ΔF^* values would increase as the temperature increases. The interfacial energy, however, decreases with temperature. Therefore, the ΔF and ΔF^* values decrease with increasing temperature, as seen in Figure 4-13 (A). The position of the maxima, i^*, computed with Equation 4-16 decrease slightly with increase in undercooling ΔT. For any pure liquid, as the undercooling increases, the critical nucleus formation size, i^*, is reduced. The increase of interfacial energy with undercooling softens this reduction. Thus, the calculated critical size i^* seen in Figure 4-13(B) changes much less than the i^* values calculated from a constant δ. Therefore, it takes

longer to reach the nucleation condition of $i=i^*$when δ increases with ΔT. The nucleus size ξ^* corresponding to $i^* \sim 45$ molecules is around 2.8 nm, with ξ_2^* 5.9 nm.

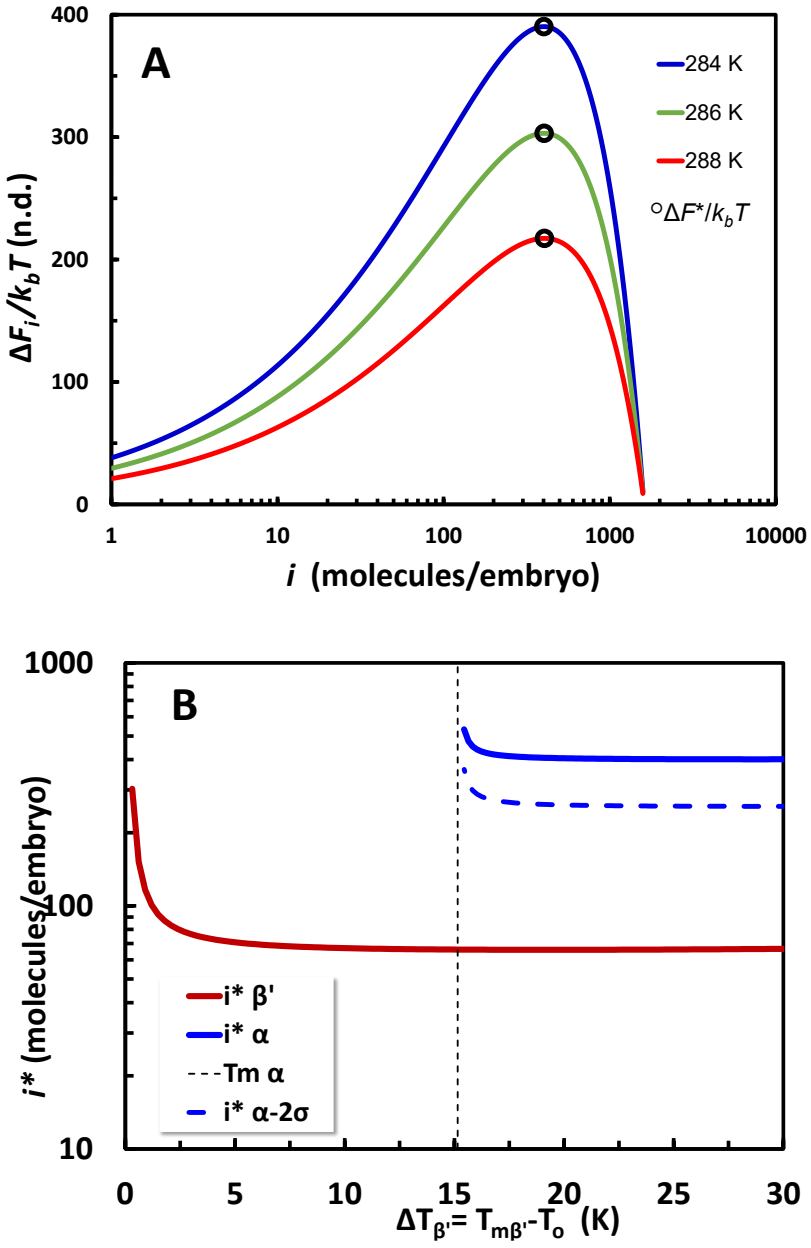

Figure 4-13: (A) Free energy of embryos and nuclei as a function of the number of molecules in a platelet, for the β' polymorph, at three temperatures, see Eq 4-16. (B) Number of molecules per embryo (molecules/embryo) at the critical nucleus size, i^*, as a function of undercooling ΔT (K) with its 95% confidence interval.

4.8 CONCLUSIONS

In conclusion, the non-isothermal cooling of triacylglycerols (TAGs) below the melting temperatures of its polymorphs instigates a complex sequence of transformations, substantially impacting the nucleation rates and crystalline structures. Understanding these transformations, regulated by the interplay between interface energy and chemical potential, is pivotal, with Gibbs free energy, ΔF, serving as a central driver.

We employed a differential form of the T&F model to find the nucleation rate of the β' polymorphs and the subsequent formation of the α form through cross-nucleation. The α form was molded considering it as a secondary heterogeneous nucleation by introducing a factor that accounts for the surface area exposed to the liquid. We provided an explanation as to why α polymorph formed after the crystallization and growth of β' based on calculated values of interfacial energy. The interfacial energy was approximated as $\delta = [0.10+ 2.17\cdot(T_m-T)]\times10^{-24}$ kJ/nm^2.

4.9 AUTHOR INFORMATION

Corresponding Author

* Gianfranco Mazzanti, mazzanti@dal.ca, Department of Process Engineering & Applied Science, Faculty of Engineering - Dalhousie University, Room F2215- 5273 DaCosta Row, Halifax, NS, Canada B3H 4R2.

4.10 AUTHOR CONTRIBUTIONS

The manuscript was written through significant contributions of all authors. All authors have given approval to the final version of the manuscript.

4.11 ACKNOWLEDGMENT

We appreciate the technical support of Steve Bennett at NSLS, and of Pavan K. Batchu for XRD work. Canada NSERC Discovery Grant.

CHAPTER 5 CONCLUSIONS AND FUTURE WORK

In this thesis, we explored the nucleation kinetics of TAGs during the crystallization process. Our primary goal was to understand and implement how to predict the polymorph(s) formed and at what temperature they will form when a liquid TAG is cooled at a controlled cooling rate. This is important for various industries, such as food, cosmetics, and pharmaceuticals as it will provide them with the predictive tool to optimize the crystallization conditions and enhance the properties of TAG-based products.

In Chapter 2, we discussed the importance of accurate measurements of specific heat capacity for lipids as a function of temperature, C_p(T), using DSC to model their crystallization behavior. We evaluated the uncertainties in C_p(T) measurements due to the pan position on a heat-flux DSC sensor.

In Chapter 3, we presented a conceptual and numerical method to solve the T&F nucleation model for a molecular liquid during its undercooling. We introduced the monolayer nanoplatelet embryo idea and proposed an interfacial energy and an energy of activation that are temperature and size dependent. We developed a numerical framework to solve the T&F nucleation model, which can be used to predict the onset temperature of nucleation at given cooling rates. The parabolic partial differential equation was solved algebraically and programmed to be solved numerically with MATLAB, making this model accessible to many researchers.

In Chapter 4, we extended our investigation on modeling the nucleation rate for α polymorph, and provided an explanation as to why they formed after the crystallization and growth of β' based on calculated values of interfacial energy. The interfacial energy was approximated as $\delta = [0.10+ 2.17\cdot(T_m\text{-}T)] \times 10^{-24}$ kJ/nm^2.

To better reflect real-world conditions, future work will focus on improving the models presented in this thesis by accounting for heterogeneous (primary) nucleation, which can have a significant impact on how nucleation occurs. To expand our understanding of TAGs nucleation, further studies can be conducted to investigate how parameters like energy of activation, interfacial energy, and critical size are affected by the carbon number in other TAGs.

An important aspect that needs to be addressed in future work is the potential influence of the pan position on heat capacity measurements. This issue can be resolved by utilizing DSCs equipped with a robotic arm for precise pan placement and ensuring consistency in the type of the pan used and pan-to-pan variability. Additionally, it would be advantageous to perform similar experiments in facilities that support simultaneous synchrotron X-ray diffraction (SXRD) and DSC measurements. This approach will help minimize measurement discrepancies resulting from variations in sample container types, thus improving the reliability and consistency of the results.

In our future work, we plan to enhance the versatility and precision of our model. An important future step is to adapt the model to handle TAGs with different carbon numbers and diverse types of saturated and unsaturated fatty acids. This would allow the model to represent a wider range of lipid systems, making it more widely applicable and facilitating a broader understanding of nucleation in different contexts. We also intend to incorporate three distinct values of δ values into the 3D monolayer nanoplatelet model, rather than a single averaged value. This would enable us to better capture the complex energy dynamics associated with the incorporation of TAG molecules onto the surface of nuclei, ultimately enhancing the model's predictive accuracy.

REFERENCES

1. Bohm, J., *The history of crystal growth.* Acta Physica Hungarica, 1985. **57**(3): p. 161-178.
2. Gibbs, J.W., *On the equilibrium of heterogeneous substances.* Transactions of the Connecticut Academy, 1878. **3**: p. 343-524.
3. Volmer, M. and A.Z. Weber, *Nucleus Formation in Supersaturated Systems.* Zeitschrift für Physikalische Chemie, 1926. **119**: p. 277-301.
4. Becker, R. and W. Döring, *Kinetic treatment of the nucleation in supersaturated vapors*. 1954: National Advisory Commitee for Aeronautics.
5. Turnbull, D. and J.C. Fisher, *Rate of Nucleation in Condensed Systems.* Journal of Chemical Physics, 1949. **17**(1): p. 71-73.
6. Hollomon, J. and D. Turnbull, *Nucleation.* Progress in Metal Physics, 1953. **4**: p. 333-388.
7. Kolmogorov, A.N., *On the Statistical Theory of Crystallization of Metals [in Russian].* Izv. Akad. Nauk SSSR, Ser. Mat., 1937. **3**: p. 355-359.
8. William, J. and R. Mehl, *Reaction kinetics in processes of nucleation and growth.* Trans. Metall. Soc. AIME, 1939. **135**: p. 416-442.
9. Avrami, M., *Kinetics of phase change I - General theory.* Journal of Chemical Physics, 1939. **7**(12): p. 1103-1112.
10. Sosso, G.C., et al., *Crystal Nucleation in Liquids: Open Questions and Future Challenges in Molecular Dynamics Simulations.* Chem Rev, 2016. **116**(12): p. 7078-116.
11. Wille, R. and E. Lutton, *Polymorphism of cocoa butter.* Journal of the American Oil Chemists' Society, 1966. **43**(8): p. 491-496.
12. Bailey, A.E. and D. Swern, *Bailey's Industrial Oil and Fat Products*. 1964: Interscience Publishers.
13. Nascimento, M.L.F., et al., *Dynamic processes in a silicate liquid from above melting to below the glass transition.* The Journal of chemical physics, 2011. **135**(19): p. 194703.

14. Gupta, P.K., D.R. Cassar, and E.D. Zanotto, *Role of dynamic heterogeneities in crystal nucleation kinetics in an oxide supercooled liquid.* The Journal of Chemical Physics, 2016. **145**(21): p. 211920.
15. Anantharaman, T.R. and C. Suryanarayana, *Review: A decade of quenching from the melt.* Journal of Materials Science, 1971. **6**(8): p. 1111-1135.
16. Marangoni, A.G., *Crystallization Kinetics*, in *Fat crystal networks*, A.G. Marangoni, Editor. 2004, Marcel Dekker: New York. p. 21-82.
17. Himawan, C., V.M. Starov, and A.G.F. Stapley, *Thermodynamic and kinetic aspects of fat crystallization.* Advances in Colloid and Interface Science, 2006. **122**(1-3): p. 3-33.
18. Acevedo, N.C. and A.G. Marangoni, *Characterization of the Nanoscale in Triacylglycerol Crystal Networks.* Crystal Growth & Design, 2010. **10**(8): p. 3327-3333.
19. Ostwald, W., *Studien über die Bildung und Umwandlung fester Körper.* 1. Abhandlung: Übersättigung und Überkaltung, 1897. **22U**(1): p. 289-330.
20. Threlfall, T., *Structural and Thermodynamic Explanations of Ostwald's Rule.* Organic Process Research & Development, 2003. **7**(6): p. 1017-1027.
21. Bernstein, J., R.J. Davey, and J.-O. Henck, *Concomitant Polymorphs.* Angewandte Chemie International Edition, 1999. **38**(23): p. 3440-3461.
22. Marangoni, A.G., *On the use and misuse of the avrami equation in characterization of the kinetics of fat crystallization.* Journal of the American Oil Chemists Society, 1998. **75**(10): p. 1465-1467.
23. Christian, J.W., *The Theory of Transformations in Metals and Alloys*. 2002: Elsevier Science.
24. Jeziorny, A., *Parameters characterizing the kinetics of the non-isothermal crystallization of poly(ethylene terephthalate) determined by d.s.c.* Polymer, 1978. **19**(10): p. 1142-1144.
25. Ozawa, T., *Kinetics of non-isothermal crystallization.* Polymer, 1971. **12**(3): p. 150-158.

26. Harnisch, K. and H. Muschik, *Determination of the Avrami exponent of partially crystallized polymers by DSC- (DTA-) analyses.* Colloid & Polymer Science, 1983. **261**(11): p. 908-913.
27. Vyazovkin, S. and N. Sbirrazzuoli, *Isoconversional approach to evaluating the Hoffman-Lauritzen parameters (U* and Kg) from the overall rates of nonisothermal crystallization.* Macromolecular Rapid Communications, 2004. **25**(6): p. 733-738.
28. Liu, T., Z. Mo, and H. Zhang, *Nonisothermal crystallization behavior of a novel poly(aryl ether ketone): PEDEKmK.* Journal of Applied Polymer Science, 1998. **67**(5): p. 815-821.
29. Cazé, C., et al., *A new method to determine the Avrami exponent by d.s.c. studies of non-isothermal crystallization from the molten state.* Polymer, 1997. **38**(3): p. 497-502.
30. Malek, J., *Kinetic analysis of crystallization processes in amorphous materials.* Thermochimica Acta, 2000. **355**(1-2): p. 239-253.
31. Zhang, Z., et al., *Kinetics of non-isothermal cold crystallization of uniaxially oriented poly(ethylene terephthalate).* Polymer, 2003. **44**(8): p. 2547-2551.
32. Achilias, D.S., G.Z. Papageorgiou, and G.P. Karayannidis, *Isothermal and nonisothermal crystallization kinetics of poly (propylene terephthalate).* Journal of Polymer Science Part B: Polymer Physics, 2004. **42**(20): p. 3775-3796.
33. Boistelle, R., *Fundamentals of nucleation and crystal growth*, in *Crystallization and Polymorphism of Fats and Fatty Acids*, N. Garti and K. Sato, Editors. 1988, Marcel Dekker: New York.
34. Timme, R.E., *Crystallisation of fats*, in *Developments in Oils and Fats*, R.J. Hamilton, Editor. 1995, Chapman & Hall: Glasgow, U.K. p. 204-223.
35. Himawan, C., V.M. Starov, and A.G. Stapley, *Thermodynamic and kinetic aspects of fat crystallization.* Adv Colloid Interface Sci, 2006. **122**(1-3): p. 3-33.
36. Anom, E.Y., *Comparison of the theoretical and experimental composition of crystallizing lipid mixtures*, in *Food Science*. 2009, Dalhousie University: Halifax. p. 269.

37. Pavan, K.B., *Kinetic distortion to thermodynamic predictions in crystallizing triglycerides*, in *Food Science* 2014, Dalhousie University: Halifax.
38. Willmott, P., *An introduction to synchrotron radiation: techniques and applications*. 2019: John Wiley & Sons.
39. Bragg, W.H. and W.L. Bragg, *The reflection of X-rays by crystals.* Proceedings of the Royal Society of London. Series A, Containing Papers of a Mathematical and Physical Character, 1913. **88**(605): p. 428-438.
40. Britannica, E. *Bragg law*. 2022 [cited 2023 10/July/2023].
41. Santos, J.C.O., et al., *Comparative study of specific heat capacities of some vegetable oils obtained by DSC and microwave oven.* Journal of Thermal Analysis and Calorimetry, 2005. **79**(2): p. 283-287.
42. Narvaez, P.C., et al., *Determination of some physical and transport properties of palm oil and of its methyl esters.* Latin American Applied Research, 2008. **38**(1): p. 1-6.
43. Morad, N., et al., *Liquid specific heat capacity estimation for fatty acids, triacylglycerols, and vegetable oils based on their fatty acid composition.* JAOCS, Journal of the American Oil Chemists' Society, 2000. **77**: p. 1001-1005.
44. Morad, N.A., M. Idrees, and A.A. Hasan, *Specific heat capacities of pure triglycerides by heat-flux differential scanning calorimetry.* Journal of Thermal Analysis, 1995. **45**(6): p. 1449-1461.
45. Los, J. and M. Matovic, *Effective kinetic phase diagrams.* J. Phys. Chem. B, 2005. **109**: p. 14632-14641.
46. Hampson, J.W. and H.L. Rothbart, *Triglyceride Specific-Heat Determined by Differential Scanning Calorimetry.* Journal of the American Oil Chemists Society, 1983. **60**(6): p. 1102-1104.
47. van Miltenburg, J.C. and P.J. van Ekeren, *Investigation of the thermal behavior of trielaidin between 10 K and 360 K.* Journal of Chemical and Engineering Data, 2003. **48**(5): p. 1245-1250.
48. Simpson, T.D., D.P. Hockett, and L. Harris, *Specific-Heats of the Solid-State Phases of Trimargarin and Tristearin.* Journal of the American Oil Chemists Society, 1984. **61**(5): p. 883-886.

49. Kowalski, B., *Determination of Specific-Heats of Some Edible Oils and Fats by Differential Scanning Calorimetry.* Journal of Thermal Analysis, 1988. **34**(5-6): p. 1321-1326.
50. Fasina, O.O. and Z. Colley, *Viscosity and Specific Heat of Vegetable Oils as a Function of Temperature: 35C to 180C.* International Journal of Food Properties, 2008. **11**(4): p. 738-746.
51. Eiteman, M.A. and J.W. Goodrum, *Heat-Capacity of the Triglycerides - Tricaproin, Tricaprylin and Tricaprin.* Journal of the American Oil Chemists Society, 1994. **71**(5): p. 549-550.
52. Samyn, P., et al., *Quality of Brazilian vegetable oils evaluated by (modulated) differential scanning calorimetry.* Journal of Thermal Analysis and Calorimetry, 2012. **110**(3): p. 1353-1365.
53. Phillips, J.C. and M.M. Mattamal, *Correlation of Liquid Heat-Capacities for Carboxylic Esters.* Journal of Chemical and Engineering Data, 1976. **21**(2): p. 228-232.
54. Charbonnet, G.H. and W.S. Singleton, *Thermal Properties of Fats and Oils .6. Heat Capacity, Heats of Fusion and Transition, and Entropy of Trilaurin, Trimyristin, Tripalmitin, and Tristearin.* Journal of the American Oil Chemists Society, 1947. **24**(5): p. 140-142.
55. Morad, N.A., et al., *Liquid specific heat capacity estimation for fatty acids, triacylglycerols, and vegetable oils based on their fatty acid composition.* Journal of the American Oil Chemists Society, 2000. **77**(9): p. 1001-1005.
56. Wang, F. and G. Mazzanti, *Viscous Heating in a Mini-Couette Cell Used in Rheo-XRD and Rheo-NMR Research*, in *American Oil Chemists Society*. 2012: Long Beach, USA.
57. Wang, T. and J.L. Briggs, *Rheological and thermal properties of soybean oils with modified FA compositions.* Journal of the American Oil Chemists Society, 2002. **79**(8): p. 831-836.
58. Morad, N.A., M. Idrees, and A.A. Hasan, *Improved Conditions for Measurement of the Specific-Heat Capacities of Pure Triglycerides by Differential Scanning Calorimetry.* Journal of Thermal Analysis, 1995. **44**(4): p. 823-835.

59. Schick, C., *Differential scanning calorimetry (DSC) of semicrystalline polymers.* Analytical and Bioanalytical Chemistry, 2009. **395**(6): p. 1589-1611.
60. Hill, V.L., D.Q.M. Craig, and L.C. Feely, *The effects of experimental parameters and calibration on MTDSC data.* International Journal of Pharmaceutics, 1999. **192**(1): p. 21-32.
61. Luisi, M., B. Wilthan, and G. Pottlacher, *Influence of purge gas and spacers on uncertainty of high-temperature heat flux DSC measurements.* Journal of Thermal Analysis and Calorimetry, 2015. **119**(3): p. 2329-2334.
62. Höhne, G.W.H. and E. Gloggler, *Some Peculiarities of the Dsc-2/Dsc-7 (Perkin-Elmer) and Their Influence on Accuracy and Precision of the Measurements.* Thermochimica Acta, 1989. **151**: p. 295-304.
63. Pishchur, D. and V. Drebushchak, *Recommendations on DSC calibration.* Journal of Thermal Analysis and Calorimetry, 2016. **124**(2): p. 951-958.
64. Hatta, I. and A.A. Minakov, *Some remarks on heat capacity measurements by temperature-modulated calorimetry.* Thermochimica Acta, 1999. **330**(1-2): p. 39-44.
65. Xu, S.X., Y. Li, and Y.P. Feng, *Some elements in specific heat capacity measurement and numerical simulation of temperature modulated DSC (TMDSC) with R/C network.* Thermochimica Acta, 2000. **360**(2): p. 157-168.
66. VarmaNair, M. and B. Wunderlich, *Non isothermal heat capacities and chemical reactions using a modulated DSC.* Journal of Thermal Analysis, 1996. **46**(3-4): p. 879-892.
67. Sarge, S.M. and W. Poessnecker, *The influence of heat resistances and heat transfers on the uncertainty of heat-capacity measurements by means of differential scanning calorimetry (DSC).* Thermochimica Acta, 1999. **329**(1): p. 17-21.
68. Verdonck, E., K. Schaap, and L.C. Thomas, *A discussion of the principles and applications of Modulated Temperature DSC (MTDSC).* International Journal of Pharmaceutics, 1999. **192**(1): p. 3-20.

69. Cao, J.N., *Numerical simulation of DSC and TMDSC curves as well as reversing and nonreversing curve separation.* Journal of Applied Polymer Science, 2007. **106**(5): p. 3063-3069.
70. Wunderlich, B., Y.M. Jin, and A. Boller, *Mathematical-Description of Differential Scanning Calorimetry Based on Periodic Temperature Modulation.* Thermochimica Acta, 1994. **238**: p. 277-293.
71. Rudtsch, S., *Uncertainty of heat capacity measurements with differential scanning calorimeters.* Thermochimica Acta, 2002. **382**(1-2): p. 17-25.
72. Richardson, M.J., *Quantitative aspects of differential scanning calorimetry.* Thermochimica Acta, 1997. **300**(1-2): p. 15-28.
73. Merzlyakov, M. and C. Schick, *Complex heat capacity measurements by TMDSC. Part 2. Algorithm for amplitude and phase angle correction.* Thermochimica Acta, 1999. **330**(1-2): p. 65-73.
74. Höhne, G.W.H., W.F. Hemminger, and H. Flammersheim, *Differential Scanning Calorimetry*. 2 ed. 2003, Heidelberg: Springer.
75. Danley, R.L., *New heat flux DSC measurement technique.* Thermochimica Acta, 2003. **395**(1-2): p. 201-208.
76. Danley, R.L., *DIFFERENTIAL SCANNING CALORIMETER*, U.S. Patents, Editor. 2002, TA Instruments-Waters, LLC, New Castle, DE: US.
77. ASTM-International, *Standard test method for determining specific heat capacity by differential scanning calorimetry*. 2005: West Conshohocken, PA.
78. Ditmars, D.A., et al., *Enthalpy and Heat-Capacity Standard Reference Material - Synthetic Sapphire (Alpha-Al2o3) from 10 to 2250 K.* Journal of Research of the National Bureau of Standards, 1982. **87**(2): p. 159-163.
79. Diedrichs, A. and J. Gmehling, *Measurement of heat capacities of ionic liquids by differential scanning calorimetry.* Fluid Phase Equilibria, 2006. **244**(1): p. 68-77.
80. Hesse, N., *Heat Capacity Determination at High Temperatures by Using Simultaneous DSC-TGA*. 2010, TA Instruments: New Castle.
81. 100, J.J., *Evaluation of measurement data - Guide to the expression of uncertainty in measurement.* Joint Committee for Guides in Metrology, 2008.

82. Wilthan, B., *Uncertainty budget for high temperature heat flux DSCs.* Journal of Thermal Analysis and Calorimetry, 2014. **118**(2): p. 603-611.
83. Claudy, P., J.C. Commercon, and J.M. Letoffe, *Heat-Transfer in a Disc-Type Dsc Apparatus .2. Theoretical Representation.* Thermochimica Acta, 1983. **68**(2-3): p. 305-316.
84. Grabowski, G., et al., *Anisotropy of thermal expansion of 3Y-TZP, α-Al2O3 and composites from 3Y-TZP/α-Al2O3 system.* Arch. Civ. Mech. Eng., 2018. **18**: p. 188-197.
85. Claudy, P., J.C. Commercon, and J.M. Letoffe, *Heat-Transfer in a Disc-Type Dsc Apparatus .1. Experimental.* Thermochimica Acta, 1983. **65**(2-3): p. 245-255.
86. Menczel, J.D., *Temperature calibration of heat flux DSC's on cooling.* Journal of Thermal Analysis, 1997. **49**(1): p. 193-199.
87. Heldman, D.R. and D.B. Lund, *Handbook of food engineering*. 2nd ed. Food science and technology. 2007, Boca Raton: CRC Press/Taylor & Francis. 1023 p.
88. Sari, A., et al., *Synthesis, thermal energy storage properties and thermal reliability of some fatty acid esters with glycerol as novel solid-liquid phase change materials.* Solar Energy Materials and Solar Cells, 2010. **94**(10): p. 1711-1715.
89. Sharma, S.D., H. Kitano, and K. Sagara, *Phase change materials for low temperature solar thermal applications.* Res. Rep. Fac. Eng. Mie Univ, 2004. **29**(1).
90. Dobrovinskaya, E.R., L.A. Lytvynov, and V. Pishchik, *Sapphire: Material, Manufacturing, Applications*. 2009: Springer US.
91. Bogatishcheva, N.S., et al., *Critical properties, heat capacities, and thermal diffusivities of four saturated triglycerides.* Journal of Chemical Thermodynamics, 2017. **113**: p. 308-314.
92. Lee, S., et al., *Thermophysical Properties of Aluminum 1060 Fabricated by Equal Channel Angular Pressing.* International Journal of Thermophysics, 2012. **33**(3): p. 540-551.
93. Lin, L., *Structure in Liquid Triglycerides*. 2014, Dalhousie University: Nova Scotia, Halifax.

94. Chumpitaz, L.D.A., L.F. Coutinho, and A.J.A. Meirelles, *Surface tension of fatty acids and triglycerides.* Journal of the American Oil Chemists Society, 1999. **76**(3): p. 379-382.
95. Jariyavidyanont, K., et al., *Experimental analysis of lateral thermal inhomogeneity of a specific chip-calorimeter sensor.* Thermochimica Acta, 2019. **674**: p. 95-99.
96. Sato, K., et al., *External factors affecting polymorphic crystallization of lipids.* European Journal of Lipid Science and Technology, 2013. **115**(11): p. 1224-1238.
97. Marangoni, A.G., D. Tang, and A.P. Singh, *Non-isothermal nucleation of triacylglycerol melts.* Chemical Physics Letters, 2006. **419**(1): p. 259-264.
98. Becker, R. and W. Döring, *Kinetische Behandlung der Keimbildung in übersättigten Dämpfen.* Annalen der Physik, 1935. **416**(8): p. 719-752.
99. Kashchiev, D., *Solution of the non-steady state problem in nucleation kinetics.* Surface Science, 1969. **14**(1): p. 209-220.
100. Fisher, J.C., J.H. Hollomon, and D. Turnbull, *Kinetics of the Austenite-]Martensite Transformation.* Transactions of the American Institute of Mining and Metallurgical Engineers, 1949. **185**(10): p. 691-700.
101. Pouget, E.M., et al., *The initial stages of template-controlled CaCO3 formation revealed by cryo-TEM.* Science, 2009. **323**(5920): p. 1455-8.
102. Richard, D. and T. Speck, *Crystallization of hard spheres revisited. II. Thermodynamic modeling, nucleation work, and the surface of tension.* The Journal of Chemical Physics, 2018. **148**(22): p. 224102.
103. Marangoni, A.G., et al., *A probabilistic approach to model the nonisothermal nucleation of triacylglycerol melts.* Crystal Growth and Design, 2006. **6**(5): p. 1199-1205.
104. Cerdeira, M., et al., *Nucleation behavior of blended high-melting fractions of milk fat as affected by emulsifiers.* European Journal of Lipid Science and Technology, 2005. **107**(12): p. 877-885.
105. Herrera, M., M. de Leon Gatti, and R. Hartel, *A kinetic analysis of crystallization of a milk fat model system.* Food Research International, 1999. **32**(4): p. 289-298.

106. Marangoni, A.G. and S.E. McGauley, *Relationship between crystallization behavior and structure in cocoa butter.* Crystal Growth & Design, 2003. **3**(1): p. 95-108.
107. Takeuchi, M., S. Ueno, and K. Sato, *Crystallization kinetics of polymorphic forms of a molecular compound constructed by SOS (1,3-distearoyl-2-oleoyl-sn-glycerol) and SSO (1,2-distearoyl-3-oleoyl-rac-glycerol).* Food Research International, 2002. **35**(10): p. 919-926.
108. Zulkurnain, M., F. Maleky, and V.M. Balasubramaniam, *High Pressure Processing Effects on Lipids Thermophysical Properties and Crystallization Kinetics.* Food Engineering Reviews, 2016. **8**(4): p. 393-413.
109. Rodríguez-hornedo, N. and D. Murphy, *Significance of controlling crystallization mechanisms and kinetics in pharmaceutical systems.* Journal of Pharmaceutical Sciences, 1999. **88**(7): p. 651-660.
110. Fisher, J.C., J.H. Hollomon, and D. Turnbull, *Rate of Nucleation of Solid Particles in a Subcooled Liquid.* Science, 1949. **109**(2825): p. 168-169.
111. Hoffman, J.D. and J.J. Weeks, *Melting process and the equilibrium melting temperature of polychlorotrifluoroethylene.* J. Res. Natl. Bur. Stand., Sect. A, 1962. **66**(1): p. 13-28.
112. Golodnizky, D. and M. Davidovich-Pinhas, *New insights into the thermodynamics and kinetics of triacylglycerols crystallization.* Innovative Food Science & Emerging Technologies, 2022. **81**: p. 103115.
113. Takeuchi, M., S. Ueno, and K. Sato, *Synchrotron Radiation SAXS/WAXS Study of Polymorph-Dependent Phase Behavior of Binary Mixtures of Saturated Monoacid Triacylglycerols.* Crystal Growth & Design, 2003. **3**.
114. Lutton, E.S. and A.J. Fehl, *The polymorphism of odd and even saturated single acid triglycerides, C8–C22.* Lipids, 1970. **5**(1): p. 90-99.
115. Cullity, B. and S. Stock, *Elements of x-ray diffraction, Prentice Hall.* Upper Saddle River, NJ, 2001: p. 388.

116. Hagemann, J.W. and J.A. Rothfus, *Polymorphism and transformation energetics of saturated monoacid triglycerides from differential scanning calorimetry and theoretical modeling.* Journal of the American Oil Chemists' Society, 1983. **60**(6): p. 1123-1131.
117. van Langevelde, A., et al., *Structure of mono-acid even-numbered β-triacylglycerols.* Acta Crystallographica Section B, 1999. **55**(1): p. 114-122.
118. Gibbs, J.W., *A Method of Geometrical Representation of the Thermodynamic Properties of Substances by Means of Surfaces.* Transactions of the Connecticut Academy of Arts and Sciences 2, 1873: p. 382-404.
119. Fokin, V.M. and E.D. Zanotto, *Crystal nucleation in silicate glasses: the temperature and size dependence of crystal/liquid surface energy.* Journal of Non-Crystalline Solids, 2000. **265**(1): p. 105-112.
120. Chumpitaz, L., L. Coutinho, and A. Meirelles, *Surface tension of fatty acids and triglycerides.* Journal of Oil & Fat Industries, 1999. **76**: p. 379-382.
121. Prestipino, S., A. Laio, and E. Tosatti, *A fingerprint of surface-tension anisotropy in the free-energy cost of nucleation.* The Journal of Chemical Physics, 2013. **138**(6): p. 064508.
122. Al-Qatami, O. and G. Mazzanti, *The effect of the sample pan position on the determination of the specific heat capacity for lipid materials using heat flux DSC.* Thermochimica Acta, 2022. **710**: p. 179148.
123. Cerdeira, M., R.J. Candal, and M.L. Herrera, *Analytical Techniques for Nucleation Studies in Lipids: Advantages and Disadvantages.* Journal of Food Science, 2004. **69**(9): p. R185-R191.
124. Takeguchi, S., et al. *Multiple β Forms of Saturated Monoacid Triacylglycerol Crystals*. Molecules, 2020. **25**, DOI: 10.3390/molecules25215086.
125. Jadhav, H.B. and U.S. Annapure, *Triglycerides of medium-chain fatty acids: A concise review.* Journal of Food Science and Technology, 2022: p. 1-10.
126. Litwinenko, J.W., et al., *Relationship between crystallization behavior, microstructure, and mechanical properties in a palm oil-based shortening.* Journal of the American Oil Chemists Society, 2002. **79**(7): p. 647-654.

127. Porter, C.J., N.L. Trevaskis, and W.N. Charman, *Lipids and lipid-based formulations: optimizing the oral delivery of lipophilic drugs.* Nature reviews Drug discovery, 2007. **6**(3): p. 231-248.
128. Rane, S.S. and B.D. Anderson, *What determines drug solubility in lipid vehicles: is it predictable?* Advanced drug delivery reviews, 2008. **60**(6): p. 638-656.
129. Ahmad, A. and H. Ahsan, *Lipid-based formulations in cosmeceuticals and biopharmaceuticals.* Biomedical Dermatology, 2020. **4**(1): p. 1-10.
130. Wille, R.L. and E.S. Lutton, *Polymorphism of cocoa butter.* Journal of the American Oil Chemists' Society, 1966. **43**(8): p. 491-496.
131. Timms, R.E., *Phase behaviour of fats and their mixtures.* Progress in Lipid Research, 1984. **23**(1): p. 1-38.
132. Al-Qatami, O., Zhang, Xinyue., Mazzanti, Gianfranco., *Prediction of the onset nucleation temperatures of metastable polymorphs – part 1 – β' polymorph of tridodecanoyl-glycerol (trilaurin).* Journal of the American Chemical Society, 2023.
133. Desgranges, C. and J. Delhommelle, *Molecular Mechanism for the Cross-Nucleation between Polymorphs.* Journal of the American Chemical Society, 2006. **128**(32): p. 10368-10369.
134. Sato, K. and N. Garti, *Crystallization and polymorphic transformation: an introduction.* Surfactant Sci. Ser., 1988. **31**(Cryst. Polymorphism Fats Fatty Acids): p. 3-7.
135. Bayés-García, L., et al., *Lipid crystallization kinetics—roles of external factors influencing functionality of end products.* Current Opinion in Food Science, 2015. **4**: p. 32-38.
136. Ickes, L., et al., *Classical nucleation theory of homogeneous freezing of water: thermodynamic and kinetic parameters.* Physical Chemistry Chemical Physics, 2015. **17**(8): p. 5514-5537.
137. Yu, L., *Nucleation of one polymorph by another.* Journal of the American Chemical Society, 2003. **125**(21): p. 6380-6381.

138. Cavallo, D., et al., *Cross-Nucleation between Concomitantly Crystallizing α- and γ-Phases in Polypivalolactone: Secondary Nucleation of One Polymorph on Another.* Crystal Growth & Design, 2017. **17**(5): p. 2639-2645.
139. Lacmann, R., A. Herden, and C. Mayer, *Kinetics of Nucleation and Crystal Growth.* Chemical Engineering & Technology, 1999. **22**(4): p. 279-289.
140. Al-Qatami, O., Zhang, Xinyue., Mazzanti, Gianfranco., *Prediction of the onset nucleation temperatures of metastable polymorphs – part 1 – β' polymorph of tridodecanoyl-glycerol (trilaurin)*, in *Journal of the American Chemical Society*. 2023.
141. Zhang, X., Al-Qatami, Omar, Mazzanti, Gianfranco, *Crystallization onset and polymorphic occurrence in pure saturated triacylglycerols during cooling from the melt*, in *Crystal Growth and Design*. 2023.
142. Takeguchi, S., et al., *Multiple β Forms of Saturated Monoacid Triacylglycerol Crystals.* Molecules, 2020. **25**(21).

APPENDICES

APPENDIX A: MATLAB CODE USED TO CALCULATE THE GIBBS FREE ENERGY.

```
function [d_H,d_S,d_G] = Delta_Gibbs(T_on,Tagn,Polymorph)
%% Delta_G as f(T_onset) for a given TAG and Polymorph
% Xinyue Zhang, 2021-2022 -- Revised v5.0 --
% G. Mazzanti, O. Qatami
% Arguments
% 1. T_on   onset temperature, °C
% 2. Tagn - number of alkyl carbons
%       12 L
%       14 M
%       16 P
%       18 S
% 3. Polymorph
%       1 alpha
%       2 betaprime
%       3 beta
% T_on = T_on + 273.15;
%% C: Tm, Delta_Hm, and Cp coefficients

% Molecular weights
% Mw kg/mol
L_Mw = 0.639;
M_Mw = 0.723;
P_Mw = 0.807;
S_Mw = 0.891;

% C.1. Specific Heat Coefficients
%          cp_1      cp_0
% a        0.010064          -0.987100
% b'       0.010311          -1.317910
% b        0.008520          -0.940464

% C.1.1. Solid from Hampson & Rothbart 1983
% kJ/(kg.K)
% C.1.1.1. Alpha
% L_a_2=0.0;L_a_1=0.010064; L_a_0=-0.987100;
L_a_2=4.86E-05;L_a_1=-1.62E-02; L_a_0=2.55E+00;
M_a_2=8.05E-05;M_a_1=-3.24E-02; M_a_0=4.70E+00;
P_a_2=5.56E-05;P_a_1=-1.91E-02; P_a_0=2.86E+00;
S_a_2=4.54E-05;S_a_1=-1.33E-02; S_a_0=1.94E+00;
% C.1.1.2. Beta prime
%L_bp_2=0.0;L_bp_1=0.010311; L_bp_0=-1.317910;
L_bp_2=5.68E-05;L_bp_1=-2.26E-02; L_bp_0=3.46E+00;
M_bp_2=5.68E-05;M_bp_1=-2.16E-02; M_bp_0=3.37E+00;
```

```
P_bp_2=8.52E-05;P_bp_1=-3.61E-02; P_bp_0=5.11E+00;
S_bp_2=3.74E-05;S_bp_1=-1.12E-02; S_bp_0=1.81E+00;
% C.1.1.3. Beta
%L_b_2=0.0;L_b_1=0.008520; L_b_0=-0.940464;
L_b_2=4.30E-05;L_b_1=-1.68E-02; L_b_0=2.79E+00;
M_b_2=3.81E-05;M_b_1=-1.46E-02; M_b_0=2.62E+00;
P_b_2=4.45E-05;P_b_1=-1.70E-02; P_b_0=2.76E+00;
S_b_2=1.59E-05;S_b_1=-2.43E-03; S_b_0=8.15E-01;

% C.1.2. Liquid from Morad
% kJ/(kg.K)
L_1=0.002443;L_0= 1.23169; %1.22179455;
M_1=0.002390;M_0=1.3036715;
P_1=0.002474;P_0=1.3035269;
S_1=0.002530;S_0=1.3297305;

% C.2. Melting Point absolute temperature (K)

% Plot, report in °C

L_MP_a=288.75; L_MP_bp=308.25;          L_MP_b=318.85;
M_MP_a=305.75; M_MP_bp=319.05;          M_MP_b=330.25;
P_MP_a=317.85; P_MP_bp=328.85;          P_MP_b=339.05;
S_MP_a=327.85; S_MP_bp=337.45;          S_MP_b=345.65;

% C.3. Enthalpy of melting
% kJ/kg
L_H_a=109.23; L_H_bp=134.58; L_H_b=191.23;
M_H_a=113.25; M_H_bp=146.58; M_H_b=203.00;
P_H_a=118.65; P_H_bp=156.67; P_H_b=212.15;
S_H_a=121.71; S_H_bp=175.55; S_H_b=217.84;

%% Example script to generate curve
% T_ons = 25:75;
% npts = size(T_ons,2);
% for i=1:npts+1;T_on = T_ons(i);dG(i)=Delta_Gibbs(T_on,12,1);end;
% figure;plot(T_ons,dG);
% hold on;plot(L_MP_a-273.15,0,'ro');hold off;
% title('LLL Alpha');
% xlabel('T (°C)');
% ylabel('\Delta G at T_o (kJ/kg)');

%% 4. Calculate (Use switch structure for material & Polymorph)
   switch Tagn
      case 12 % LLL
         % disp('4.1. LLL');
         switch Polymorph
            case 1
               % 4.1.1 Alpha
               % 4.1.1.1. delta H_a
               % This are integrals, thus the terms are difference of squares, not sqares
               % of differences, etc.
               % Enthalpy of liquid
```

```
            H_L_lq_a=L_1/2*(T_on^2-L_MP_a^2)+L_0*(T_on-L_MP_a);
            % Enthalpy of solid
            H_L_a=(L_a_2/3*(T_on^3-L_MP_a^3)+L_a_1/2*(T_on^2-L_MP_a^2)+L_a_0*(T_on-L_MP_a))-
L_H_a;
            d_H=H_L_a-H_L_lq_a; % Difference Solid - Liquid

            % 4.1.1.2. delta S_a
            % Natural logarithm in matlab is written log(x). It comes from the integral
            % of 1/T
            % Entropy of liquid . Note that (log(T1)-log(T2)) = log(T1/T2)
            S_L_lq_a=L_1*(T_on-L_MP_a)+L_0*log(T_on/L_MP_a);
            % Entropy of solid
            S_L_a=L_a_2/2*(T_on^2-L_MP_a^2)+L_a_1*(T_on-L_MP_a)+L_a_0*log(T_on/L_MP_a)-
L_H_a/L_MP_a;
            d_S=S_L_a-S_L_lq_a;% Difference Solid - Liquid

            %4.1.1.3. delta Gibbs_a
            d_G=d_H-T_on*d_S; % Difference Solid - Liquid
        case 2
            % 4.1.2 Betaprime
            % 4.1.2.1. delta H_bp
            % This are integrals, thus the terms are difference of squares, not sqares
            % of differences, etc.
            % Enthalpy of liquid
            H_L_lq_bp=L_1/2*(T_on^2-L_MP_bp^2)+L_0*(T_on-L_MP_bp);
            % Enthalpy of solid
            H_L_bp=(L_bp_2/3*(T_on^3-L_MP_bp^3)+L_bp_1/2*(T_on^2-L_MP_bp^2)+L_bp_0*(T_on-
L_MP_bp))-L_H_bp;
            d_H=H_L_bp-H_L_lq_bp; % Difference Solid - Liquid

            % 4.1.2.2. delta S_bp
            % Natural logarithm in matlab is written log(x). It comes from the integral
            % of 1/T
            % Entropy of liquid . Note that (log(T1)-log(T2)) = log(T1/T2)
            S_L_lq_bp=L_1*(T_on-L_MP_bp)+L_0*log(T_on/L_MP_bp);
            % Entropy of solid
            S_L_bp=L_bp_2/2*(T_on^2-L_MP_bp^2)+L_bp_1*(T_on-
L_MP_bp)+L_bp_0*log(T_on/L_MP_bp)-L_H_bp/L_MP_bp;
            d_S=S_L_bp-S_L_lq_bp;% Difference Solid - Liquid

            %4.1.2.3. delta Gibbs_bp
            d_G=d_H-T_on*d_S; % Difference Solid - Liquid
        case 3
            % 4.1.3 Beta
            % 4.1.3.1. delta H_b
            % This are integrals, thus the terms are difference of squares, not sqares
            % of differences, etc.
            % Enthalpy of liquid
            H_L_lq_b=L_1/2*(T_on^2-L_MP_b^2)+L_0*(T_on-L_MP_b);
            % Enthalpy of solid
            H_L_b=(L_b_2/3*(T_on^3-L_MP_b^3)+L_b_1/2*(T_on^2-L_MP_b^2)+L_b_0*(T_on-L_MP_b))-
L_H_b;
            d_H=H_L_b-H_L_lq_b; % Difference Solid - Liquid
```

```
            % 4.1.3.2. delta S_b
            % Natural logarithm in matlab is written log(x). It comes from the integral
            % of 1/T
            % Entropy of liquid . Note that (log(T1)-log(T2)) = log(T1/T2)
            S_L_lq_b=L_1*(T_on-L_MP_b)+L_0*log(T_on/L_MP_b);
            % Entropy of solid
            S_L_b=L_b_2/2*(T_on^2-L_MP_b^2)+L_b_1*(T_on-L_MP_b)+L_b_0*log(T_on/L_MP_b)-
L_H_b/L_MP_b;
            d_S=S_L_b-S_L_lq_b;% Difference Solid - Liquid

            %4.1.3.3. delta Gibbs_b
            d_G=d_H-T_on*d_S; % Difference Solid - Liquid
        otherwise
            warning('Bad Polymorph number');

    end % of Polymorph selection

  case 14
    disp('4.2. MMM');
  case 16
  % 4.3. PPP
    switch Polymorph
      case 1
        % 4.3.1 Alpha
        % 4.3.1.1. delta H_a
        % This are integrals, thus the terms are difference of squares, not sqares
        % of differences, etc.
        % Enthalpy of liquid
        H_P_lq_a=P_1/2*(T_on^2-P_MP_a^2)+P_0*(T_on-P_MP_a);
        % Enthalpy of solid
        H_P_a=(P_a_2/3*(T_on^3-P_MP_a^3)+P_a_1/2*(T_on^2-P_MP_a^2)+P_a_0*(T_on-P_MP_a))-
P_H_a;
        d_H=H_P_a-H_P_lq_a; % Difference Solid - Liquid

        % 4.3.1.2. delta S_a
        % Natural logarithm in matlab is written log(x). It comes from the integral
        % of 1/T
        % Entropy of liquid . Note that (log(T1)-log(T2)) = log(T1/T2)
        S_P_lq_a=P_1*(T_on-P_MP_a)+P_0*log(T_on/P_MP_a);
        % Entropy of solid
        S_P_a=P_a_2/2*(T_on^2-P_MP_a^2)+P_a_1*(T_on-P_MP_a)+P_a_0*log(T_on/P_MP_a)-
P_H_a/P_MP_a;
        d_S_a=S_P_a-S_P_lq_a;% Difference Solid - Liquid

        %4.3.1.3. delta Gibbs_a
        d_G=d_H-T_on*d_S_a; % Difference Solid - Liquid
      case 2
        d_G=0;
      case 3
        d_G=0;
      otherwise
        warning('Bad Polymorph number');
```

```
            end % of Polymorph selection
        case 18
            disp('4.4. SSS');
        otherwise
            warning('Bad TAG C number');


    end % of TAG selection

end % of Delta_Gibbs
```

APPENDIX B: MATLAB CODE USED TO CALCULATE THE DIFFERENTIAL EQUATIONS OF TURNBULL AND FISHER

```
function [ts,tope,intrf_coef,fval,exitflag,output,
pa_t_sets,L,G,H]=nucl_mod_drive_nonisof_A(sigm,ns,xt,Tmtest,at)

% function to find the parameters dm and d23 for the interfacial energy
% (c) G. Mazzanti, O. Qatami, X. Zhang
% version 12.1
% 2022 - 2023

%% Inputs
%   Tmtest  Melting Temperature for Alpha
%   sigm    number of standard deviations above or below mean To_a value
%   ns      Set number, between 1 and 9
%   xt      Fraction of surface molecules touching liquid
%% Outputs
%   1 ts,       Estimated time to reach i_cr
%   2 tope,     Time of execution of the fit
%   3 intrf_coef,      Coefficients for interfacial energy
%   4 fval,     Minimized value of the objective function
%   4 exitflag, Flag for the type of exit from fmincon
%   5 output,   Message from fmincon
%   7 pa_t_sets, Time - temperature cr data
%   5 L         lambda, Linear and Nonlinear constraints values
%   6 G         grad,     gradient of fval wrt to parameters at the min
%   7 H         Hessian,  Real part of the hessian matrix 8x8 --
%   Uncertainties +/-
%% 1. Setup
tic;  % stars the stopwatch
% Enthaply estimate from the test temperature
TH=TH_f(Tmtest,sigm);
% set options for fmincon
options2=optimoptions('fmincon','Algorithm','sqp');
pa_t_sets=zeros(9,4);
% Alpha average onsets
ToaC=[10.34 10.59 10.73 11.34 11.83 12.37 13.22 15.63 18.59];
% To K
Toa=ToaC+273.15;
% STD dev of the Alpha average onsets
STDYDEV=[0.13 0.14 0.20 0.53 0.78 1.24 1.05 0.86 1.13];
% Cooling rates
CRms(1)=25.0;
CRms(2:9)=20.0:-2.5:2.5;

% values of CRm, To to the results array
pa_t_sets(1:9,1)=CRms;
pa_t_sets(1:9,2)=Toa; %+sigm*STDYDEV;



%% 2. Main Program Sections
```

```
%% 3. Startup section
%  =========================================================
% Step sizes
t_steps=76; % Time steps in the function
i_steps=46; % Steps for the # of molecules i, from 2 to i_cr
n_sets=size(pa_t_sets,1); % The number of sets that you are going to run
%       nim=0; % adds one when you make an image
%  =========================================================
% Prepare emptymatrices
intrfe=zeros(3,2); % Interfacial Energy
% Arrays to store full results
%       To_niso=zeros(1,n_sets); % store the  onset temperatures
%       solec = zeros(t_steps,i_steps,n_sets); % To store the solution of each set
%       i_crc =  zeros(1,n_sets); % to store the values of the critical number of each set
%       xmeshc =  zeros(i_steps,n_sets); % Span of # molecules for each set
%       tspanc= zeros(t_steps,n_sets); % Real time span for each set
%       surfe2=zeros(1,n_sets); % final value of surface energy for each set
      ts=ones(1,n_sets)*t_steps; % final indexes of integration

% ============================================================
% PARAMETERS

%       NA = 6.02214076E23;     % Avogadro number, molecules/mol
%       Mw_L = 0.639;           % Trilaurin, kg/mol
% parameters for LLL --*-- Tm updated
Tm_a=TH(1); Tm_bp=308.3; Tm_b=318.9;
Tm=[Tm_a;Tm_bp;Tm_b];
pa_t_sets(:,3)=(Tm(1)-Toa)./(CRms/60);
%       %The molar volume of the molecules in an embryo(nm3/molecule)
      Vs_a=1.051; Vs_bp=1.030; Vs_b=1.015;
      Vs=[Vs_a;Vs_bp;Vs_b];
%       % Lamellar thickness
      d0_a=3.52; d0_bp=3.25; d0_b=3.12; % nm
      d0=[d0_a;d0_bp;d0_b];
%       % Aspect ratio ra = E1/E2 and d0 spacing
      ra_a=1.8; ra_bp=2.1; ra_b=2.4; % r1/r2
      ra=[ra_a;ra_bp;ra_b];
% Default parameter values

plym=1;
      k0(plym,1)=Vs(plym)/(d0(plym)*ra(plym));
%         kse=(d0(plym)*(1+ra(plym)))^2*k0(plym,1);

      kGs_a=4.17E-25;
%         dT_min_a=d0(plym)/(2*Vs(plym))*kGs_a;
%       kGs_bp=4.593 E-25;
%       surfe_slope_cr=d0(plym)/(2*Vs(plym))*kGs;

% surface energy (delta), kJ/nm^2 (*10^-24)
surf_a=8E-24; surf_bp=17E-24; surf_b=24E-24;
intrfe=[surf_a surf_a;surf_bp surf_bp;surf_b surf_b];
%-------------------------------------------------------------------------
```

```
%% Variables for the fit

u0i=-400;
t_steps=76;
cf=1E-12;
DTmax = 30;
% =-=-=-=-=-=-=-=-=-=-=-=-=-=-=-=-=-=-
warning('off','MATLAB:pdepe:TimeIntegrationFailed');
isot=0; % nonisothermal code
%-------------------
% Set up fittype and options.
ft = fittype( 'power2' );
opts = fitoptions( 'Method', 'NonlinearLeastSquares' );
opts.Display = 'Off';
opts.StartPoint = [-8 -0.7 73];
%-------------------

%% ---------------------------------------------------------------------
% ***** Search for the values of d_m and d_23 *****
%----------------------------------------------------------------------

sedi=[0.1 40.0 xt]; % initial guess for d_m and d_23
sedub =[2.0 sedi(2)*1.2  1.0]; % upper bounds d_m and d_23
sedlb =[0.01 sedi(2)*0.8 xt*0.8]; % lower bounds d_m and d_23
A=[1 -1 0]; % linear constrain, so that d_m < d_23
b=0;        % A1*x1 + A2*x2 <= b : 1*d_m (-1)*d_23 <= 0
nuso=1;
nuse=ns;
%ffx=1.02;
%[x,fval,exitflag,output,lambda,grad,hessian]
[intrf_coef,fval,exitflag,output,L,G,H] = fmincon(@ergen,sedi,A,b,[],[],sedlb,sedub);
checkpoint=0;
%% .-.-.-.-.-.-.-.-.-.   Nested Functions   .-.-.-.-.-.-.-.-.-.
% ---------------------------------------------------------------------

   function [er]=ergen(x)
      %% Execute the model with the parameters chosen
      %-----------------------------------------------------
      %  UPDATE THE VALUES OF THE PARAMETERS IN THIS SECTION
      %-----------------------------------------------------
      errtsq=0;
      excelport=zeros(9,5);
      for nf=nuso:nuse
         % ====================
         % Main parameters
         CRm=pa_t_sets(nf,1);%10.00;
         To=pa_t_sets(nf,2);%291.15;
         % surface energy at melting temperature
         dm = x(1)*1E-24;%8.0E-24;
         d23= x(2)*1E-24;% 17.0E-24; % surface energy at DT = 23, d23 [17 35]
         xtf=x(3); %fratcion of molecules at the surface that are in contact with liquid
         % =-=-=-=-=-=-=-=-=-=-=-=-=-=-=-=-=-=-
```

```
intrfe(plym,1)=dm; % dm [0.01 20]
% =================
%           DT=Tm(plym)-To;
% surface energy at DTmax = 30 to pass to the model
intrfe(plym,2)=intrfe(plym,1)+(d23-intrfe(plym,1))/23*DTmax;


%           % Compute istar for debugging
%           [~,~,d_G] = Delta_Gibbs(To,12,plym);
%           DGs=-d_G/NA*Mw_L;
%           surfeT = surfe(2,1)+se_sl*DT;
%           istar=kse*(surfeT/DGs)^2;
%

 % Non-isothermal time for function
tr=(Tm(plym)-To)/(CRm/60);% real time ramp
% Estimate time that can be solved before max u
tnisof_c=at*tr;
isot=0;

% runs the function

[i_cr,sol]=nucleation_model_A(CRm,plym,To,isot,cf,intrfe,t_steps,i_steps,at,xtf,TH);
t_sol=size(sol,1);

%-----------------------------------------------------

%% Ranges and optional Surface Plot
xmesh=logspace(log10(2),log10(i_cr),i_steps)/i_cr;

% isot == 0 => it is **** non-isothermal ****

tspan= linspace(0.0,tnisof_c,t_steps); % function's time span
%       figure;gca=surf(xmesh,tspan(1:t_sol),exp(sol/u0i-1),'EdgeColor','none');hold on;
%       figure;gca=surf(xmesh,tspan(1:t_sol),exp(sol/u0i-1),'EdgeColor','none');
%       title(sprintf('%1.1f C/min, d_m %2.3f, cf %3G , d_T %4.3f, t %5.2f ,To %6.2f',...
%       CRm,surfe(2,1)*1E24,cf,surfe(2,2)*1E24,tr,To));
%       xlabel('i/i* (# molecules/embryo)');
%       ylabel('t (s)');
%       zlabel('{\ite^{(ln(n_i)/ln(n_0)-1)');
%       title(sprintf('%1.1f C/min, d_m %2.2f, d23 %3.2f, Tm %4.1f, at %8.2f, tr %5.1f, t %6.2f ,To
%7.2f',...
%           CRm,surfe(2,1)*1E24,surfe(2,2)*1E24,Tmtest,tr,To,at(2)));
%       hold off;

%       zlabel('{\itln(ln(n_i))}');


%% Edge finder & Fit power curve
% -----------
gua=exp(sol(1:t_sol,:)/u0i-1); % Transform u values
```

```
        i_num=sum(isinf(gua),2)+1; % Count inf values in each row
        % reset the arrays for the edge & fill them
        pollox=zeros(t_sol,1);
        polloy=zeros(t_sol,1);
        pollox(1:t_sol,1)=xmesh(i_num);
        polloy(1:t_sol,1)=tspan(1,1:t_sol);

        % Fit power law model to data and extrapolate to find the final time
        [fitresult, ~]=fit(pollox, polloy, ft,opts);
        % Extrapolate to (i/i*) = 1
        trcal=(fitresult.a + fitresult.c);

        % Add the square of the error to the sum for automatic operation
        errtsq = errtsq +((trcal-tr)/tr*100)^2*(1+0.0001*(x(3)^2)); % relative error

        %moigo is a z value from the variable u, which is Ln(n_i),
        %which is how many clusters there are in a family (i, i+1, ...)
       %Plot for testing Tm and at
%           gca=figure;
%           axes1 = axes('Parent',gca);
%           hold(axes1,'on');
%           moigo=log10(-sol);
%           surf(xmesh,tspan(1:t_sol),moigo,'EdgeColor','none');
%           view(axes1,[-10 60]);
%           hold on;
%           zv= moigo(1,:)*1.05;
%           plot3(xmesh(1,1:46)*1.05,fitresult.a*(xmesh).^fitresult.b+fitresult.c,zv,'-r','LineWidth',2);
%           set(axes1,'XMinorTick','on','XScale','log','YMinorTick','on','YScale','log',...
%                 'ZMinorTick','on','ZScale','log');
%           xlabel('i/i* (# molecules/embryo)');
%           ylabel('t (s)');
%           zlabel('{\itlog(-ln(n_i))}');
%           title(sprintf('%1.1f C/min d_m %2.2f d_{23} %3.2f Tm %4.1f tr %5.1f t %6.2f To %7.2f at %8.2f',...
%                 CRm,dm*1E24,d23*1E24,Tmtest,tr,trcal,To,at));
%
%              hold off;
%           % plot - optional - direct operation
%           %   figure;semilogx(xmesh(i_num),tspan(1:t_sol),'xb','LineWidth',3);
%           %   xlim([xmesh(1) 1]);
%           %   hold on;semilogx(xmesh,fitresult.a*(xmesh).^fitresult.b+fitresult.c);
%           %   ylim([0 ceil(trcal*11/100)*10]);
%           %   hold off;
        %.....
        %% Store the values for set nf once the fit is ok - direct operation
        % if a group of sets is fitted using different i or t steps, the name of
        % the file must be changed, e.g. 'Fit_sets_GM_101_41'
        %           surfe2(1,nf)=surfe(2);
        %           solec(:,:,nf)=sole(:,:);
        %           i_crc(1,nf)=i_cr;
        excelport(nf,1:5)=[t_sol tr trcal i_cr TH(2)];
                  ts(1,nf)=t_sol;
        %           pseudo_t_sets(nf,1)=CRm;
        %           pseudo_t_sets(nf,2)=To;
```

```
                pa_t_sets(nf,4)=trcal;

          %           xmeshc(1:i_steps,nf)=xmesh;
          %           tspanc(1:t_steps,nf)=tspan;

       end
       er=errtsq;
       %% Save the values to a file - for direct operation
       % filnam='Fit_sets_GM';
       % save(filnam,'surfe2','solec','i_crc','xmeshc','tspanc','cfc','csc');
    end
%% Enthaply estimate from the melting temperature being tested (alpha)
function [TH]=TH_f(Tmtest,sigm)
    % Using the data from C14 to C22 we extrapolated the expected
    % Entropy and its derivative wrt Temperature
    % For a given Tmtest melting temperature, we compute
    % the enthalphy of fusion at that temperature
    % The Standard Error provided by sigm is derived from the data of the
    % other saturated TAGs
    % Reference Vaules
    Tma_r=292.0;
    DSa_r=0.2462;
    % Standard error and ds/dT
    SES_r=0.0043;
    dsdT=0.00141;
    % Compute melting entropy and enthalpy and place them in TH
    DS0=DSa_r+dsdT*(Tmtest-Tma_r)+sigm*SES_r;
    DHa=DS0*Tmtest;
    TH = [Tmtest;DHa];
    Tm(1)=Tmtest;
end


tope=toc; % ends stopwatch
end
```

APPENDIX C: MATLAB CODE USED TO FIND THE INTERFACIAL ENERGY VALUES.

```
function [i_cr_To,sol]=nucleation_model_A(CRm,plym,To,isot,cf,surfe,ts,is,at,xt,TH)
%% Nucleation prediction using Turnbull & Fisher concept
% - to run from nucl_mod_drive with data from preliminary tests
% G. Mazzanti, O. Qatami & X.Zhang  2022-2023
% Version 12.1
%
%% 1. Inputs
% TH        Vector (2,1) with [Tm DH] for Alpha
% CRm       coooling rate, K/min
% plym      Polymorph number
%           1: alpha, 2: betaprime, 3: beta
% To        Onset temperature, K
% isot      Is is isothermal?
%           isot=0 if not isothermal,
%           isot=time if it is isothermal
% cf        Scaling factor for the number of embryos
% surfe     Interfacial energy guesses, dm and d23
% ts        Number of time steps
% is        Number of embryo size steps, i is the number of molecules
% at        Coefficients to estimate the max time that can be calculated
%   xt      Fraction of surface molecules touching liquid

%% 2. Outputs
% i_cr_To   Array with times, i, dm, dm23, etc. values
% sol       2D Array with the values of 'u', log(#embryos_i) wrt time and i

%% 3. Universal constants

kb = 1.380649E-26;      % Botlzmann constant per molecule kJ/K.molecule
hp = 6.62607015E-37;    % Planck consant, kJ.s
NA = 6.02214076E23;     % Avogadro number, molecules/mol
Mw_L = 0.639;           % Trilaurin, kg/mol

%% 4. Property Coefficients
% Melting temperature(K)
% THE MELTING TEMPERATURE OF ALPHA HAS BEEN UPDATED
Tm_a=TH(1); Tm_bp=308.3; Tm_b=318.9;
Tm=[Tm_a;Tm_bp;Tm_b];

% Enthalpy(KJ/mol) 74.3
dHm_a=TH(2); dHm_bp=86; dHm_b=122.2;
dHm=[dHm_a;dHm_bp;dHm_b];

%The molar volume of the molecules in an embryo(nm3/molecule)
Vs_a=1.051; Vs_bp=1.030; Vs_b=1.015;
Vs=[Vs_a;Vs_bp;Vs_b];

% Heat capacity coefficient kJ/(K·mol)kJ/(K^2·mol)kJ/(K^3·mol)
```

```
% Liquid
Cp1_liq = 0.002443;Cp0_liq=1.23169;
% Crystals
Cp0_a=2.55;      Cp0_bp=3.46;      Cp0_b=2.79;
Cp1_a=-1.62E-02; Cp1_bp=-2.26E-02; Cp1_b=-1.68E-02;
Cp2_a=4.86E-05;  Cp2_bp=5.68E-05;  Cp2_b=4.30E-05;
Cp_c=[[Cp0_a;Cp1_a;Cp2_a],[ Cp0_bp;Cp1_bp;Cp2_bp],...
   [Cp0_b;Cp1_b;Cp2_b]];

% Aspect ratio ra = E1/E2 and d0 spacing
ra_a=1.0; ra_bp=1.8; ra_b=2.4; % r1/r2
ra=[ra_a;ra_bp;ra_b];

d0_a=3.52; d0_bp=3.25; d0_b=3.12; % nm
d0=[d0_a;d0_bp;d0_b];

% av_a=d0_a*ra_a; av_bp=d0_bp*ra_bp; av_b=d0_b*ra_b;
% av=[av_a;av_bp;av_b];

% Molecules/nm in Crystal
mo_a=[1/d0_a; 1/d0_bp; 1/d0_b];
m1_a=[1.781; 1.672; 1.556];
m2_a=ones(3,1);
for plmr=1:3
 m2_a(plmr)=1/(Vs(plmr)*mo_a(plmr)*m1_a(plmr)) ;
end
k0=ones(3,1);
k1=ones(3,1);
for plmr=1:3
   k0(plmr,1)=Vs(plmr)/(d0(plmr)*ra(plmr));
   k1(plmr,1)=d0(plmr)*(1+ra(plmr))*(k0(plmr,1))^(1/2);
end
a_s=ones(3,1);
for plmr=1:3
 a_s(plmr,1)=2*(m1_a(plmr)+ra(plmr)*m2_a(plmr))*(k0(plmr,1))^(1/2);
end

% a_s(1,1)=2*(m1_a+av_a/(m1_a*Vs_a))*(Vs_a/av_a)^(1/2);
% a_s(2,1)=2*(m1_bp+av_bp/(m1_bp*Vs_bp))*(Vs_bp/av_bp)^(1/2);
% a_s(3,1)=2*(m1_b+av_b/(m1_b*Vs_b))*(Vs_b/av_b)^(1/2);

% % surface energy (delta), kJ/nm^2 (*10^-24)
% surf_a=8E-24; surf_bp=15E-24; surf_b=24E-24;
% % surfe=[surf_a;surf_bp;surf_b];
%[~,~,d_G] = Delta_Gibbs(To,12,plym,TH);
%DGs=-d_G/NA*Mw_L;
%surfe_lim=delta_slope*DGs;
kGs=4.5932E-25;
porrongo =d0(plym)/(2*Vs(plym))*kGs;
DTmax=30;
DT=Tm(plym)-To;
% if surfe(2,2)< porrongo*DT
%     surfe(2,2)= porrongo*DT;
```

```
% end
surfe_slope = ( surfe(plym,2)- surfe(plym,1))/DTmax;
% kass=d0(plym)*(1+ra(plym))/(m1_a(plym)+ra(plym)*m2_a(plym));

%-------------------------------------------------------------------
%% 5. Optional - Plot of the critical size as a function of temperature
%-------------------------------------------------------------------
% Set the value of plotsizes to 1 for plot, and to 0 for no plot
plotsizes=0;
if plotsizes

   npts_size=101;
   A_T=zeros(npts_size,3);
   B_T=zeros(npts_size,3);
   colr=['-r';'-g';'-b'];
   T_sizes = ones(npts_size,3);
   z_sizes = ones(npts_size,3);
   i_sizes = ones(npts_size,3);
   DFxTT=zeros(npts_size,2);
   DGsT=zeros(npts_size,1);
   surfe_T=zeros(npts_size,1);
   % Part of Dfx that dpends on i
   ni_mf=1:npts_size;
   DFxi=((sqrt(ni_mf)-sqrt(ni_mf+1))*k1(plmr,1)-ra(plmr,1))*k0(plmr,1);
   figure(95);semilogx(ni_mf,-DFxi,'-c','LineWidth',1.5);

   for plmr=plym:plym

      T_sizes(:,plmr)= linspace(Tm(plmr)-20.0,0.999*Tm(plmr),npts_size);
      for np=1:npts_size
         T_mf=T_sizes(np,plmr);
         [~,~,d_G] = Delta_Gibbs(T_mf,12,plmr,TH);
         DGs=-d_G/NA*Mw_L;
         DGsT(np,1)=DGs;
         % # of molecules in the critical size embryo, i_cr
         surfeT=surfe(plmr,1)+surfe_slope*(Tm(plmr)-T_mf);
         surfe_T(np,1)=surfeT;
         i_cr =(d0(plmr)*(1+ra(plmr)))^2*k0(plmr,1)*(surfeT/DGs)^2;

         % Length of the first dimension for the critical size embryo, in nm
         z_cr=(i_cr*k0(plmr,1))^(1/2);
         % Save to vectors
         z_sizes(np,plmr) = z_cr;
         i_sizes(np,plmr) = i_cr;
         A2 = (d0(plmr)+(z_cr+d0(plmr))*ra(plmr))*2*surfeT-DGs/k0(plmr)*z_cr;
         A_T(np,plmr)=z_cr*A2/(kb*T_mf*i_cr^(2.0/3.0));
         B_T(np,plmr)=2.0/3.0*A_T(np,plmr)*i_cr^(-1.0/3.0);
         %-----------------------

         %        % Enthalpy, entropy, and free energy of the embryos and their difference
         DHL = Cp0_liq*(T_mf-Tm(plym)) + Cp1_liq*(T_mf^2-Tm(plym)^2)/2;
         DSL = Cp0_liq*log(T_mf/Tm(plym)) + Cp1_liq*(T_mf-Tm(plym));
         DFL =(DHL-T_mf*DSL)/NA;
```

```
        %       % Crystallization entropy for the aggregation barrier
        DSC = Cp_c(1,plym)*log(T_mf/Tm(plym)) + Cp_c(2,plym)*(T_mf-Tm(plym)) +...
           Cp_c(3,plym)*(T_mf^2-Tm(plym)^2)/2-DSL-dHm(plym)/Tm(plym);

        DFxT=(DFL+DGs)/2-T_mf/NA*DSC;
        DFxTT(np,1)=T_mf;
        DFxTT(np,2)=DFxT;

        % ---===-------------===-----------===
        % Difference of F energy between embryo and that with one more
        % molecule
%               DDFF=(k1(plym,1)*(i_m^0.5-(i_m+1)^0.5)-ra(plym))*k0(plym,1)*2*surfeT+DGs;
%               ai=d0(plym)*(1+ra(plym))+ra(plym)*(k0(plym,1)*i_m)^(1/2);
%               ai1=d0(plym)*(1+ra(plym))+ra(plym)*(k0(plym,1)*(i_m+1))^(1/2);
%               DSCA = log(ai1/ai*((i_m+1)/i_m)^(1/2))*kass*surfeT;
%
%          %        % Overall  energy barrier, in KJ/molecule
%
%               Df_x=((DDFF+DFL)/2-T/NA*DSC+DSCA);
        %-----------------------
      end
      % Plot the critical sizes (in nm)
       figure(90);semilogy(Tm(plmr)-T_sizes(:,plmr),z_sizes(:,plmr),colr(plmr,:),'LineWidth',2);
       xlabel('Tm-To'); ylabel('\xi_c');
       % Plot the Chemnical Potential and the Interfacial Energy
       figure(99);plot(Tm(plmr)-T_sizes(:,plmr),DGsT(:,1),'-r','LineWidth',2);
       hold on;plot(Tm(plmr)-T_sizes(:,plmr),surfe_T(:,1),'--b','LineWidth',1.5);
       plot(Tm(plmr)-T_sizes(:,plmr),d0_a/(2*Vs_a)*DGsT(:,1),'-.k');
       xlabel('Tm-To'); ylabel('\DeltaG_s');
       hold off;
       %        hold on;
    end
    plmr=plym;
%     xlabel('Tm-To'); ylabel('\xi_c');
    hold off;
    % Plot the critical number of molecules as function of undercooling
    figure(91);semilogy(Tm(plmr)-T_sizes(:,plmr),i_sizes(:,plmr),'-b','LineWidth',2);
    xlabel('Tm-To'); ylabel('\it{i^*}');

     % Plot the DF* energy as f(T)
    DFstar=4/27*(A_T(:,plmr).^3)./(B_T(:,plmr).^2);
    figure(92);semilogy(Tm(plmr)-T_sizes(:,plmr),DFstar,'k','LineWidth',2);
    xlabel('Tm-To'); ylabel('{\DeltaF^*}');

    % Plot the F energy parameters A and B
    figure(93);plot(Tm(plmr)-T_sizes(:,plmr),A_T(:,plmr),'r','LineWidth',2);
    hold on; plot(Tm(plmr)-T_sizes(:,plmr),B_T(:,plmr),'--b','LineWidth',2);
    xlabel('Tm-To'); ylabel('A,B');
    hold off;

    % Plot the Temperature (not intefacial energy)part of exponential Delta_f_^x
    figure(94);
```

```
    hold on;plot(Tm(plmr)-T_sizes(:,plmr),DFxTT(:,2),'--r','LineWidth',2);
    xlabel('Tm-To'); ylabel('{\DeltaF^x_T}');
    hold off;


end

% %-------------------------------------------------------------------
 %% 6. Optional - Plot of Gibbs energy F as a function of temperature for alpha
% %-------------------------------------------------------------------
% Set the value of plotdf to 1 for plot, and to 0 for no plot
plotdf=0;
if plotdf
    i_DF_c = ones(3,2);
    colr=["#0000FF";"#9966FF";"#FF0000"];
    i_mf(:,1)=logspace(0,5,201);
    DF_mf=zeros(201,3);
    plmr=plym;
    figure(12);
    for nT_mf = 1:3
        T_mf=282.0+nT_mf*2.0;
        surfeT=surfe(plmr,1)+surfe_slope*(Tm(plmr)-T_mf);
        [~,~,d_G] = Delta_Gibbs(T_mf,12,plmr,TH);
        DGs=-d_G/NA*Mw_L;
        for ni_mf=1:201
            DF_mf(ni_mf,nT_mf)=k1(plmr,1)*2*surfeT*(i_mf(ni_mf,1)^(1/2))-DGs*i_mf(ni_mf,1);
        end
        oky(:,1)=DF_mf(:,nT_mf)>0;
        posdn=sum(oky(:,1))-1;
        DF_mf(:,nT_mf)=oky(:,1).*DF_mf(:,nT_mf)/(kb*T_mf);
        semilogx(i_mf(1:posdn,1),DF_mf(1:posdn,nT_mf),'Color',colr(nT_mf,:),'LineWidth',3);
        hold on;
        % Critical number of molecules and its DF
        i_cr =( d0(plmr)*(1+ra(plmr))*surfeT/DGs)^2*k0(plmr,1);
        DF_cr=(k1(plmr,1)*2*surfeT*(i_cr^(1/2))-DGs*i_cr)/(kb*T_mf);
        semilogx(i_cr,DF_cr,'ok','LineWidth',2);
        zeta_cr = (i_cr*k0(plym,1))^(1/2);
        A2 = (d0(plym)+(zeta_cr+d0(plym))*ra(plym))*2*surfeT-DGs/k0(plym)*zeta_cr;
        A=zeta_cr*A2/(kb*T_mf*i_cr^(2.0/3.0));
        B=2.0/3.0*A*i_cr^(-1.0/3.0);
       % A,B
       i_DF_c(nT_mf,1)=i_cr;
       i_DF_c(nT_mf,2)=DF_cr;
    end
    hold off
end
%====================================
%% 7. Solve the differential equation
%====================================
% 7.1. Parepare the parameters
CR = CRm/60.0; % Cooling rate in K/s
t_steps=ts; % number of time steps
i_steps=is; % number of steps for 'size' = molecules/embryo
```

```
% Cartesian space for the coordinates is specified by m=0
% (instead of cyl or sph coords) i.e.the two coordinates are
%  "i" number of molecules of each class;
%  "u" =ln(n_i) ln of the number of embryos of each class
m=0;
% initial value for ni_o = exp(u0i)
u0i=-400;
% Chemical potential DGs at the onset temperature
[~,~,d_G] = Delta_Gibbs(To,12,plym,TH);
DGs=-d_G/NA*Mw_L;
% Interfacial energy at the onset temperature
surfeTo=surfe(plym,1)+surfe_slope*(Tm(plym)-To);
% Number of molecules of the critical size embryo
i_cr_To =( d0(plym)*(1+ra(plym))*surfeTo/DGs)^2*k0(plym,1);
% Vector with the values of the number of molecules "i"
% in number of molecules, starts at 2
xmesh = logspace(log10(2),log10(i_cr_To),i_steps);

if isot
   % When isot is > 0, i.e. there is an isothermal time
   tr = isot;
   % estimate time stop for calculation
   isotf=at*tr;
   tspan= linspace(0.0,isotf,t_steps); % in seconds

else
   %(When isot == 0 and it is non-isothermal)
   tr=(Tm(plym)-To)/CR;% real time
   tnisof= at*tr;
   tspan= linspace(0.0,tnisof,t_steps); % function's time span

end
% Set the options for the ode solver associated with the mesh
opts = odeset('NormControl','on','RelTol',1e-3,'AbsTol',1e-6);
warning('off','MATLAB:ode15s:IntegrationTolNotMet');

%% 7.2. Call the pdepe function to solve the parabolic partial differential eq.

sol = pdepe(m,@pdefun,@icfun,@bcfun,xmesh,tspan,opts);

Turba=0;
% sole=sol>0;
% sole=sole.*sol;
%figure;surf(xmesh,tspan,-sol);
% sole=log10(-sol);
% figure;surf(xmesh,tspan,sole);

% =========================================================================
%%    *****          NESTED FUNCTIONS              *****
% =========================================================================
%% NF1. Initial conditions function
function u0 = icfun(x)
   % Initial value for u ( ln of number of embryos of each class)
```

```
    u0=u0i*x./x;
end
%% NF2. Boundary conditions function
function [pl,ql,pr,qr] = bcfun(~,ul,~,ur,~)
  % boundaries [pl,ql,pr,qr] = bcfun(xl,ul,xr,ur,t)
  pl = ul;
  ql = 1;
  pr =ur-u0i;
  qr = 1;
end

%% NF3. Function F&T differential equation
%[c,f,s] = pdefun(x,t,u,dudx)
    function [c,f,s] =pdefun(i_m,t,u,dudx)
        % Determine the temperature at the time step t
        if isot
            T=To;
        else
            if t==0
                tri=0;
            else
                tri=t;
            end
            T = Tm(plym)-CR*tri;
        end
        DT = Tm(plym)-T;
        surfeT=surfe(plym,1)+surfe_slope*DT;

        % Numer of surface molecules i_si for embryo of "i" molecules
        i_si=a_s(plym,1)*i_m^(1/2);

        % Chemical potential DGs and critical number of molecules at the
        % temperature being calculated
        if t==0&&isot==0
            DGs=0;
            i_cr=1E30;
        else
            [~,~,d_G] = Delta_Gibbs(T,12,plym,TH);
            DGs=-d_G/NA*Mw_L;
            % # of molecules in the critical size embryo, i_cr
            i_cr =( d0(plym)*(1+ra(plym))*surfeT/DGs)^2*k0(plym,1);
        end
        % Length of the first dimension for the critical size embryo, in nm
        zeta_cr = (i_cr*k0(plym,1))^(1/2);

        % A & B parameters from i_cr, surfeT, etc.
        A2 = (d0(plym)+(zeta_cr+d0(plym))*ra(plym))*2*surfeT-DGs/k0(plym)*zeta_cr;
        A=zeta_cr*A2/(kb*T*i_cr^(2.0/3.0));
        B=2.0/3.0*A*i_cr^(-1.0/3.0);

        % Difference of F energy between an embryo and one with one more
        % molecule
        DDFF=(k1(plym,1)*(i_m^0.5-(i_m+1)^0.5)-ra(plym))*k0(plym,1)*2*surfeT+DGs;
```

```
        % Enthalpy, entropy, and free energy of the embryos and their difference
        DHL = Cp0_liq*(T-Tm(plym)) + Cp1_liq*(T^2-Tm(plym)^2)/2;
        DSL = Cp0_liq*log(T/Tm(plym)) + Cp1_liq*(T-Tm(plym));
        DFL =(DHL-T*DSL)/NA;

        % Crystallization entropy for the aggregation barrier
        DSC = Cp_c(1,plym)*log(T/Tm(plym)) + Cp_c(2,plym)*(T-Tm(plym)) +...
            Cp_c(3,plym)*(T^2-Tm(plym)^2)/2-DSL-dHm(plym)/Tm(plym);

        % Overall  energy barrier, in KJ/molecule

        Df_x=((DDFF+DFL)/2-T/NA*DSC);

        % Parabolic pde terms in n_i
        %         cf scales the time
        c = 1/((xt*i_si*kb*T/hp)*i_m^(2.0/3.0)*exp(-Df_x/(kb*T)));

        % parabolic pde terms in transformation n_i= exp(u)

        f = -u*cf;
        s = -(2.0/3.0*A*i_m^(-1.0/3.0)-B)*cf;



% ------  ------  ------  ------  ------  ------  ------  ------  ------
%       /////  Debugging additional code - if needed   /////
%       Derivative of "u" wrt to time, to check consistency
%         du_dt=(dudx+s)/c;
%         if du_dt<0
%             s=-dudx;
%         end
%         if (i_m>i_cr_To*0.5)&&i_m<33%(t>tnisof/3)&&
% %           kass=d0(plym)*(1+ra(plym))/(m1_a(plym)+ra(plym)*m2_a(plym));
%             xmeshi=logspace(log10(2),log10(1000),51);
%             k3T=(DFL+DGs)/2-T/NA*DSC;
% %             K3TT(floor(t/tnisof*75)+1,1)=T;
% %             K3TT(floor(t/tnisof*75+1),2)=k3T;
%             rin=d0(plym)*(1+ra(plym))+ra(plym)*(k0(plym,1)*(xmeshi+1)).^(1/2);
%             rid=d0(plym)*(1+ra(plym))+ra(plym)*(k0(plym,1)*xmeshi).^(1/2);
%             rii=log((rin./rid).*((xmeshi+1)./xmeshi).^(1/2))*kass;
%             rio=((xmeshi.^(1/2)-(xmeshi+1).^(1/2))*k1(plym,1)-ra(plym))*k0(plym,1);
%             kh=2*(m1_a(plym)+ra(plym))*(k0(plym)^(1/2))*kb*T/hp;
%             c_i=kh*exp(-((rio+rii)*surfeT+k3T)/(kb*T)).*xmeshi.^(7/6);
%             s_i = (2.0/3.0*A*xmeshi.^(-1.0/3.0)-B);
%             du_dt=(dudx+s)/c; % add a breakpoint here
%         end
    end % of NF3


end % of nucleation_model_A
```

APPENDIX D: COPYRIGHT PERMSSION